

Multifunctionalization of Nanostructured Metal Oxides

Guest Editors: Zijie Yan, Yu Wang, Dawen Zeng, Douglas B. Chrisey,
and Min Liu





Multifunctionalization of Nanostructured Metal Oxides

Journal of Nanomaterials

Multifunctionalization of Nanostructured Metal Oxides

Guest Editors: Zijie Yan, Yu Wang, Dawen Zeng,
Douglas B. Chrisey, and Min Liu



Copyright © 2015 Hindawi Publishing Corporation. All rights reserved.

This is a special issue published in "Journal of Nanomaterials." All articles are open access articles distributed under the Creative Commons Attribution License, which permits unrestricted use, distribution, and reproduction in any medium, provided the original work is properly cited.

Editorial Board

Domenico Acierno, Italy
Katerina Aifantis, USA
Sheikh Akbar, USA
Nageh K. Allam, USA
Margarida Amaral, Portugal
Martin Andersson, Sweden
Raul Arenal, Spain
Ilaria Armentano, Italy
Vincenzo Baglio, Italy
Lavinia Balan, France
Thierry Baron, France
Andrew R. Barron, USA
Reza Bayati, USA
Hongbin Bei, USA
Daniel Bellet, France
Stefano Bellucci, Italy
Enrico Bergamaschi, Italy
Samuel Bernard, France
D. Bhattacharyya, New Zealand
Sergio Bietti, Italy
Giovanni Bongiovanni, Italy
Theodorian Borca-Tasciuc, USA
Mohamed Bououdina, Bahrain
Torsten Brezesinski, Germany
C. Jeffrey Brinker, USA
Christian Brosseau, France
Philippe Caroff, Australia
Victor M. Castaño, Mexico
Albano Cavaleiro, Portugal
Bhanu P. S. Chauhan, USA
Shafiul Chowdhury, USA
Jin-Ho Choy, Republic of Korea
Kwang-Leong Choy, UK
Yu-Lun Chueh, Taiwan
Elisabetta Comini, Italy
Giuseppe Compagnini, Italy
David Cornu, France
Miguel A. Correa-Duarte, Spain
Pantaleo D. Cozzoli, Italy
Shadi A. Dayeh, USA
Luca Deseri, USA
Yong Ding, USA
Philippe Dubois, Belgium
Alain Dufresne, France
Zehra Durmus, Turkey
Joydeep Dutta, Oman
Ali Eftekhari, USA
Jeffrey Elam, USA
Samy El-Shall, USA
Ovidiu Ersen, France
Claude Estournès, France
Andrea Falqui, KSA
Matteo Ferroni, Italy
Elena J. Foster, USA
Ilaria Fratoddi, Italy
Alan Fuchs, USA
Miguel A. Garcia, Spain
Siddhartha Ghosh, Singapore
P. K. Giri, India
Russell E. Gorga, USA
Jihua Gou, USA
Jean M. Greneche, France
Smrati Gupta, Germany
Kimberly Hamad-Schifferli, USA
Simo-Pekka Hannula, Finland
Michael Harris, USA
Yasuhiko Hayashi, Japan
F. Hernandez-Ramirez, Spain
Michael Z. Hu, USA
Nay Ming Huang, Malaysia
Shaoming Huang, China
David Hui, USA
Zafar Iqbal, USA
Balachandran Jeyadevan, Japan
Xin Jiang, Germany
Rakesh Joshi, Australia
J.-won Kang, Republic of Korea
Hassan Karimi-Maleh, Iran
Antonios Kelarakis, UK
Alireza Khataee, Iran
Ali Khorsand Zak, Iran
Philippe Knauth, France
Ralph Krupke, Germany
Christian Kübel, Germany
Prashant Kumar, UK
Michele Laus, Italy
Eric Le Bourhis, France
Burtrand Lee, USA
Jun Li, Singapore
Meiyong Liao, Japan
Shijun Liao, China
Silvia Licocchia, Italy
Wei Lin, USA
Nathan C. Lindquist, USA
Jun Liu, USA
Zainovia Lockman, Malaysia
Nico Lovergine, Italy
Jim Low, Australia
Jue Lu, USA
Songwei Lu, USA
Ed Ma, USA
Laura M. Maestro, Spain
Gaurav Mago, USA
Muhamamd A. Malik, UK
Devanesan Mangalaraj, India
Sanjay R. Mathur, Germany
Tony McNally, UK
Yogendra Mishra, Germany
Paulo Cesar Morais, Brazil
Paul Munroe, Australia
Jae-Min Myoung, Republic of Korea
Rajesh R. Naik, USA
Albert Nasibulin, Russia
Toshiaki Natsuki, Japan
Koichi Niihara, Japan
Natalia Noginova, USA
Sherine Obare, USA
Won-Chun Oh, Republic of Korea
Atsuto Okamoto, Japan
Abdelwahab Omri, Canada
Ungyu Paik, Republic of Korea
Piersandro Pallavicini, Italy
Edward A. Payzant, USA
Alessandro Pegoretti, Italy
Ton Peijs, UK
Oscar Perales-Pérez, Puerto Rico
Jorge Pérez-Juste, Spain
Alexey P. Popov, Finland
Philip D. Rack, USA
Peter Reiss, France
Orlando Rojas, USA
Marco Rossi, Italy
Ilker S. Bayer, Italy
Cengiz S. Ozkan, USA
Sudipta Seal, USA



Shu Seki, Japan
Vladimir Šepelák, Germany
Huaiyu Shao, Japan
Prashant Sharma, USA
Donglu Shi, USA
Bhanu P. Singh, India
Surinder Singh, USA
Vladimir Sivakov, Germany
Ashok Sood, USA
Adolfo Speghini, Italy
Marinella Striccoli, Italy
Xuping Sun, KSA
Ashok K. Sundramoorthy, USA
Angelo Taglietti, Italy

Bo Tan, Canada
Leander Tapfer, Italy
Valeri P. Tolstoy, Russia
Muhammet S. Toprak, Sweden
Ramon Torrecillas, Spain
Achim Trampert, Germany
Takuya Tsuzuki, Australia
Tamer Uyar, Turkey
Bala Vaidhyanathan, UK
Luca Valentini, Italy
Rajender S. Varma, USA
Ester Vazquez, Spain
Antonio Villaverde, Spain
Ajayan Vinu, Australia

Ruibing Wang, Macau
Shiren Wang, USA
Yong Wang, USA
Magnus Willander, Sweden
Ping Xiao, UK
Zhi Li Xiao, USA
Yangchuan Xing, USA
Doron Yadlovker, Israel
Yoke K. Yap, USA
Kui Yu, Canada
William Yu, USA
Michele Zappalorto, Italy
Renyun Zhang, Sweden

Contents

Multifunctionalization of Nanostructured Metal Oxides, Zijie Yan, Yu Wang, Dawen Zeng, Douglas B. Chrisey, and Min Liu
Volume 2015, Article ID 102976, 1 page

Facile Preparation of Efficient WO₃ Photocatalysts Based on Surface Modification, Min Liu, Hongmei Li, and Yangsu Zeng
Volume 2015, Article ID 502514, 7 pages

Photocatalysis of Yttrium Doped BaTiO₃ Nanofibres Synthesized by Electrospinning, Zhenjiang Shen, Yu Wang, Wanping Chen, Helen Lai Wah Chan, and Lina Bing
Volume 2015, Article ID 327130, 6 pages

Crystallization Behavior of Phosphate Glasses with Hydrophobic Coating Materials, Jaeyeop Chung and Bongki Ryu
Volume 2015, Article ID 981720, 10 pages

Laser-Doping through Anodic Aluminium Oxide Layers for Silicon Solar Cells, Pei Hsuan Doris Lu, Alison Lennon, and Stuart Wenham
Volume 2015, Article ID 870839, 8 pages

Nanocrystallization of Vanadium Borophosphate Glass for Improving the Electrical and Catalytic Properties, Su-Yeon Choi and Bong-Ki Ryu
Volume 2015, Article ID 201597, 9 pages

Nanoscale Ferroelectric Switchable Polarization and Leakage Current Behavior in (Ba_{0.50}Sr_{0.50})(Ti_{0.80}Sn_{0.20})O₃ Thin Films Prepared Using Chemical Solution Deposition, Venkata Sreenivas Puli, Shiva Adireddy, Dhiren K. Pradhan, Ram S. Katiyar, and Douglas B. Chrisey
Volume 2015, Article ID 340616, 7 pages

Ferromagnetic Property of Co and Ni Doped TiO₂ Nanoparticles, Qing Wang, Xiaoming Liu, Xuegang Wei, Jianfeng Dai, and Weixue Li
Volume 2015, Article ID 371582, 5 pages

Photocatalytically Active YBa₂Cu₃O_{7-x} Nanoparticles Synthesized via a Soft Chemical Route, Zhenjiang Shen, Yongming Hu, Linfeng Fei, Kun Li, Wanping Chen, Haoshuang Gu, and Yu Wang
Volume 2015, Article ID 589426, 5 pages

Editorial

Multifunctionalization of Nanostructured Metal Oxides

Zijie Yan,¹ Yu Wang,² Dawen Zeng,³ Douglas B. Chrisey,⁴ and Min Liu⁵

¹Department of Chemical & Biomolecular Engineering, Clarkson University, Potsdam, NY 13699, USA

²School of Materials Science and Engineering, Nanchang University, Nanchang 330029, China

³Department of Materials Science and Engineering, Huazhong University of Science and Technology, Wuhan 430074, China

⁴Department of Physics and Engineering Physics, Tulane University, New Orleans, LA 70118, USA

⁵Department of Electrical and Computer Engineering, The University of Toronto, Toronto, ON, Canada M5S 3G4

Correspondence should be addressed to Zijie Yan; zyan@clarkson.edu

Received 16 September 2015; Accepted 16 September 2015

Copyright © 2015 Zijie Yan et al. This is an open access article distributed under the Creative Commons Attribution License, which permits unrestricted use, distribution, and reproduction in any medium, provided the original work is properly cited.

Metal oxides are a rich family of materials that have nourished many research areas. From colossal magnetoresistance to multiferroicity and from catalysts to wearable devices, metal oxides never lack new materials with fascinating properties and great potential for device applications. The ability to control materials at the nanometric level has further broadened the landscape of research for metal oxides. With rational control of sizes, structures, compositions, and morphologies, nanostructured metal oxides can possess novel optical, electronic, magnetic, and/or mechanical properties that do not exist in bulk forms. These properties have enabled applications of metal oxides in various areas, including electronics, photonics, sensors, catalysis, photovoltaics, and batteries. A better understanding of the origin of novel metal oxide properties promises further improvements that are waiting to be discovered, yet difficulties still exist for applications that require integrating or balancing multiple aspects of the material properties. The integration of metal oxides in prototype devices needs innovations in synthesis, functionalization, assembly, and characterization of nanostructures, which in turn will inspire new applications of metal oxides.

This special issue features articles that address these challenges. The authors report here their achievements in the design, fabrication, modification, and characterization of multifunctional metal oxide nanostructures. It is worth noting that $\text{YBa}_2\text{Cu}_3\text{O}_{7-x}$ (YBCO) is a well-known material for “high temperature superconductivity.” However, in the paper entitled “Photocatalytically Active $\text{YBa}_2\text{Cu}_3\text{O}_{7-x}$ Nanoparticles Synthesized via a Soft Chemical Route,” Z. Shen et al. explored the chemical properties of YBCO

and found that YBCO nanoparticles could show excellent photocatalytic effects without compromising their normal superconductivity properties. This work provides a good example of obtaining multifunctional metal oxides based on the surface effects of nanostructures.

In another article entitled “Nanoscale Ferroelectric Switchable Polarization and Leakage Current Behavior in $(\text{Ba}_{0.50}\text{Sr}_{0.50})(\text{Ti}_{0.80}\text{Sn}_{0.20})\text{O}_3$ Thin Films Prepared Using Chemical Solution Deposition,” V. S. Puli et al. investigated the ferroelectric/piezoelectric effects of $(\text{Ba}_{0.50}\text{Sr}_{0.50})(\text{Ti}_{0.80}\text{Sn}_{0.20})\text{O}_3$ (BSTS) thin films at the nanoscale level using piezoresponse force microscopy and revealed the nanoscale switchability of ferroelectric polarization in these chemical solution deposited BSTS thin films. This observation opens up the possibility of further optimizing physical and electrical properties of BSTS films for practical applications, including nonvolatile ferroelectric memories, data-storage media, piezoelectric actuators, and electric energy storage capacitors.

The guest editors hope that the special issue will draw attention to the multifunctionalization of nanostructured metal oxides and stimulate not only the discovery of new multifunctional metal oxides, but also the detection of new properties in traditional metal oxides *via* the state-of-the-art nanotechnology.

Zijie Yan
Yu Wang
Dawen Zeng
Douglas B. Chrisey
Min Liu

Research Article

Facile Preparation of Efficient WO₃ Photocatalysts Based on Surface Modification

Min Liu,^{1,2} Hongmei Li,¹ and Yangsu Zeng¹

¹*Institute of Laser and Information, Department of Information Engineering, Shaoyang University, Hunan 42200, China*

²*School of Engineering, The University of Tokyo, 7-3-1 Hongo, Bunkyo-ku, Tokyo 113-8656, Japan*

Correspondence should be addressed to Hongmei Li; hongmeili82@gmail.com and Yangsu Zeng; yangsuz@vip.sina.com

Received 8 February 2015; Revised 4 August 2015; Accepted 17 August 2015

Academic Editor: Sherine Obare

Copyright © 2015 Min Liu et al. This is an open access article distributed under the Creative Commons Attribution License, which permits unrestricted use, distribution, and reproduction in any medium, provided the original work is properly cited.

Tungsten trioxide (WO₃) was surface modified with Cu(II) nanoclusters and titanium dioxide (TiO₂) nanopowders by using a simple impregnation method followed by a physical combining method. The obtained nanocomposites were studied by scanning electron microscope, X-ray photoelectron spectroscopy spectra, UV-visible light spectra, and photoluminescence, respectively. Although the photocatalytic activity of WO₃ was negligible under visible light irradiation, the visible light photocatalytic activity of WO₃ was drastically enhanced by surface modification of Cu(II) nanoclusters and TiO₂ nanopowders. The enhanced photocatalytic activity is due to the efficient charge separation by TiO₂ and Cu(II) nanoclusters functioning as cocatalysts on the surface. Thus, this simple strategy provides a facile route to prepare efficient visible-light-active photocatalysts for practical application.

1. Introduction

As one of the most important transition metal oxides, tungsten trioxide (WO₃) has attracted considerable attention due to its promising physical and chemical properties [1, 2]. Considering its small band gap, stable physicochemical properties and resilience to photocorrosion effects, WO₃ has been widely considered as a feasible candidate for visible-light photocatalysts [1–3]. However, several fundamental issues have to be addressed before they are economically available for large scale industrial applications. For example, pure WO₃ is usually not efficient photocatalysts because of the high electron-hole recombination rate and the difficulty in the reduction of oxygen, due to the negative position of its conduction band (CB) [4]. Thus, many efforts have been made to improve the activity of WO₃, such as morphology control, doping, nanostructure construction, and surface modification [4]. One of the most promising ways to accomplish this goal is to design heterogeneous catalysts [5]. So far, various heterogeneous WO₃ based heterogeneous structures, such as WO₃/SiO₂, WO₃/TiO₂, WO₃/NiO, and Pt/TiO₂-WO₃, have been designed toward good catalytic performance [5–12].

Titanium dioxide (TiO₂) has attracted much attention as a suitable semiconductor to construct heterogeneous structures with WO₃, due to its low cost, nontoxicity, and suitable band structure [5, 13–16]. The valence band (VB) and CB potentials of TiO₂ are more cathodic than those of WO₃ [16]. The coupling of TiO₂ and WO₃ can lead to photogenerated electron and hole transfer from one semiconductor particle to another; those are electrons transfer from the CB of TiO₂ down to the CB of WO₃ and holes transfer from the VB of WO₃ to that of TiO₂ [17]. This process suppresses the recombination of photogenerated carriers and leads to improved photocatalytic efficiency of the system [17]. To further increase the photocatalytic performance of the system, metal or metal oxide particles, such as Au, Pt, and CuO, were introduced into the system to promote the reduction reaction of electrons with oxygen molecules, leading to efficient consumption of electrons [10–12]. For example, copper ions modified WO₃/TiO₂ nanocomposites, prepared by Hosogi and Kuroda, exhibited efficient photocatalytic activities [12]. However, there are still many problems in the practical application of these reported catalysts, including the complexity of the preparation procedures, the requirement

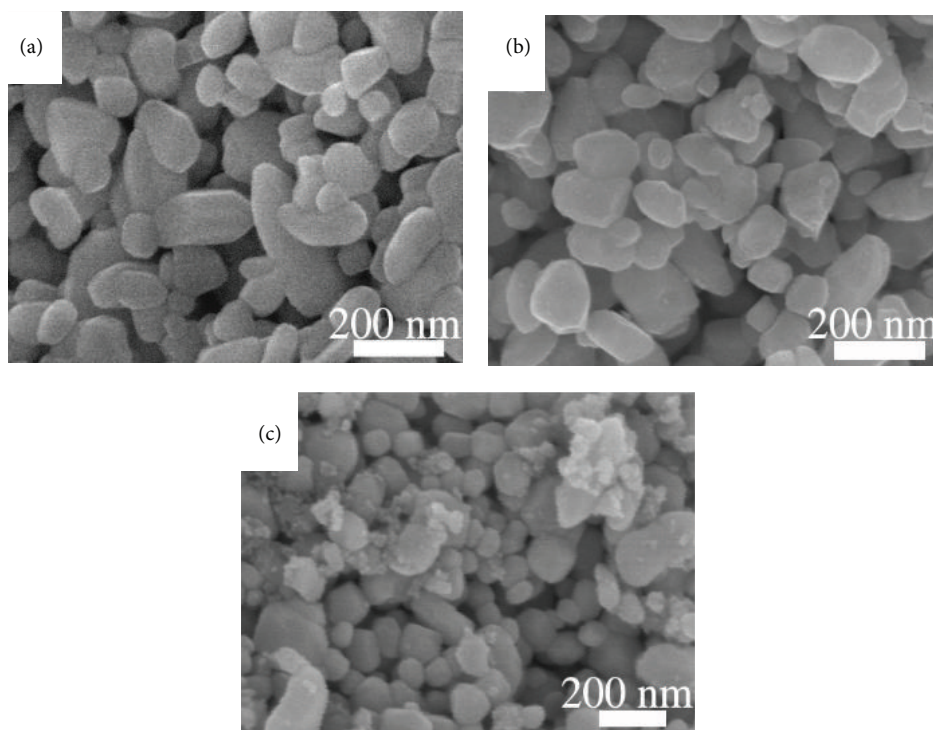


FIGURE 1: SEM images of bare WO_3 (a), Cu(II)-WO_3 (b), and $\text{Cu(II)-WO}_3/\text{TiO}_2$ (c).

for expensive raw materials, and the difficulties for large scale production [5–12]. For instance, sol-gel method and urea as raw materials were needed in the preparation of copper ions modified WO_3/TiO_2 nanocomposites [12]. Thus, efforts aimed at improving the photocatalytic performance and the preparation process of WO_3 are still needed.

In the present work, we reported efficient Cu(II) nanoclusters modified WO_3/TiO_2 nanocomposites ($\text{Cu(II)-WO}_3/\text{TiO}_2$) through a facile preparation process. In this process, Cu(II) nanoclusters were deposited on WO_3 using a simple impregnation method and TiO_2 nanopowders were introduced into the Cu(II) nanoclusters modified WO_3 (Cu(II)-WO_3) by a physical combination method. The introduced Cu(II) nanoclusters and TiO_2 nanopowders functioned as cocatalysts on the surface of WO_3 . Thus, the obtained $\text{Cu(II)-WO}_3/\text{TiO}_2$ products exhibited an enhanced visible light photocatalytic activity.

2. Experimental

2.1. Materials. Commercial tungsten (VI) oxide (Sigma-Aldrich; for monoclinic WO_3 , particle size is ~ 100 nm) was used as the initial WO_3 . $\text{CuCl}_2 \cdot 2\text{H}_2\text{O}$ (Sigma-Aldrich) was used as the source of Cu(II) nanoclusters. Degussa (Evonik) P25 TiO_2 nanopowders (particle size ~ 25 nm) was used as the raw material of TiO_2 . All of these commercial materials were used as received, without further purification. Distilled water was applied in the experimental process.

2.2. Preparation of the Composites. Cu(II) nanoclusters were grafted on the surface of WO_3 by using an impregnation

method, as reported previously [18, 19]. $\text{CuCl}_2 \cdot 2\text{H}_2\text{O}$ was used as the Cu(II) nanoclusters source to prepare Cu(II)-WO_3 . 1 g WO_3 powder with 0.1% weight fraction of Cu to WO_3 was dispersed in 10 mL distilled water. 0.1% weight fraction of Cu to WO_3 has demonstrated the optimized amount of Cu(II) nanoclusters for Cu(II)-WO_3 systems [18]. The suspension was heated at 90°C and stirred for 1 h in a vial reactor to hydrolyze the CuCl_2 source and generate Cu(II) nanoclusters on the surface of WO_3 . Then, the suspension was filtered twice with a membrane filter ($0.025 \mu\text{m}$, Millipore) and washed with sufficient amounts of distilled water. The resulting residue was dried at 110°C for 24 h and subsequently grounded into fine powder using an agate mortar and pestle.

The mixing of Cu(II)-WO_3 with TiO_2 was performed using a physical mixing method. Typically, 1 g Cu(II)-WO_3 powder and 1% weight ratio TiO_2 were mixed in an agate mortar and grounded into fine powder using a pestle for 1 h.

2.3. Sample Characterizations. Scanning electron microscope (SEM) images were taken using a field-emission SEM (FE-SEM, Hitachi S-4800). Photoluminescence PL spectra were obtained by using a Hitachi F-4500 fluorophotometer with an excited wavelength of $\lambda = 325$ nm at room temperature. UV-visible reflectance spectra were obtained by the diffuse reflection method using a spectrometer (UV-2550, Shimadzu). Surface compositions were studied by X-ray photoelectron spectroscopy (XPS; model 5600, Perkin-Elmer). The binding energy data were calibrated with reference to the C 1s signal at 284.5 eV.

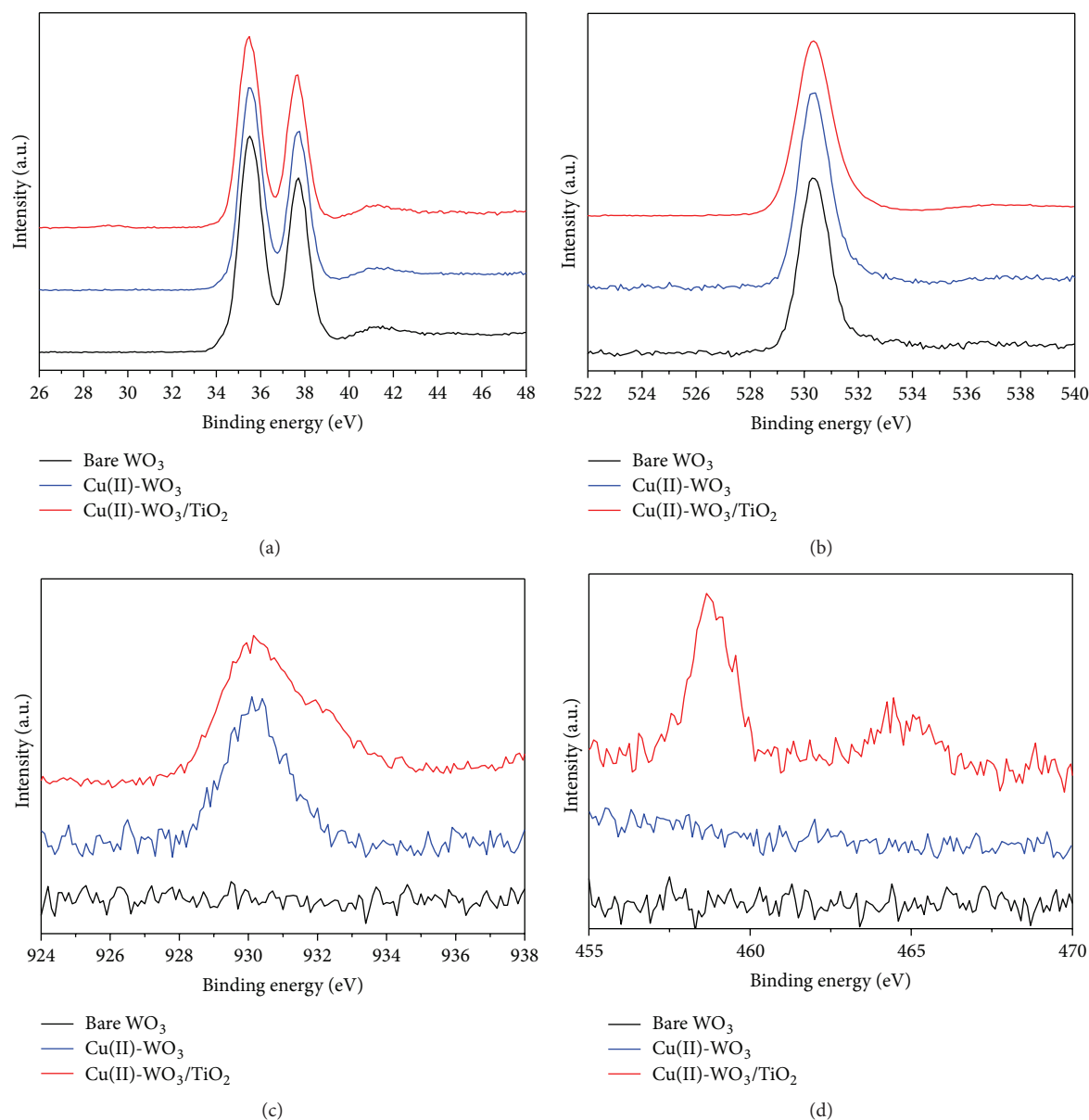


FIGURE 2: (a) W 4f core-level spectra, (b) O 1s core-level spectra, (c) Cu 2p core-level spectra, and (d) Ti 2p core-level spectra of bare WO₃, Cu(II)-WO₃, and Cu(II)-WO₃/TiO₂, respectively.

2.4. Catalytic Activity Testing. Photocatalytic activity of the WO₃ samples was evaluated in terms of the decolorization of methylene blue (MB) dye under visible irradiation. 20 mg sample was dispersed into 100 mL of 10 mg/L MB solution and stirred in the dark for 1 h to reach a complete adsorption-desorption equilibrium. Then the solution was irradiated with $\sim 20 \text{ mW/cm}^2$ visible light ($>420 \text{ nm}$, with a light filter L42 (Asahi Techno-Glass)) under continuous stirring. With a given irradiation time interval, some specimens (5 mL) were taken from the dispersion and were centrifuged (4000 rpm). The clear upper solution was subjected to UV-Vis spectrophotometer (UV-2550, Shimadzu). The concentration of MB was determined from the absorbance at the wavelength of 665 nm.

3. Results

Figure 1 shows the SEM images of the obtained samples. It can be seen that the bare WO₃ samples contained many particles. These particles have a clear surface and a size of $\sim 100 \text{ nm}$. After Cu(II) nanoclusters grafting, the particle morphology still remained, indicating the grafting of Cu(II) nanoclusters did not affect its morphology (Figure 1(b)). After the modification with TiO₂ nanopowders, some small particles could be observed in TiO₂ mixed Cu(II)-WO₃ (Cu(II)-WO₃/TiO₂) samples (Figure 1(c)). These small particles have a size around several tens of nanometers, coinciding with the size of TiO₂ nanopowders. In the paper, except specially noted, the weight ratios of Cu and TiO₂ to WO₃ were set to 0.1% and 1%, respectively,

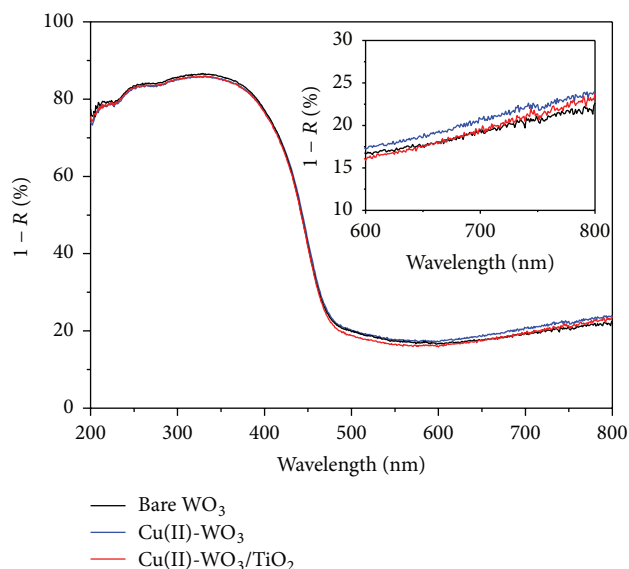


FIGURE 3: UV-visible reflectance spectra of bare WO₃, Cu(II)-WO₃, and Cu(II)-WO₃/TiO₂, respectively. Inset is the enlarged UV-visible reflectance spectra at range of 600–800 nm.

In order to determine the surface composition and chemical states of the surface elements, XPS spectra were recorded, as shown in Figure 2. In the W 4f and O 1s core-level spectra of the samples (Figures 2(a) and 2(b)), no obvious differences could be seen in the chemical states of elements W and O, demonstrating that neither the surface grafting of Cu(II) nanoclusters nor physical mixing of TiO₂ powders affected the bonding structure between tungsten and oxygen. In the Cu 2p core-level spectra (Figure 2(c)), Cu signals were clearly observed in Cu(II)-grafted samples, such as Cu(II)-WO₃ and Cu(II)-WO₃/TiO₂, confirming that Cu(II) was successfully grafted on the surface of WO₃, while, in the Ti 2p core-level spectra (Figure 2(d)), Ti signal was only observed in Cu(II)-WO₃/TiO₂ composites, indicating the TiO₂ was well mixed with WO₃ powders.

Figure 3 shows the UV-Vis of the samples. It clearly shows that WO₃ has a good visible light absorption property, indicating it is a potential visible light photocatalyst. The absorption edge of WO₃ is located at ~460 nm, which corresponds to the interband transition of WO₃ [18]. This interband absorption indicates a band gap of ~2.7 eV, which coincides with the reported values of 2.7 eV for WO₃ [20, 21]. After Cu(II) nanoclusters grafting, an additional light absorption at the range of ~700–800 nm was clearly superimposed on the light absorption of WO₃, as shown in the inset of Figure 3. This additional light absorption can be attributed to the d-d transition of Cu(II) [18]. After further modification with TiO₂ powders, the interband transition of WO₃ was not changed, due to the small amount of TiO₂ powders and their large band gap [13–15]. Notably, the additional visible light absorption caused by the d-d transition of Cu(II) can still be observed in the mixed nanocomposites, proving the existence of Cu(II) nanoclusters (inset of Figure 3).

Figure 4 represents the variation of MB concentration by photocatalytic reaction with the samples under visible light (>420 nm) irradiation. Typical evolution of MB concentration during photocatalytic reaction on Cu(II)-WO₃/TiO₂ is presented in Figure 4(a). Under light irradiation, the characteristic MB absorption peak decreased sharply and almost no color was observed after 90 minutes of irradiation, indicating that MB was completely degraded by Cu(II)-WO₃/TiO₂. Comparative studies among bare WO₃, Cu(II)-WO₃, and Cu(II)-WO₃/TiO₂ show that bare WO₃ has a negligible activity under visible light irradiation (Figure 4(b)). The grafting of Cu(II) nanoclusters to the surface switched its photocatalytic activity. It can be seen that MB dye was almost degraded by Cu(II)-WO₃ with 2 h of visible light irradiation. Interestingly, after further modification with TiO₂ nanopowders, Cu(II)-WO₃/TiO₂ exhibited an enhanced photocatalytic activity compared with that of Cu(II)-WO₃. MB dye was completely degraded by Cu(II)-WO₃/TiO₂ nanocomposites with 1.5 h of visible light irradiation, revealing the high photocatalytic activity of the Cu(II)-WO₃/TiO₂ nanocomposites. Figure 4(c) shows the pseudo-first-order kinetic rate for the photochemical degradation of MB by Cu(II)-TiO₂ samples. The pseudo-first-order kinetic rate was calculated according to the equation of $\ln(C_0/C) = kt$, where C/C_0 is the normalized MB concentration, t is the reaction time, and k is the pseudo-first-rate constant. It can be seen that the Cu(II)-WO₃/TiO₂ samples presented the highest reaction rate. The reaction rate was sharply decreased when bare WO₃ was used. The result was consistent with the MB decomposition curves in Figure 4(b). Figure 4(d) shows the cycling measurements of MB decomposition over Cu(II)-WO₃/TiO₂. Similar k values were obtained after 5-cycle measurements, suggesting a good stability for the photocatalytic application of Cu(II)-WO₃/TiO₂.

We also investigated the influences of experimental parameters on the photocatalytic performances of Cu(II)-WO₃/TiO₂ samples. Figure 5 shows the photocatalytic performances of Cu(II)-WO₃/TiO₂ samples with different ratios of TiO₂. It can be seen that the activity of the samples was increased with the ratio of TiO₂ to WO₃ in the beginning. After the highest activity was achieved at the ratio of 1%, the photocatalytic activity was decreased again with the increase of ratio. These results revealed that the Cu(II)-WO₃/TiO₂ samples obtained with 1% TiO₂ have the optimum amount of TiO₂ for hole separation and reaction. It has been reported that the amount of TiO₂ to mix with WO₃ was important for the photocatalytic reaction [22, 23]. Thus, the Cu(II)-WO₃/TiO₂ samples with a TiO₂ ratio of 1% exhibited the highest photocatalytic performance.

4. Discussions

Figure 6 shows the energy levels of TiO₂ and WO₃ [18]. TiO₂, as one of the most efficient photocatalysts, has a high potential CB and a deep VB. Thus, electrons in its CB have sufficient reduction power for oxygen reaction with single electron and holes in its VB have large oxidation power for organic compounds decomposition, respectively. Consequently, TiO₂ has a very high efficiency for photocatalytic reactions under

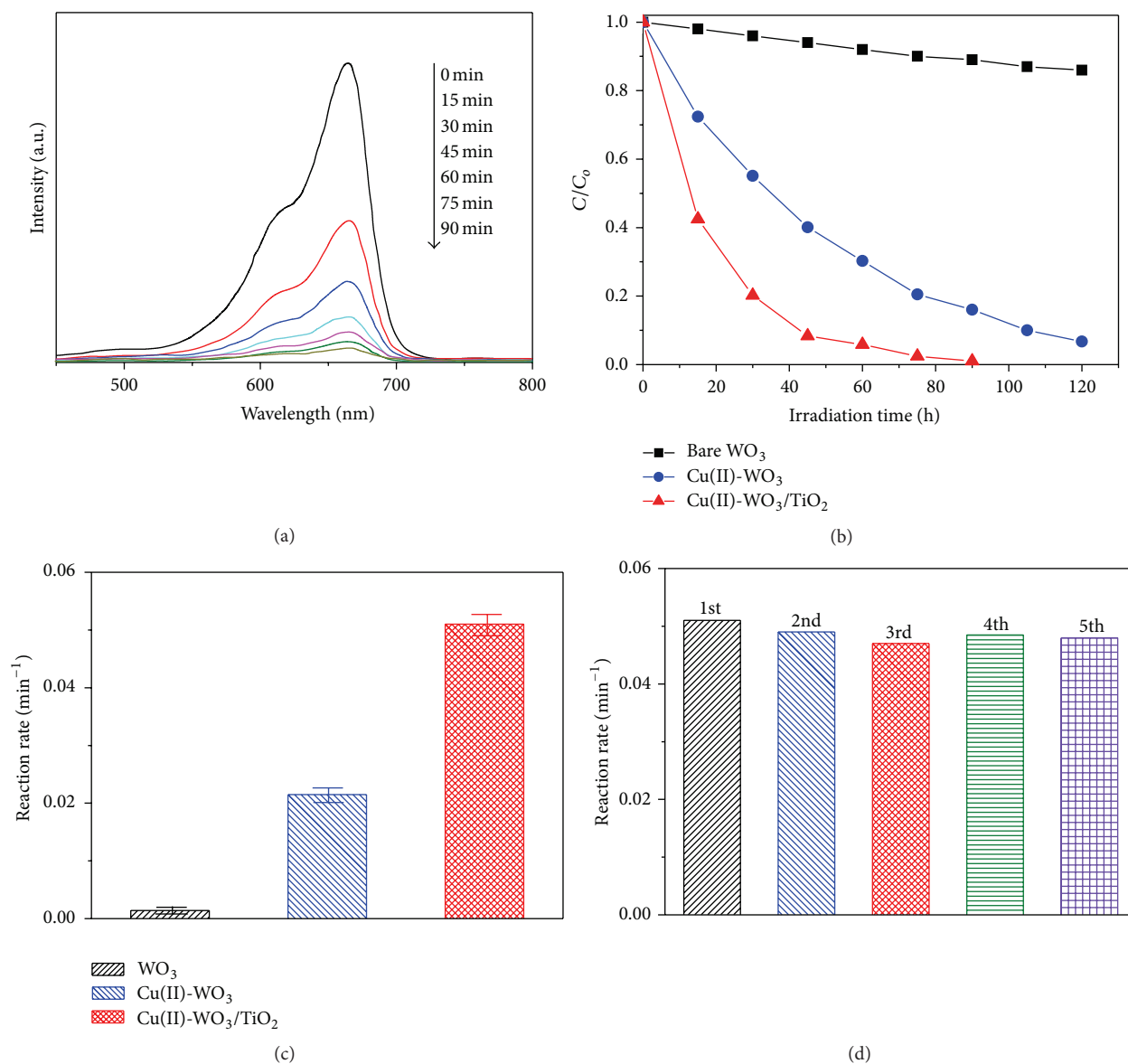


FIGURE 4: (a) Absorption spectra for MB degradation using Cu(II)-WO₃/TiO₂. (b) The variation of MB concentration by photocatalytic reaction with bare WO₃, Cu(II)-WO₃, and Cu(II)-WO₃/TiO₂, respectively. (c) The pseudo-first-order kinetic rates with error bars for the photochemical degradation of MB by bare WO₃, Cu(II)-WO₃, and Cu(II)-WO₃/TiO₂, respectively. (d) Cycling measurements of MB decomposition over Cu(II)-WO₃/TiO₂.

UV light irradiation. However, TiO₂ can only be activated under UV light irradiation, owing to its large band gap. WO₃ is sensitive to visible light because of its proper band gap, 2.7 eV [20, 21]. Notably, both the CB and VB positions of WO₃ are more positive than those of TiO₂. As a result, photogenerated electrons can be transferred from the CB of TiO₂ to the CB of WO₃ and photogenerated holes can be transferred from the VB of WO₃ to that of TiO₂ [17]. Moreover, if photons do not have enough energy to excite TiO₂ but have enough energy to excite WO₃, hole in the VB of WO₃ is still possibly transferred to the VB of TiO₂ [24]. This process suppresses the recombination of photogenerated carriers and indicates that TiO₂ can act as hole cocatalyst [12, 17, 24]. On the other hand, the CB potential of WO₃ is lower

than the potential for reduction reaction of oxygen molecules, leading to the insufficient consumption of electrons in CB. When Cu(II) nanoclusters were modified on the surface of WO₃, the photogenerated electrons in the CB of WO₃ can be transferred to the Cu(II) nanoclusters. The transferred electrons can be consumed by multielectron reduction reactions with oxygen molecules in the Cu(II) nanoclusters [18, 19]. In other words, Cu(II) nanoclusters function as efficient electron cocatalysts [12, 18, 19]. Consequently, the activity of Cu(II)-WO₃ can be further enhanced by combining with TiO₂.

Figure 7 shows the PL spectra of bare WO₃, Cu(II)-WO₃, and Cu(II)-WO₃/TiO₂, respectively. The main emission peak for WO₃ is centered at about 460 nm, which is approximately equal to the band gap energy of WO₃ [20, 25]. It worth noting

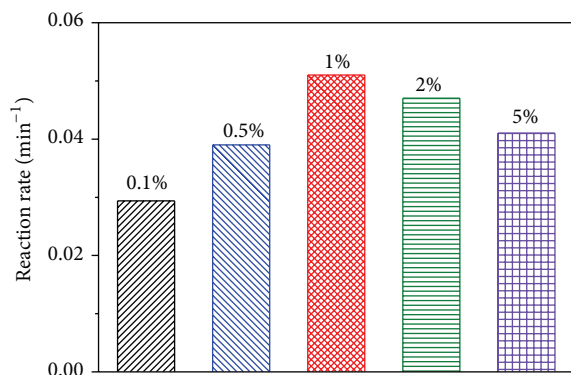


FIGURE 5: Photocatalytic activities of Cu(II)-WO₃/TiO₂ samples with different ratios of TiO₂.

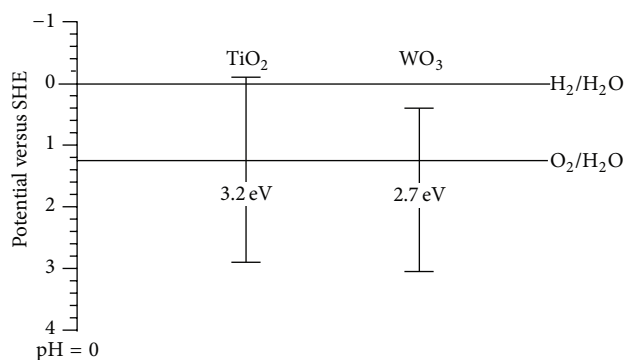


FIGURE 6: Energy levels of TiO₂ and WO₃.

that bare WO₃ exhibited the highest PL intensity among these samples, indicating the highest recombination rate of electrons and holes [26]. After the Cu(II) nanoclusters were grafted, the intensity of the PL emission decreases, which can be attributed to the decrease of the efficient electron trapping and consumption on Cu(II) nanoclusters [18, 19]. The emission intensity of the Cu(II)-WO₃/TiO₂ was lower than that of bare WO₃ and Cu(II)-WO₃, which indicated that the recombination rate of photogenerated charge carriers was the lowest in the Cu(II)-WO₃/TiO₂. The PL results confirmed the importance of the modification of Cu(II) nanoclusters and TiO₂ nanopowders for hindering the recombination of electrons and holes. Thus, efficient visible light photocatalytic activity can be achieved in Cu(II) and TiO₂ modified WO₃.

5. Conclusions

Efficient WO₃ photocatalysts were prepared by being simply surface modified with Cu(II) nanoclusters and TiO₂ nanopowders. In this prepared system, Cu(II) nanoclusters and TiO₂ nanopowders were deposited on the surface of WO₃ using a simple impregnation method and a physical combination method, respectively. Cu(II) nanoclusters and TiO₂ nanopowders functioned as efficient cocatalysts on the surface of WO₃, which acted as photocatalyst. Thus, efficient charge separations and reactions can be achieved in this Cu(II)-WO₃/TiO₂ system, resulting in efficient visible light

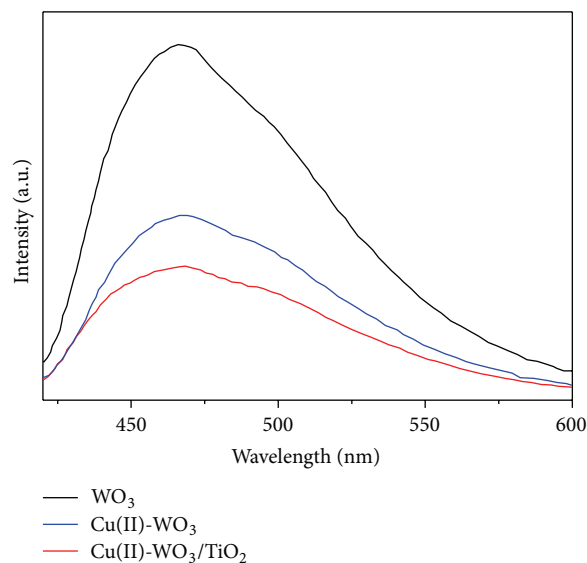


FIGURE 7: PL spectra of bare WO₃, Cu(II)-WO₃, and Cu(II)-WO₃/TiO₂, respectively.

photocatalytic reaction for organic compounds decomposition. The simple strategy opens an avenue for designing efficient visible-light-active photocatalysts for practical application.

Conflict of Interests

The authors declare that there is no conflict of interests regarding the publication of this paper.

Acknowledgments

This work was supported by the Scientific Research Fund of Hunan Provincial Education Department under Grant no. 09A083 and the Science and Technology Fund of Hunan Provincial Science and Technology Department under Grant no. 2012FJ4137.

References

- [1] J. Zhou, Y. Ding, S. Z. Deng, L. Gong, N. S. Xu, and Z. L. Wang, "Three-dimensional tungsten oxide nanowire networks," *Advanced Materials*, vol. 17, no. 17, pp. 2107–2110, 2005.
- [2] G. C. Xi, Y. Yan, Q. Ma et al., "Synthesis of multiple-shell WO₃ hollow spheres by a binary carbonaceous template route and their applications in visible-light photocatalysis," *Chemistry*, vol. 18, no. 44, pp. 13949–13953, 2012.
- [3] D. L. Chen, L. Gao, A. Yasumori, K. Kuroda, and Y. Sugahara, "Size- and shape-controlled conversion of tungstate-based inorganic-organic hybrid belts to WO₃ nanoplates with high specific surface areas," *Small*, vol. 4, no. 10, pp. 1813–1822, 2008.
- [4] X. An, J. C. Yu, Y. Wang, Y. Hu, X. Yu, and G. Zhang, "WO₃ nanorods/graphene nanocomposites for high-efficiency visible-light-driven photocatalysis and NO₂ gas sensing," *Journal of Materials Chemistry*, vol. 22, no. 17, pp. 8525–8531, 2012.
- [5] X.-L. Yang, W.-L. Dai, C. W. Guo et al., "Synthesis of novel core-shell structured WO₃/TiO₂ spheroids and its application

- in the catalytic oxidation of cyclopentene to glutaraldehyde by aqueous H_2O_2 ,” *Journal of Catalysis*, vol. 234, no. 2, pp. 438–450, 2005.
- [6] A. Spamer, T. I. Dube, D. J. Moodley, C. van Schalkwyk, and J. M. Botha, “Application of a WO_3/SiO_2 catalyst in an industrial environment: part II,” *Applied Catalysis A: General*, vol. 255, no. 2, pp. 133–142, 2003.
- [7] R. H. Jin, X. Xia, W. L. Dai, J. F. Deng, and H. X. Li, “An effective heterogeneous $\text{WO}_3/\text{TiO}_2\text{-SiO}_2$ catalyst for selective oxidation of cyclopentene to glutaraldehyde by H_2O_2 ,” *Catalysis Letters*, vol. 62, no. 2–4, pp. 201–207, 1999.
- [8] M. Bao, Y. J. Chen, F. Li et al., “Plate-like p-n heterogeneous NiO/WO_3 nanocomposites for high performance room temperature NO_2 sensors,” *Nanoscale*, vol. 6, no. 8, pp. 4063–4066, 2014.
- [9] A. K. Nayak, R. Ghosh, S. Santra, P. K. Guha, and D. Pradhan, “Hierarchical nanostructured $\text{WO}_3\text{-SnO}_2$ for selective sensing of volatile organic compounds,” *Nanoscale*, vol. 7, no. 29, pp. 12460–12473, 2015.
- [10] M.-H. Chen, C.-S. Lu, and R.-J. Wu, “Novel $\text{Pt}/\text{TiO}_2\text{-WO}_3$ materials irradiated by visible light used in a photoreductive ozone sensor,” *Journal of the Taiwan Institute of Chemical Engineers*, vol. 45, no. 3, pp. 1043–1048, 2014.
- [11] R.-J. Wu, Y.-C. Chiu, C.-H. Wu, and Y.-J. Su, “Application of $\text{Au}/\text{TiO}_2\text{-WO}_3$ material in visible light photoreductive ozone sensors,” *Thin Solid Films*, vol. 574, pp. 156–161, 2015.
- [12] Y. Hosogi and Y. Kuroda, “Tungsten oxide photocatalyst and method for producing the same,” US Patent, US 8652991 B2, 2014.
- [13] T. L. Thompson and J. T. Yates Jr., “Surface science studies of the photoactivation of TiO_2 —new photochemical processes,” *Chemical Reviews*, vol. 106, no. 10, pp. 4428–4453, 2006.
- [14] X. Chen and S. S. Mao, “Titanium dioxide nanomaterials: synthesis, properties, modifications and applications,” *Chemical Reviews*, vol. 107, no. 7, pp. 2891–2959, 2007.
- [15] H. Li, Y. Zeng, T. Huang, L. Piao, and M. Liu, “Controlled synthesis of anatase TiO_2 single crystals with dominant {001} facets from TiO_2 powders,” *ChemPlusChem*, vol. 77, no. 11, pp. 1017–1021, 2012.
- [16] M. Liu, H. Li, Y. Zeng, and T. Huang, “Anatase TiO_2 single crystals with dominant {001} facets: facile fabrication from Ti powders and enhanced photocatalytic activity,” *Applied Surface Science*, vol. 274, pp. 117–123, 2013.
- [17] M. M. Khan, M. O. Ansari, D. H. Han, and M. H. Cho, “Band gap engineered TiO_2 nanoparticles for visible light induced photoelectrochemical and photocatalytic studies,” *Journal of Materials Chemistry A*, vol. 2, pp. 637–644, 2014.
- [18] H. Irie, S. Miura, K. Kamiya, and K. Hashimoto, “Efficient visible light-sensitive photocatalysts: grafting Cu(II) ions onto TiO_2 and WO_3 photocatalysts,” *Chemical Physics Letters*, vol. 457, pp. 202–204, 2008.
- [19] H. Irie, K. Kamiya, T. Shibanuma et al., “Visible light-sensitive Cu(II) -grafted TiO_2 photocatalysts: activities and X-ray absorption fine structure analyses,” *Journal of Physical Chemistry C*, vol. 113, no. 24, pp. 10761–10766, 2009.
- [20] G. R. Bamwenda, K. Sayama, and H. Arakawa, “The effect of selected reaction parameters on the photoproduction of oxygen and hydrogen from a $\text{WO}_3\text{-Fe}^{2+}\text{-Fe}^{3+}$ aqueous suspension,” *Journal of Photochemistry and Photobiology A: Chemistry*, vol. 122, no. 3, pp. 175–183, 1999.
- [21] T. Arai, M. Yanagida, Y. Konishi, Y. Iwasaki, H. Sugihara, and K. Sayama, “Efficient complete oxidation of acetaldehyde into CO_2 over $\text{CuBi}_2\text{O}_4/\text{WO}_3$ composite photocatalyst under visible and UV light irradiation,” *The Journal of Physical Chemistry C*, vol. 111, no. 21, pp. 7574–7577, 2007.
- [22] W. Smith, A. Wolcott, R. C. Fitzmorris, J. Z. Zhang, and Y. Zhao, “Quasi-core-shell TiO_2/WO_3 and WO_3/TiO_2 nanorod arrays fabricated by glancing angle deposition for solar water splitting,” *Journal of Materials Chemistry*, vol. 21, no. 29, pp. 10792–10800, 2011.
- [23] J. Papp, S. Soled, K. Dwight, and A. Wold, “Surface acidity and photocatalytic activity of TiO_2 , WO_3/TiO_2 , and $\text{MoO}_3/\text{TiO}_2$ photocatalysts,” *Chemistry of Materials*, vol. 6, no. 4, pp. 496–500, 1994.
- [24] S. Y. Chai, Y. J. Kim, and W. I. Lee, “Photocatalytic WO_3/TiO_2 nanoparticles working under visible light,” *Journal of Electroceramics*, vol. 17, no. 2–4, pp. 909–912, 2006.
- [25] T. Arai, M. Yanagida, Y. Konishi, Y. Iwasaki, H. Sugihara, and K. Sayama, “Efficient complete oxidation of acetaldehyde into CO_2 over $\text{CuBi}_2\text{O}_4/\text{WO}_3$ composite photocatalyst under visible and UV light irradiation,” *Journal of Physical Chemistry C*, vol. 111, no. 21, pp. 7574–7577, 2007.
- [26] L. L. Chen, W. X. Zhang, C. Feng, Z. H. Yang, and Y. M. Yang, “Replacement/etching route to ZnSe nanotube arrays and their enhanced photocatalytic activities,” *Industrial and Engineering Chemistry Research*, vol. 51, no. 11, pp. 4208–4214, 2012.

Research Article

Photocatalysis of Yttrium Doped BaTiO₃ Nanofibres Synthesized by Electrospinning

Zhenjiang Shen,^{1,2} Yu Wang,² Wanping Chen,² Helen Lai Wah Chan,² and Lina Bing¹

¹College of Physics and Electronic Engineering, Hainan Normal University, Hainan 571158, China

²Department of Applied Physics and Materials Research Center, The Hong Kong Polytechnic University, Hung Hom, Kowloon, Hong Kong

Correspondence should be addressed to Zhenjiang Shen; zjshenmail@163.com

Received 18 December 2014; Accepted 25 January 2015

Academic Editor: Zijie Yan

Copyright © 2015 Zhenjiang Shen et al. This is an open access article distributed under the Creative Commons Attribution License, which permits unrestricted use, distribution, and reproduction in any medium, provided the original work is properly cited.

Yttrium doped barium titanate (BT) nanofibres (NFs) with significant photocatalytic effect were successfully synthesized by electrospinning. Considering the necessary factors for semiconductor photocatalysts, a well-designed procedure was carried out to produce yttrium doped BT (BYT) NFs. In contrast to BYT ceramics powders and BT NFs, BYT NFs with pure perovskite phase showed much enhanced performance of photocatalysis. The surface modification in electrospinning and subsequent annealing, the surface spreading of transition metal yttrium, and the narrowed band gap energy in yttrium doping were all contributed to the final novel photocatalytic effect. This work provides a direct and efficient route to obtain doped NFs, which has a wide range of potential applications in areas based on complex compounds with specific surface and special doping effect.

1. Introduction

Issues related to environmental protection are increasingly important with the industrial advance [1]. Photocatalysis by semiconductor oxides is a significant way to degrade organic and inorganic pollutants [2, 3]. One of the most famous photocatalysts is TiO₂ [4]. It has showed excellent photocatalytic effect as reported [5]. It is generally accepted that surface defects of TiO₂ play an essential part in photocatalysis [6, 7]. In fact, one-dimensional (1D) nanomaterials such as NFs can perform better photocatalysis for their high specific surface area. Electrospinning has been proved to be an effective technique to prepare NFs with the merits of mass production and high continuity [8, 9]. During electrospinning and subsequent annealing, the volatile solvents which containing polymer could experience rapid phase separation and decomposition. So the final NFs usually have rough and defective morphology. Producing NFs by electrospinning can be a practical way to improve the photocatalytic efficiency. In this trend, many researches on the photocatalysis of NFs obtained by electrospinning were carried out [10, 11]. However, famous photocatalysts such as TiO₂ and ZnO were

still the main objects in these researches, while many other important compounds received few attentions.

Apart from the famous photocatalysts, many other doped semiconductors also possess brilliant photocatalytic properties. The suitable band gap is another important deciding factor in semiconductor photocatalysts [1–3, 12]. The doping can effectively narrow the band gap to obtain a better photocatalytic effect. As an important material [13, 14], BT has excellent environmental compatibility, since its excellent performance is with harmful elements abandoning. Because BT has a similar band gap with TiO₂, researches on the BT-based photocatalysts are also growing [15]. However, due to the unfitted band gap, the photocatalytic efficiency of BT did not perform as well as famous photocatalysts. So BT was always used as an auxiliary component, while the investigations on its intrinsic photocatalysis did not operate specially [16]. In particular, doped semiconductor BT is a good candidate to exploit novel properties for its adjustable composition. To improve the original properties of BT, transition metal yttrium was usually doped to tailor the properties, especially in the semiconductor BT with narrowed band gap [17, 18]. Moreover, it is well known that

transition metal elements spread easily on the surface of oxides [19, 20]. Actually the distribution of doping elements is a key reason to achieve interesting photocatalysis in doped semiconductor. Researches on doped TiO_2 pointed out that transition metal elements surface doping could produce more efficient photocatalysts than traditional bulk doping [21]. So the transition metal yttrium doping can enhance a desirable surface reaction. Considering the morphology features of NFs, the narrowed band gap of yttrium doping, and the surface spreading of yttrium ions, semiconductor BYT NFs with modified surface could be obtained by electrospinning. It is reasonable to believe that this can cause novel photocatalysis effects which are based on surface defects and band gap. This can provide an unexplored method in the doped semiconductor photocatalysis.

In this paper, we will report observing photocatalytic behavior in BYT NFs, which were synthesized by electrospinning. Results show the photocatalytic efficiency of BYT NFs has been greatly improved in this method. Besides, BYT ceramics powders and undoped BT NFs are also discussed.

2. Experimental Methods

The electrospinning was carried out as follows: 6 g of barium acetate [$\text{Ba}(\text{CH}_3\text{COO})_2$], titanium butoxide [$\text{C}_{16}\text{H}_{36}\text{O}_4\text{Ti}$], and yttrium acetate tetrahydrate [$\text{Y}(\text{CH}_3\text{COO})_3 \cdot 4\text{H}_2\text{O}$] were weight and mixed according to stoichiometric ratio of 1:1:0.02. 40 mL of dichloromethane was used as solvent for its rapid evaporation. To prevent hydrolyzation, 5 mL of acetic acid was added. To adjust the viscosity, 8 g PVP was dissolved into the precursor solution. The electrospinning was conducted through a needle with an inner diameter of 0.5 mm attached to a 20 mL syringe. The flow rate was set at 4 mL/h by a syringe pump. The applied voltage for electrospinning was 1.6 kV and the distance between the tip and the collector was 12 cm. Then as-spun NFs could be deposited on sapphire single crystal substrates which attached to the grounded collector. After annealed in relative high temperature of 1250°C for 2 hours with heating rate of 6°C/min, BYT NFs were obtained. Besides, BT NFs without Y doped were also synthesized in the same procedure. And a group of BYT ceramics powders which were prepared by solid reaction using BaCO_3 [99.9%], TiO_2 [99.9%], and Y_2O_3 [99.9%] were also measured in the characterizations. Regents and chemicals in this work were purchased from Sinopharm Chemical Reagents Co., Ltd. (China). Single crystal substrates were from KMT Corporation (Hefei, China).

The structure and microstructure of the NFs were characterized by X-ray diffraction (Philips X-ray diffractometer system), field-emission scanning electron microscopy (FESEM, JEOL JSM-6700F equipped with selected area electron diffraction and an energy-dispersive X-ray spectroscopy). The UV adsorption spectra were measured using a Shimadzu UV-2550 (Kyoto, Japan) spectrophotometer. The photocatalytic activity of the NFs for degradation of methylene blue (MB) was evaluated by agitating the solution and irradiating the samples using a 250 W high-pressure Hg lamp. The initial concentration of MB was 6 mg/L and with a catalyst loading of 1 g/L for measurement.

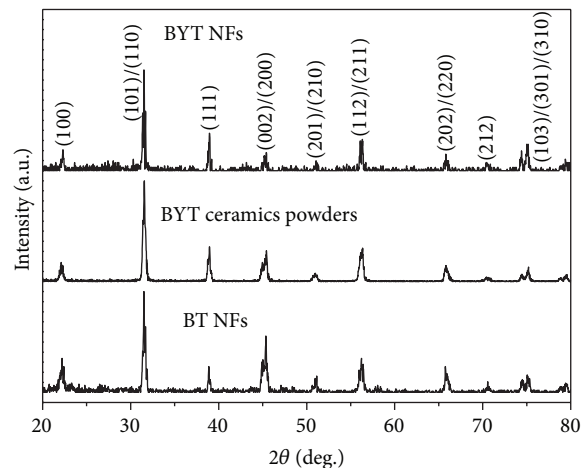


FIGURE 1: The X-ray diffraction pattern of BYT NFs, BYT ceramics powders, and BT NFs.

3. Results and Discussion

In the characterizations, we measured three groups of samples: BYT NFs, BYT ceramics powders, and BT NFs. Figure 1 shows XRD patterns of three groups. For BYT NFs and BT NFs, the as-annealed products were using a long collection time for 2 h. Three groups are all of pure perovskite phase. But BYT NFs and BT NFs are with a stronger noise. In the NFs XRD measurement in this work, the annealed products were from as-spun precursor with long collection time of 2 h. After annealing, NFs were obtained and pressed on the sample stage for XRD measurement. However, the flow rate was kept at 4 mL/h and with low metal compound concentration (6 g metal acetates dissolved into 40 dichloromethane which were added with 5 mL of acetic acid) in electrospinning. So even the as-spun NFs had been collected for a longtime, the as-annealed products were not enough to ensure strong diffraction intensity in XRD measurement. So the XRD patterns of NFs are noisy unavoidably. Nevertheless, all the main diffraction peaks in XRD patterns of BYT NFs and BYT ceramics powders have been indexed. They are all matching the BT tetragonal perovskite phase. It draws the dopant Y_2O_3 which has been incorporated into host so no impurity phase is observed. It means that BT-based NFs with high perovskite phase purity and crystallinity can be obtained by electrospinning.

Figures 2(a)-2(b) show the morphology of as-annealed BYT NFs samples. NFs with typical wire-like state with diameter less than 200 nm can be clearly observed in the images. But the diameters are not homogeneous because of the fulmination and multilayer effect in electrospinning. Besides, narrow flat ribbons, branched and broken fibers which formed in electrospinning and annealing can also be detected. Most importantly, it can be seen from Figure 2(b) that all of the NFs have rough surface as expected. Further, to determine the chemical composition of NFs, EDX measurements were taken on a single fibre in Figure 2(b). From the spectrum shown in Figure 2(c), yttrium, barium, titanate, aluminum, and oxygen peaks can be detected. The existing

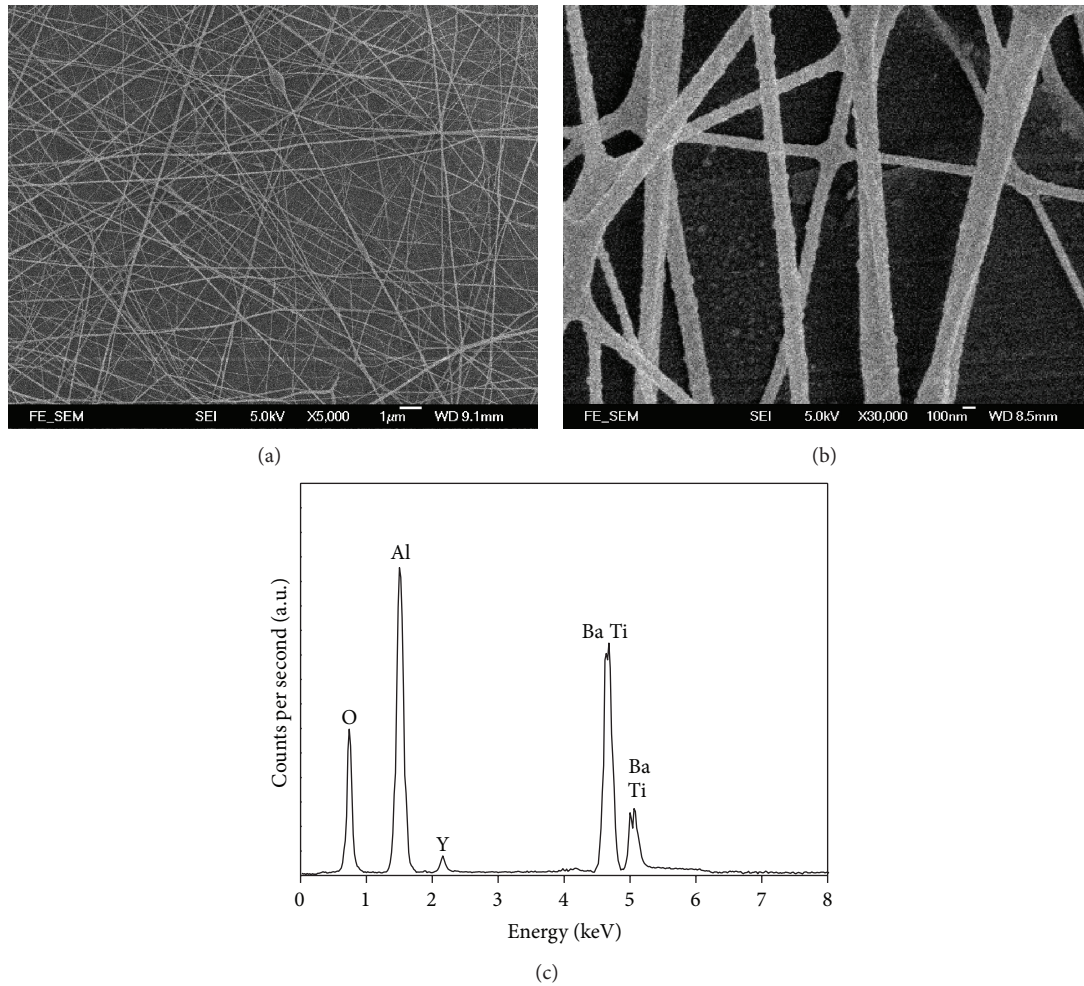


FIGURE 2: ((a)-(b)) FE-SEM image of BYT NFs, (c) EDX spectrum of a single BYT NFs.

diffraction peak of yttrium proves that this doping element has been dissolved into host BT. The content of Al is too high because sapphire single crystal was used as substrate.

In similar researches on the electrospinning preparation of 1D nanostructure materials, both NFs and nanotubes (NTs) were obtained. Heating rate and annealing temperature in annealing processes were pointed as key determinants in the formation of these different structures. In the NTs formation [22, 23], metal oxides shell must form firstly when the decomposition of PVP is unfinished. This means that the heating rate and thermal anchoring of precursor must be controlled to minimize sample overheating. In contrast, the formation of NFs needs faster heating rate and higher annealing temperature. They will all lead to sample overheating, which result in the skipping of the oxide shell formation before PVP remove completely. For this reason, we sped up the heating rate and raised the annealing temperature to meet the NFs formation condition. So NFs were fabricated finally.

The photocatalytic activities of BYT NFs, BYT ceramics powders, and BT NFs were evaluated by decomposing MB under irradiation of medium-pressure Hg lamp for 10 hours. Two groups of MB solution with no catalysts and P25 TiO₂

were also treated as contrast. MB is usually used as standard dyes in photocatalytic testing for its photostability. Figure 3 shows photodegradation of MB solutions function of reaction time for different catalysts. In the photocatalysis measurement, we took groups of photodegraded solution after each hour and then used the spectrophotometer to measure the UV adsorption spectra. C_0 and C_t represent the intensity of the maximum absorption peaks of the UV adsorption spectra of solution initially and at time t . Take nature logarithm function of ratio C_0/C_t to obtain the ordinate in Figure 3. It should be noted that the maximum absorption peak wavelength of MB is usually taken at 664 nm [24]. But this wavelength can blue shift to lower value with the degradation of MB. In order to accurately show the photocatalytic effect, we took the intensity of the exact maximum absorption peak at different wavelengths nearby 664 nm every time. MB solution with no catalysts is stable under irradiation. The MB solution used BT NFs as photocatalyst shows a small scale change during the 10 hours' irradiation. Moreover, in the presence of BYT ceramics powders, the MB concentration decreased a little more obviously after 10 hours' irradiation. However, BYT NFs show remarkable photocatalytic efficiency. A much stronger

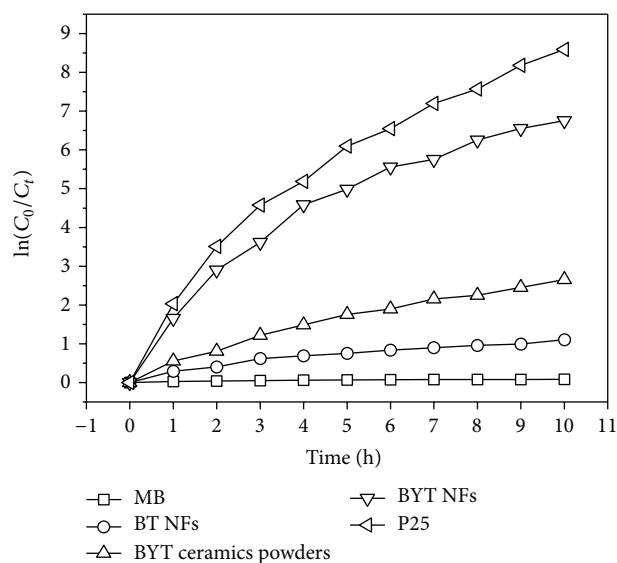


FIGURE 3: The photodegradation of MB solution with different catalysts: no catalysts, BT NFs, BYT ceramics powders, BYT NFs, and P25 TiO₂.

degradation is performed in the presence of BYT NFs. Almost all dyes had been degraded after 10 hours, very close to the group with P25. So it can be concluded that BYT NFs have a significant photocatalytic effect, compared to BYT ceramics powders and BT NFs.

When the semiconductor catalysts were irradiated with energy higher or equal to the band gap, excited state conduction-band electrons and valence-band holes would form [2]. Then the electrons and holes could be got trapped in metastable surface states to recombine or react with electron donors and electron acceptors adsorbed on the semiconductor surface or within the surrounding electrical double layer of the charged particles. But the recombination could be prevented if a suitable scavenger or surface defect state is available to trap the electrons or holes. Subsequently, the electrons and holes generated by exciting photons could have redox reaction with dyes in the solutions. It means that suitable band gap energy is a key reason in photocatalysis. As recorded most commonly, the band gap energy for BT is 3.2 eV and for TiO₂ is 3 eV [2, 13, 25, 26]. Considering the unfitted band gap energy, BT NFs show little photocatalysis effect. But for BYT, when Y₂O₃ doped into BT, yttrium will transform BT to semiconductor. The band gap must be narrowed in the semiconductor BYT, just as shown in Figure 4. It means that BYT could become a more suitable candidate in photocatalysis. So the photocatalytic efficiency has been enhanced obviously in BYT ceramics powders.

At the same time, a strong contrast between the photocatalytic activities of BYT NFs and BYT ceramics powders was also obvious in Figure 3. BYT NFs synthesized by electrospinning show almost as high photocatalytic efficiency as P25, while BYT ceramics powders show a little effect. We ascribe this to the modified surface of NFs in electrospinning. As discussed above, the excited state conduction-band electrons and valence-band holes were trapped in metastable

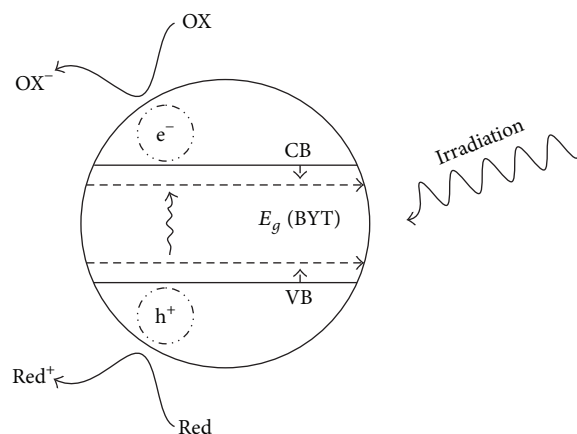


FIGURE 4: Representation of photodegradation of MB solution with BYT.

surface states in the reaction. Catalysts with surface defects are suitable scavengers to trap the electrons or holes in photocatalysis. It indicates that specific surface plays an important role. In fact, surface defects were pointed as the direct reason in photocatalysis. Oxygen vacancy defects on the surface are not only the oxidizing reagents but also the electron scavengers which ultimately drive surface photooxidation processes experience longer lifetimes due to reducing their recombination rate with electrons [6]. So the most effective way to improve the photocatalytic efficiency of doped semiconductor must be conducted directly on the surface areas.

At first, in electrospinning preparation of NFs, the final morphology and structure of NFs are controlled by many factors, such as volatile solvent, decomposition of the polymer, annealing heating rate, and annealing temperature. When we electrospin the precursor solution, rapid evaporation and following rapid solidification of volatile solvent will induce a rapid phase separation [7]. Phase boundaries may be crossed and structure formation by phase separation sets in. It means the solvent rich and poor regions will transform into different patterns, result in a rough surface of as-spun NFs. Furthermore, the next annealing will further modify the morphology and structure of NFs. Heating rate and annealing temperature were considered decisive factors in the formation of NFs [22, 23]. So we had designed the annealing process carefully. In the NFs annealing, rapid heating rate and/or high thermal anchoring will all lead to a spanning decomposition of polymer. This will make the final NFs have rougher surface and more defects. In this way, electrospinning is a perfect method to prepare NFs with modified surface. So BYT NFs will have more surface defects for photocatalysis. Secondly, the surface spreading of transition metal elements had been proved by both theories and experiments [19, 20]. When transition metal yttrium was doped into BT, the difference in the surface energies of impurities and host could provide a surface segregation energy, which could drive doping elements to the surface areas. This will further strengthen the narrowed band gap effect at surface areas of BYT NFs. Taking into account

the high specific surface area of NFs, the photocatalytic efficiency of doped semiconductor BYT NFs can be enhanced in this mechanism.

In sum, producing doped NFs by electrospinning is an excellent method to tailor the properties of materials not only due to the modified surface but also due to the doping effect. This work shows how it improved the photocatalytic properties of doped BT. Furthermore, it has a wide range of potential applications in areas based on complex compounds with specific surface and special doping effect, such as sensor, filter, or absorbed reactant. Much investigation on the properties and applications of doped NFs synthesized by electrospinning is highly desired.

4. Conclusions

Based on electrospinning, a direct and effective method to improve the photocatalysis of doped semiconductor was developed. BYT NFs were fabricated by electrospinning and subsequent annealing. BT NFs and BYT ceramics powders were also prepared as contrast. XRD patterns show that all samples have pure perovskite phase. BYT NFs with inhomogeneous diameter less than 200 nm have been proved by SEM images and EDX measurements. Significant photocatalytic effect of BYT NFs was characterized compared to weaker effect of BYT ceramics powders and little effect of BT NFs. Since specific surface and proper band gap energy were considered key factors in photocatalysis, the strong photodegradation of MB in the presence of BYT NFs was induced by the morphology and structure modification in electrospinning, the surface spreading of transition metal yttrium, and the narrowed band gap energy in yttrium doping. BYT ceramics powders and BT NFs have weaker photocatalytic efficiency for the unmodified surface and unfitted band gap energy. Producing doped NFs by electrospinning is an excellent method to tailor the properties. Much investigation on the properties and potential applications of doped NFs synthesized by electrospinning is highly desired.

Conflict of Interests

The authors declare that they have no conflict of interests regarding the publication of this paper.

Acknowledgments

This work was financially supported by National Natural Science Foundation of China (no. 11304069) and Natural Science Foundation of Hainan Province (no. 114009).

References

- [1] M. R. Hoffmann, S. T. Martin, W. Choi, and D. W. Bahnemann, "Environmental applications of semiconductor photocatalysis," *Chemical Reviews*, vol. 95, no. 1, pp. 69–96, 1995.
- [2] G. Palmisano, V. Augugliaro, M. Pagliaro, and L. Palmisano, "Photocatalysis: a promising route for 21st century organic chemistry," *Chemical Communications*, no. 33, pp. 3425–3437, 2007.
- [3] A. Mills and S. le Hunte, "An overview of semiconductor photocatalysis," *Journal of Photochemistry and Photobiology A: Chemistry*, vol. 108, no. 1, pp. 1–35, 1997.
- [4] S. Livraghi, A. Votta, M. C. Paganini, and E. Giamello, "The nature of paramagnetic species in nitrogen doped TiO₂ active in visible light photocatalysis," *Chemical Communications*, vol. 28, no. 4, pp. 498–500, 2005.
- [5] J. Zhang, W. K. Chen, J. H. Xi, and Z. G. Ji, "{001} Facets of anatase TiO₂ show high photocatalytic selectivity," *Materials Letters*, vol. 79, pp. 259–262, 2012.
- [6] T. L. Thompson and J. T. Yates Jr., "TiO₂-based photocatalysis: surface defects, oxygen and charge transfer," *Topics in Catalysis*, vol. 35, no. 3–4, pp. 197–210, 2005.
- [7] A. L. Linsebigler, G. Q. Lu, and J. T. Yates, "Photocatalysis on TiO₂ surfaces: principles, mechanisms, and selected results," *Chemical Reviews*, vol. 95, no. 3, pp. 735–758, 1995.
- [8] M. Bognitzki, W. Czado, T. Frese et al., "Nanostructured fibers via electrospinning," *Advanced Materials*, vol. 13, no. 1, pp. 70–72, 2001.
- [9] H. Niu and T. Lin, "Fiber generators in needleless electrospinning," *Journal of Nanomaterials*, vol. 2012, Article ID 725950, 13 pages, 2012.
- [10] Z. Liu, D. D. Sun, P. Guo, and J. O. Leckie, "An efficient bicomponent TiO₂/SnO₂ nanofiber photocatalyst fabricated by electrospinning with a side-by-side dual spinneret method," *Nano Letters*, vol. 7, no. 4, pp. 1081–1085, 2007.
- [11] D. Lin, H. Wu, R. Zhang, and W. Pan, "Enhanced photocatalysis of electrospun Ag-ZnO heterostructured nanofibers," *Chemistry of Materials*, vol. 21, no. 15, pp. 3479–3484, 2009.
- [12] J. Zhang, W. Fu, J. H. Xi et al., "N-doped rutile TiO₂ nano-rods show tunable photocatalytic selectivity," *Journal of Alloys and Compounds*, vol. 575, pp. 40–47, 2013.
- [13] W. J. Merz, "Switching time in ferroelectric BaTiO₃ and its dependence on crystal thickness," *Journal of Applied Physics*, vol. 27, no. 8, pp. 938–943, 1956.
- [14] T. Takenaka and H. Nagata, "Current status and prospects of lead-free piezoelectric ceramics," *Journal of the European Ceramic Society*, vol. 25, no. 12, pp. 2693–2700, 2005.
- [15] G. M. Madhu, M. A. L. A. Raj, K. V. K. Pai, and S. Rao, "Photodegradation of methylene blue dye using UV/BaTiO₃, UV/H₂O₂ and UV/H₂O₂/BaTiO₃ oxidation processes," *Indian Journal of Chemical Technology*, vol. 14, no. 2, pp. 139–144, 2007.
- [16] P. Ren, H. Fan, and X. Wang, "Electrospun nanofibers of ZnO/BaTiO₃ heterostructures with enhanced photocatalytic activity," *Catalysis Communications*, vol. 25, no. 8, pp. 32–35, 2012.
- [17] P. Blanchart, J. F. Baumard, and P. Abelard, "Effects of yttrium doping on the grain and grain-boundary resistivities of BaTiO₃ for positive temperature coefficient thermistors," *Journal of the American Ceramic Society*, vol. 75, no. 5, pp. 1068–1072, 1992.
- [18] J. Qi, L. Li, Y. Wang, Y. Fan, and Z. Gui, "Yttrium doping behavior in BaTiO₃ ceramics at different sintered temperature," *Materials Chemistry and Physics*, vol. 82, no. 2, pp. 423–427, 2003.
- [19] A. V. Ruban, H. L. Skriver, and J. K. Nørskov, "Surface segregation energies in transition-metal alloys," *Physical Review B*, vol. 59, no. 24, 10 pages, 1999.
- [20] P. Afanasiev, "On the metastability of 'monolayer coverage' in the MoO₃/ZrO₂ dispersions," *Materials Chemistry and Physics*, vol. 47, no. 2–3, pp. 231–238, 1997.
- [21] S. Ould-Chikh, O. Proux, P. Afanasiev et al., "Photocatalysis with chromium-doped TiO₂: bulk and surface doping," *ChemSusChem*, vol. 7, no. 5, pp. 1361–1371, 2014.

- [22] X. Chen, K. M. Unruh, C. Ni et al., "Fabrication, formation mechanism, and magnetic properties of metal oxide nanotubes via electrospinning and thermal treatment," *Journal of Physical Chemistry C*, vol. 115, no. 2, pp. 373–378, 2011.
- [23] Z. J. Shen, Y. Wang, W. P. Chen et al., "Electrospinning preparation and high-temperature superconductivity of $\text{YBa}_2\text{Cu}_3\text{O}_{7-x}$ nanotubes," *Journal of Materials Science*, vol. 48, no. 11, pp. 3985–3990, 2013.
- [24] J. Zhang, L. S. Qian, W. Fu, J. H. Xi, and Z. G. Ji, "Alkaline-earth metal Ca and N codoped TiO_2 with exposed {001} facets for enhancing visible light photocatalytic activity," *Journal of the American Ceramic Society*, vol. 97, no. 8, pp. 2615–2622, 2014.
- [25] S. Saha, T. P. Sinha, and A. Mookerjee, "Electronic structure, chemical bonding, and optical properties of paraelectric BaTiO_3 ," *Physical Review B: Condensed Matter and Materials Physics*, vol. 62, no. 13, pp. 8828–8834, 2000.
- [26] M.-Q. Cai, Z. Yin, and M.-S. Zhang, "First-principles study of optical properties of barium titanate," *Applied Physics Letters*, vol. 83, no. 14, pp. 2805–2807, 2003.

Research Article

Crystallization Behavior of Phosphate Glasses with Hydrophobic Coating Materials

Jaeyeop Chung and Bongki Ryu

Department of Materials Science and Engineering, Pusan National University, Busan 609-735, Republic of Korea

Correspondence should be addressed to Bongki Ryu; bkryu@pusan.ac.kr

Received 20 March 2015; Revised 8 May 2015; Accepted 18 May 2015

Academic Editor: Zijie Yan

Copyright © 2015 J. Chung and B. Ryu. This is an open access article distributed under the Creative Commons Attribution License, which permits unrestricted use, distribution, and reproduction in any medium, provided the original work is properly cited.

We analyzed the effect of the addition of Li_2O_3 , TiO_2 , and Fe_2O_3 on the crystallization behavior of P_2O_5 - CaO - SiO_2 - K_2O glasses and the effect of the crystallization behavior on the roughness and hydrophobicity of the coated surface. Exothermic behavior, including a strong exothermic peak in the 833–972 K temperature range when Fe_2O_3 , TiO_2 , or Li_2O_3 was added, was confirmed by differential thermal analysis. The modified glass samples (PFTL1–3) showed diffraction peaks when heated at 1073 and 1123 K for 5 min; the crystallized phase corresponds to $\text{Fe}_3(\text{PO}_4)_2$, that is, graptolite. We confirmed that the intensity of the diffraction peaks increases at high temperatures and with increasing Li_2O_3 content. In the case of the PFTL3 glass, a $\text{Li}_3\text{Fe}_2(\text{PO}_4)_2$ phase, that is, trillithium diiron(III) tris[phosphate(V)], was observed. Through scanning electron microscopy and the contact angles of the surfaces with water, we confirmed that the increase in surface roughness, correlated to the crystallization of the glass frit, increases hydrophobicity of the surface. The calculated values of the local activation energies for the growth of $\text{Fe}_3(\text{PO}_4)_2$ on the PFTL1, PFTL2, and PFTL3 glass were 237–292 kJ mol^{-1} , 182–258 kJ mol^{-1} , and 180–235 kJ mol^{-1} .

1. Introduction

Hydrophobic and superhydrophobic solid surfaces have attracted considerable attention in scientific and industrial fields owing to their unique self-cleaning, antifogging, anti-sticking, and anticontamination properties [1–5]. It has been theoretically and experimentally confirmed that superhydrophobic surfaces can be obtained by the cooperative effects of topographically roughened surface structures [6]. In accordance with this concept, researchers have prepared artificial superhydrophobic surfaces through hierarchical micro/nanostructures on specimen surfaces [6, 7] and have chemically modified these structures to reduce the surface energy [8]. Various methods have been reported for creating superhydrophobic surfaces, such as sol-gel processing [9], plasma processing [10], and spray pyrolysis [11]. However, these methods present limitations for industrial applications and are unsuitable for commercial products because they either are only applicable to small substrates or require time-consuming processing steps or expensive machinery [12]. Recently, studies have been performed to overcome

these problems. In particular, Reinoso et al. confirmed the influence of surface modification by crystallization on the hydrophobicity of surfaces, which occurs during the inorganic coating of glass frit by Fe_2O_3 and Cu microparticles [12]. They confirmed that the surface was modified and the hydrophobicity increased through the crystallization of the inorganic coating material. However, they only analyzed the crystallization generated by the addition of Fe_2O_3 and Cu microparticles, neglecting crystallization by the composition of the glass frit itself. If hydrophobicity can be expressed just by the crystallization of glass frit, this can be used in various applications such as self-cleaning household ovens [13, 14] and outdoor glass insulators [15].

Phosphate glass exhibits attractive properties such as low glass transition and melting temperatures, high thermal expansion coefficients, biocompatibility, and high refractive indices. These specifications are suitable for many applications in photonics, fast ion conductors [16–19], glass-to-metal seals [20–22], low-temperature enamels [22], NH_3 gas adsorption [23], and biomedical engineering [24]. An important characteristic of phosphate glass is its advantageous

TABLE 1: The chemical compositions of the PFTL glass samples.

Glass name	P ₂ O ₅ (wt%)	CaO (wt%)	SiO ₂ (wt%)	K ₂ O (wt%)	TiO ₂ (wt%)	Fe ₂ O ₃ (wt%)	Li ₂ O (wt%)
PFTL0 (reference)	74	14	5	7	0	0	0
PFTL1	65.1	12.3	4.4	6.2	5	5	2
PFTL2	64.4	12.2	4.3	6.1	5	5	3
PFTL3	63.7	12.0	4.3	6.0	5	5	4

crystallization behavior as compared to silicate glass [25, 26]. To further accelerate the crystallization of phosphate glass, nucleation agents such as Fe₂O₃ [27], Li₂O₃, and TiO₂ [28] are required; when the frit is coated with one of these agents, the glass can be crystallized using a short firing time [27].

In the present work, we investigated the effect of the addition of Li₂O₃, TiO₂, and Fe₂O₃ on the crystallization behavior of a P₂O₅-CaO-SiO₂-K₂O glass system widely used in various fields [29, 30]. In addition, we confirmed the effect of the crystallization of the glass frit on the roughness and hydrophobicity of the final coated surface.

2. Materials and Methods

2.1. Glass Preparation. Glass samples with this composition $(100-x-y)(0.74P_2O_5-0.14CaO-0.05SiO_2-0.07K_2O)-x(Fe_2O_3-TiO_2)-y(Li_2O_3)$ were used. The glass samples were prepared using NH₄H₂PO₄, CaCO₃, SiO₂, K₂CO₃, Fe₂O₃, TiO₂, and Li₂CO₃, all of which had purities higher than 99.9%. This mixture was melted in an Al₂O₃ crucible in an electrically heated furnace under ordinary atmospheric conditions at a temperature of 850°C for approximately 30 min to evaporate ammonia, carbonate, and water and to minimize the tendency for subsequent phosphate volatilization. The temperature was then gradually increased to 1250°C and maintained for 30 min to homogenize the melt. The melt was quenched by pouring it onto a plate. X-ray diffraction (XRD) analysis using an Ultima IV system (Rigaku) was employed to confirm the amorphous state of the synthesized glasses and the results are shown in Figure 1 and Table 1.

2.2. Measurements and Analysis. The glass frits were coated by the following procedure. The glass was ground and screened with a 44 μm mesh and then sprayed onto the surface of a low-carbon steel substrate (SPP steel), producing coatings with thicknesses of 200–220 μm. The coatings were fast-fired in an air atmosphere using an electrically heated furnace. The coating thickness of each sample is shown in Figure 2. The heating temperatures of 1073 K and 1123 K were applied for 5 min, which is a typical enamel sintering cycle. The phase analysis and crystallization of the heated samples were examined by XRD (Rigaku-Ultima IV). To determine the surfaces' hydrophilicity or hydrophobicity, a contact angle measurement system (Krüss DSA 100 Easy Drop) was used to find the contact angle of water with the coated surfaces. The roughness and nano- and microstructures were studied by field emission scanning electron microscopy (FE-SEM, Supra 25, Carl Zeiss).

Crystallization analysis was performed by a nonisothermal method that is easier and faster than the isothermal

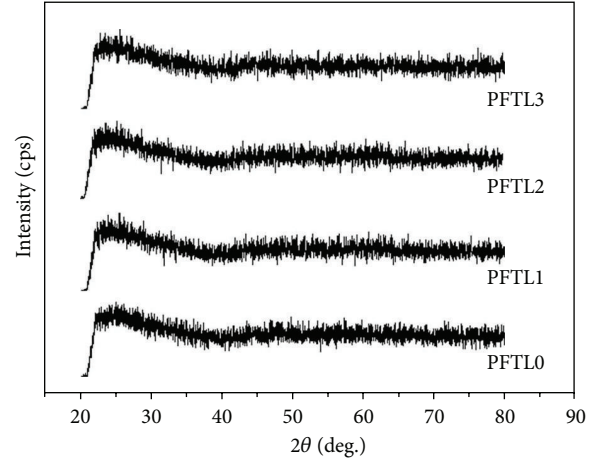


FIGURE 1: XRD data of PFTL glasses.

method [31, 32]. In order to determine the activation energy for crystallization of the samples, differential thermal analysis (DTA) measurements were performed using approximately 30 mg of the heat-treated glass powders in an air atmosphere at heating rates of 5, 10, 15, and 20 K/min up to 1273 K. The DTA results were further analyzed to obtain the activation energy values for the crystallization of each sample using the Ozawa [33] method. The slope of each graph was determined by the method of least squares.

3. Results and Discussion

3.1. Crystallization Behavior and Phase Analysis. The DTA curves for the glass powders obtained at different heating rates are presented in Figure 3. The DTA curves show the exothermic effect of heating, followed by a strong exothermic peak in the 833–972 K temperature range when Fe₂O₃, TiO₂, or Li₂O₃ is added. Furthermore, the DTA curves of the PFTL3 glass show an initial exothermic effect followed by a strong exothermic peak; Figure 3(c) also shows partial overlapping of the two peaks. The characteristic temperatures of the glass (T_g , T_c , and T_p) increased with increasing heating rate, as shown in Table 2. From Table 2, it is confirmed that T_g decreases with the addition of Fe₂O₃ or TiO₂. This means that Fe₂O₃ and TiO₂ act as network modifiers in phosphate glass and that they weaken the glass structure. In addition, the DTA data reveal that the addition of Li₂O₃ shifts the endothermic peaks to lower temperatures; that is, a lower temperature is needed to initiate crystallization [34].

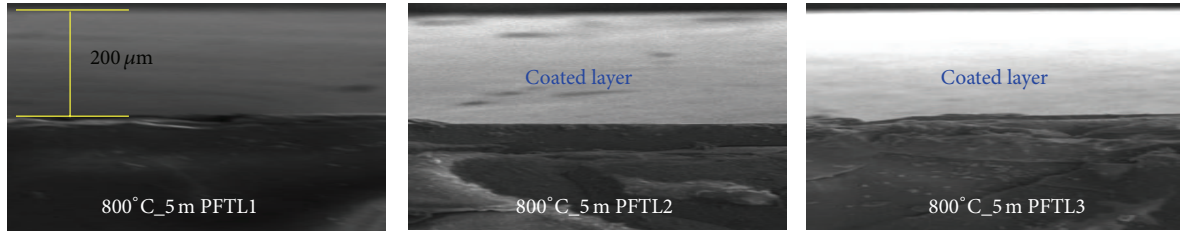


FIGURE 2: The coating thicknesses of PFTL glasses.

TABLE 2: Glass transition temperature (T_g) and maximum crystallization temperatures (T_{p1} and T_{p2}) determined from DTA data obtained at different heating rates.

Heating rate, α	PFTL0	PFTL1		PFTL2		PFTL3		
	T_g (K)	T_g (K)	T_{p1} (K)	T_g (K)	T_{p1} (K)	T_g (K)	T_{p1} (K)	T_{p2} (K)
5	878	833	943	819	927	810	902	921
10	883	839	962	830	945	822	920	948
15	891	847	975	839	958	835	931	966
20	903	861	984	853	968	847	939	972

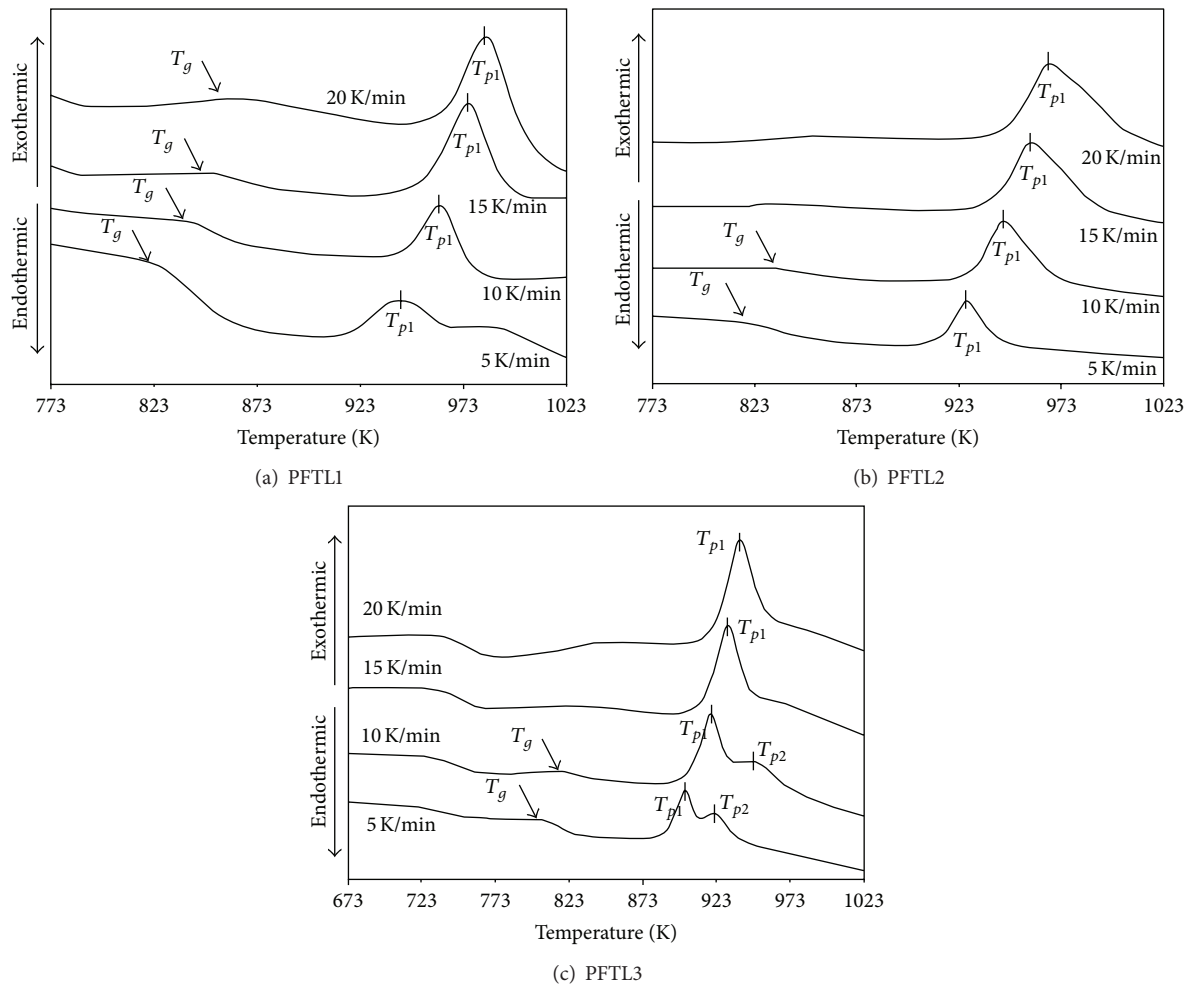


FIGURE 3: DTA curves of PFTL glasses obtained at different heating rates.

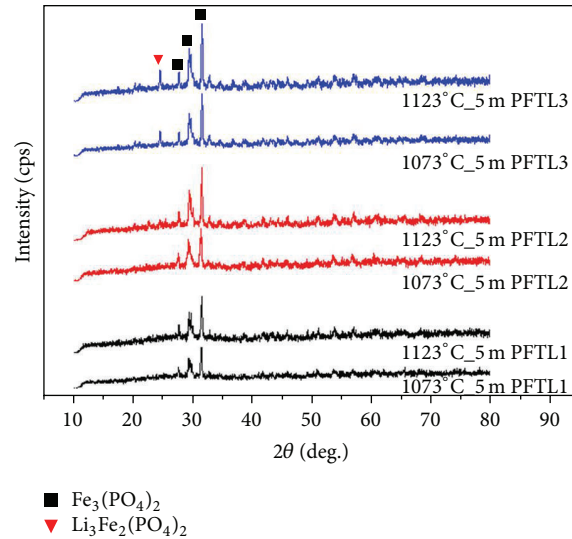


FIGURE 4: XRD data for glass samples heat-treated at different temperatures.

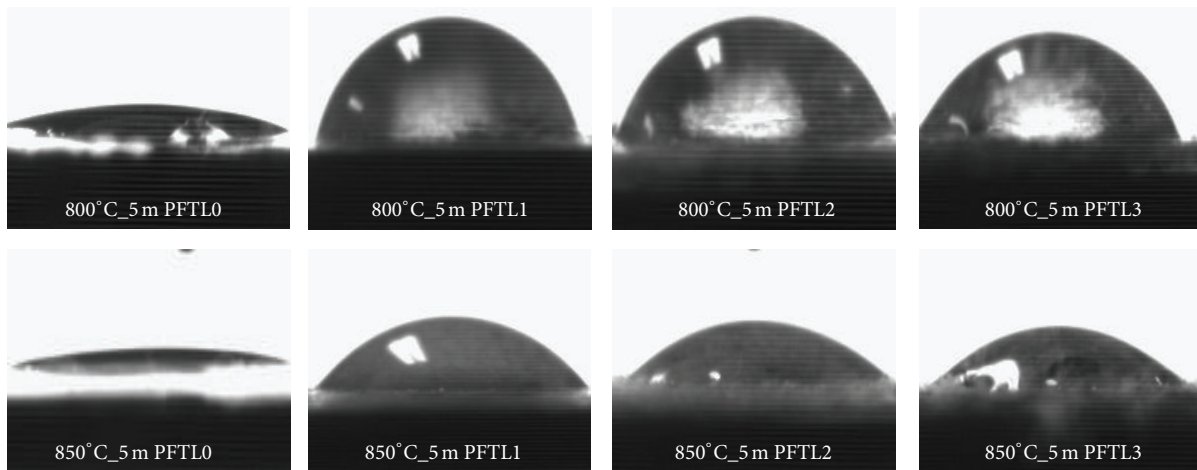


FIGURE 5: Hydrophobicity of PFTL glasses heat-treated at different temperatures, displayed by contact angle of water droplet.

To confirm the nucleation results of the DTA curves, XRD analysis was performed. Figure 4 presents the XRD patterns for glass samples heated for 5 min at both 1073 K and 1123 K. The PFTL1–3 glass samples all show diffraction peaks; the crystalline phase corresponds to the compound $\text{Fe}_3(\text{PO}_4)_2$, that is, graftonite. The data confirms that the intensity of the diffraction peaks increases at higher heating temperatures and with increased Li_2O_3 content. In addition, in the case of the PFTL3 glass, a $\text{Li}_3\text{Fe}_2(\text{PO}_4)_2$ phase is observed. This indicates that further crystallization occurs at higher temperature and with increased Li_2O_3 content. Through XRD analysis, we confirmed that the two exothermic peaks in the DTA curves are the result of crystal phases of $\text{Fe}_3(\text{PO}_4)_2$ (peak 1 of PFTL1, PFTL2, and PFTL3) and $\text{Li}_3\text{Fe}_2(\text{PO}_4)_2$ (peak 2 of PFTL3).

3.2. Hydrophobicity and Surface Characteristics. The contact angle of a water drop was measured for the glass samples of

different compositions and coating conditions; the results are shown in Figures 5 and 6.

As seen in the figures, the noncrystalline PFTL0 glass, that is, a typical phosphate glass, has very strong hydrophilicity; this is expected from the chemical composition of phosphate glass. The phosphate group is negatively charged, making the head polar. The phosphate heads are thus attracted to the water molecules in their environment. For these reasons, phosphate glasses have strong hydrophilicity [35]. As the glass crystallized, the contact angle increased up to a maximum of approximately 87° , obtained with PFTL1. In addition, the PFTL2 and PFTL3 glasses, which were more thoroughly crystallized, had lower hydrophobicity than the PFTL1 glass; all glass samples heated at 850°C had lower contact angles than the glass samples heated at 800°C . These results were analyzed through surface characteristics.

For solids, the term “surface energy” reflects the affinity of the surface to other materials; the higher the surface energy

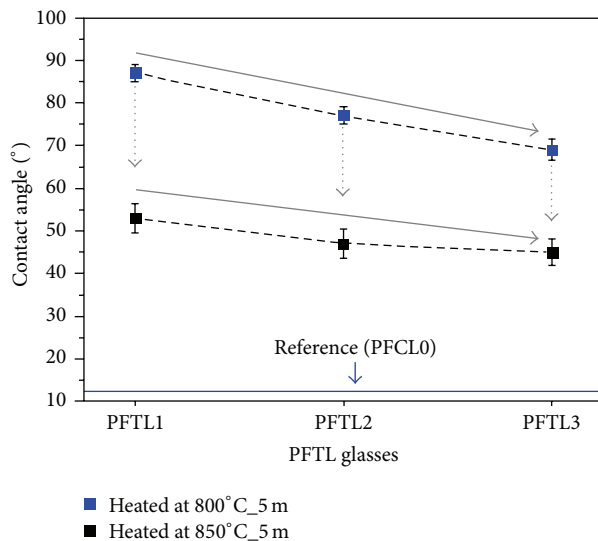


FIGURE 6: The contact angles of the PFTL glasses.

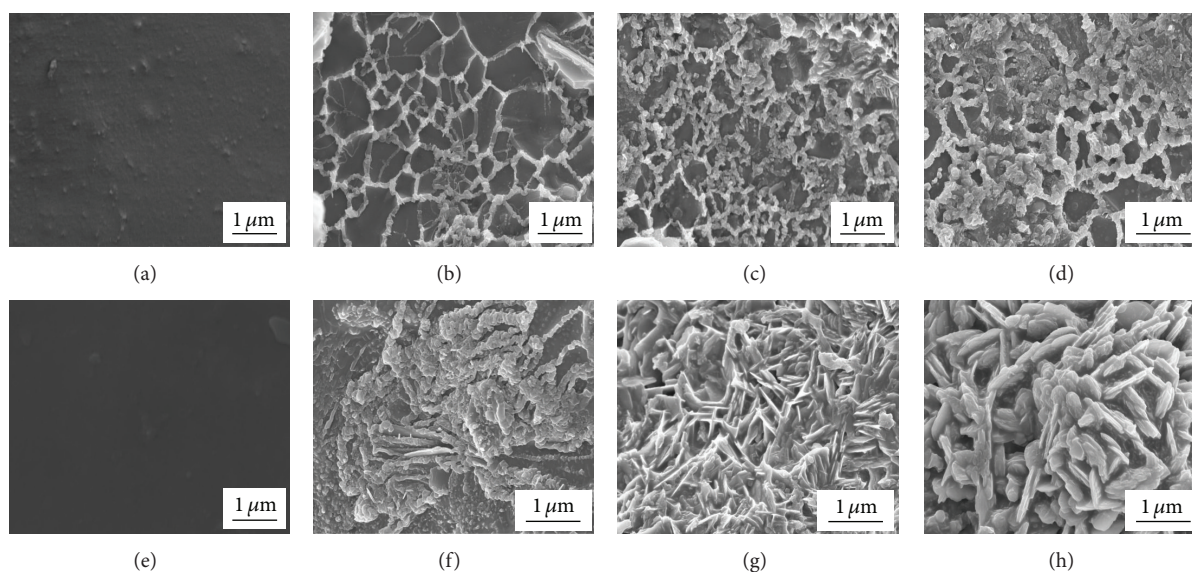


FIGURE 7: SEM images of PFTL glasses heated under different conditions: (a) PFTL0, (b) PFTL1, (c) PFTL2, and (d) PFTL3 glasses heated at 800°C for 5 min and (e) PFTL0, (f) PFTL1, (g) PFTL2, and (h) PFTL3 glasses heated at 850°C for 5 min.

of the solid, the more the energy gained upon bringing this surface into contact with other materials. Therefore, the surface energy describes the adhesive properties of the material, which can be “activated” by different surface treatments or by changing the material chemistry.

According to Abou Neel et al., the total surface free energy of phosphate glass is very high, more than 75 mN m^{-1} [36, 37]. This is because of the polar characteristics of phosphate glasses, as mentioned above.

When Fe_2O_3 or TiO_2 is added to the phosphate glass, the surface energy of the glass is reduced [36, 37]. The reason for this is associated with the formation of hydration-resistant Ti–O–P and Fe–O–P bonding in place of

hydration-susceptible P–O–P bonding. The hydrophobicity of the coated glass surfaces was further analyzed by surface morphology.

SEM micrographs of the PFTL glass samples heated at 800 and 850°C for 5 min are shown in Figure 7. We can determine the causes of changes of hydrophobicity of the PFTL glasses from these micrographs. The typical phosphate sample, PFTL0, shows a flat surface very similar to those usually found on commercial enamels. PFTL1–3 heated at 800°C for 5 min have pseudocellular structures (hereafter, cellular regions) resembling those found on the surface of hydrophobic leaves [12, 38]. Thus, hydrophobicity increases when the glass crystallizes. We think that PFTL2 and PFTL3

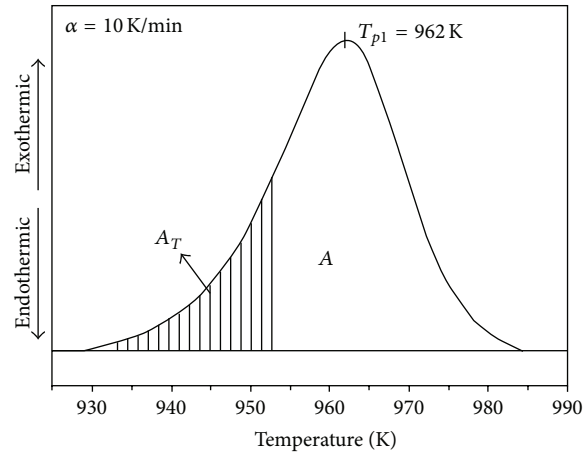


FIGURE 8: Area A between T_i and T_f and area A_T between T_i and T for the crystallization peak of the PFTL1 glass ($\alpha = 10$ K/min).

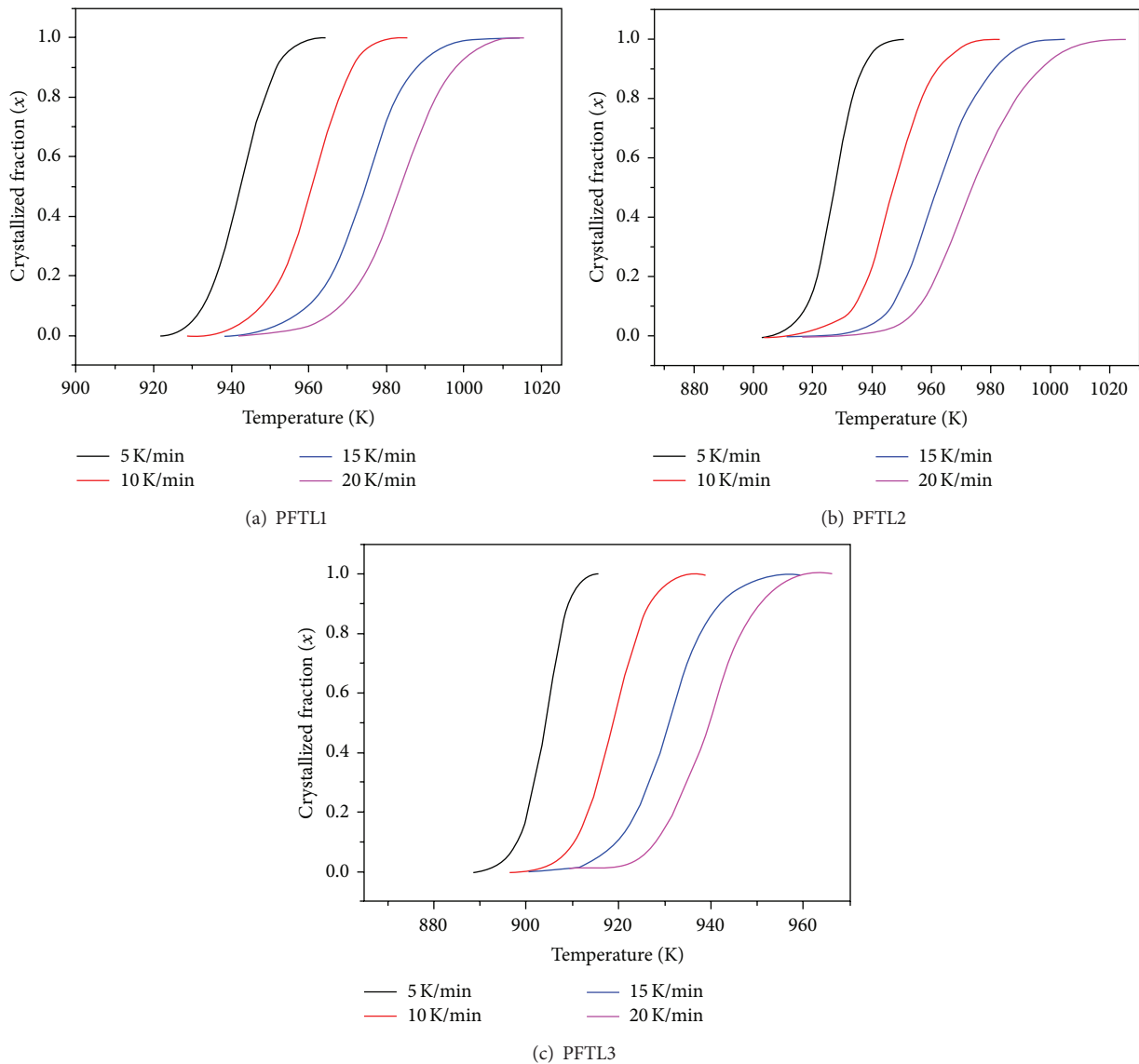


FIGURE 9: Crystallized fraction as a function of temperature at different heating rates.

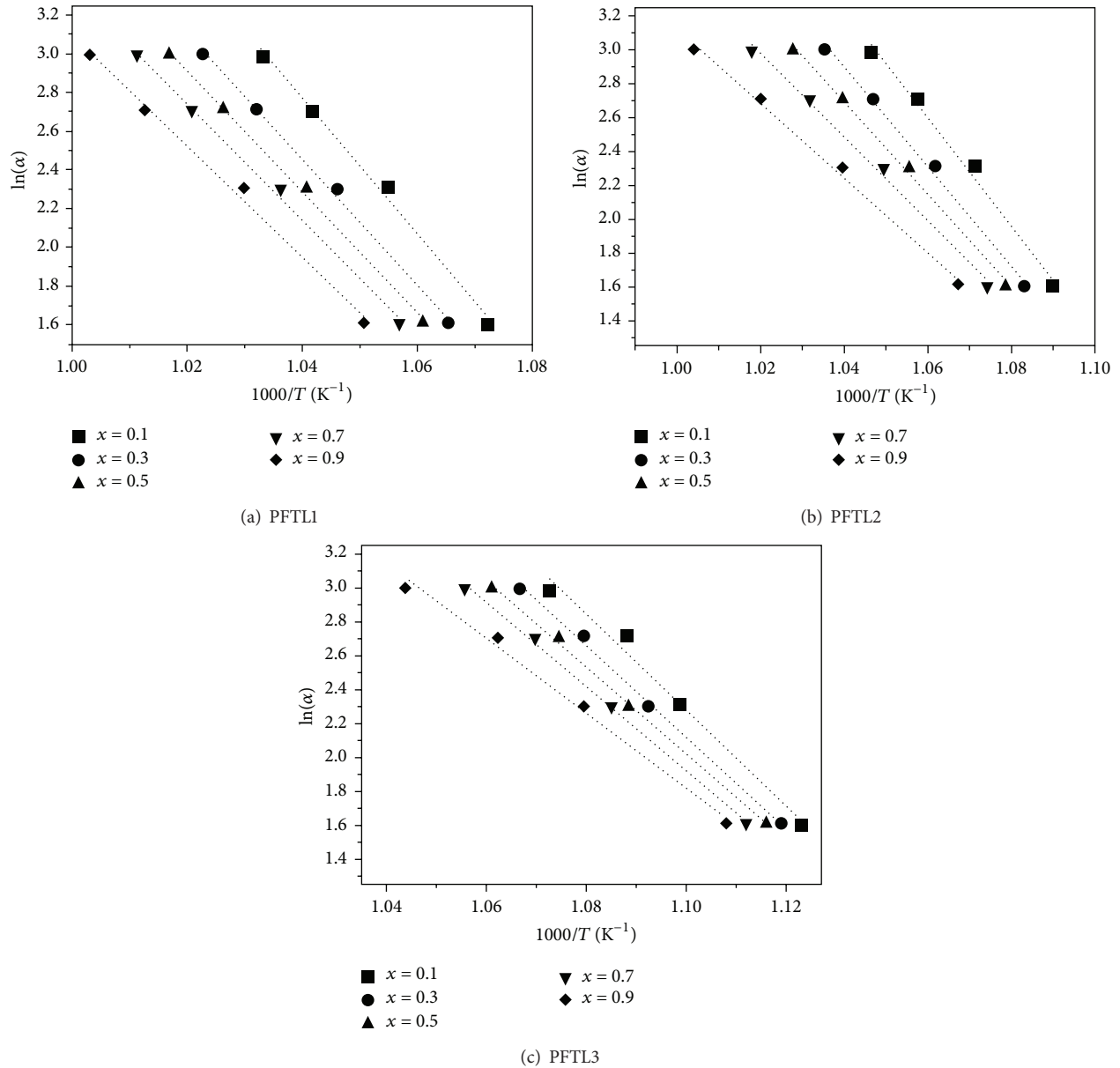


FIGURE 10: Plots of $\ln(\alpha)$ versus $1000/T$ for various values of x ($0.1 < x < 0.9$) for the $\text{Fe}_3(\text{PO}_4)_2$ crystallization peaks.

exhibited lower hydrophobicity than PFTL1 owing to the increase in the size of the nanostructures and the corresponding reduced fraction of intergranular surface voids under the water drop. As previously demonstrated, a higher fraction of empty space below the water drop increases the contact angle, making the surface more hydrophobic [39]. In addition, PFTL1-3 heated at 850°C for 5 min presented rough surfaces completely covered in crystalline phases owing to the high crystallization of these glasses. It is thought that these rough surfaces induced low hydrophobicity. We confirmed that the increase in surface roughness occurring by the crystallization of the glass frit increased the hydrophobicity of the surface through the analysis of hydrophobicity and surface characterization. However, the contact angle with water never exceeded 90° , which is the general standard for

hydrophobic materials. This is thought to be because of the strong hydrophilic nature of phosphate glasses, as previously described.

3.3. Crystallization Kinetics. We analyzed the activation energy for the crystallization of the glass samples in order to verify the impact of surface crystalline phase on the hydrophobicity. The activation energy was calculated only for the $\text{Fe}_3(\text{PO}_4)_2$ phase of the PFTL1, PFTL2, and PFTL3 glasses.

The Johnson-Mehl-Avrami (JMA) model, which is the most general method of calculating activation energies, implies that the activation energy, E_c , should be constant during the transformation process [40]. However, some authors have shown that E_c values are not necessarily constant; instead, they vary during the transformation in

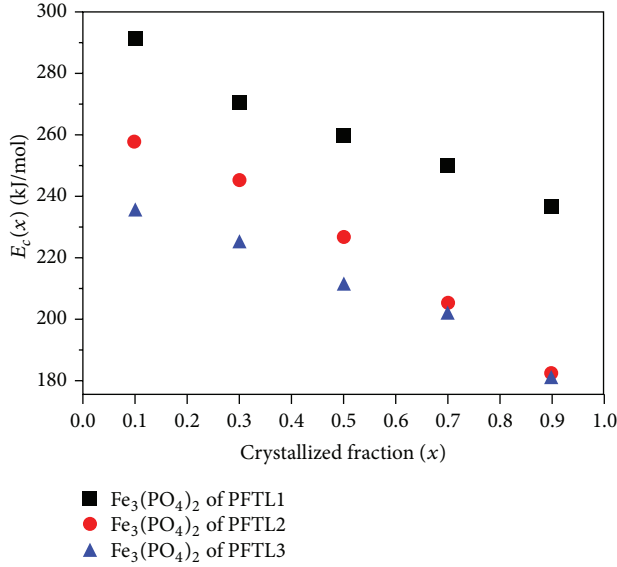


FIGURE 11: Local activation energy for crystallization $E_c(x)$ as a function of crystallized fraction (x), obtained from the DTA curve at 10 K/min.

nonisothermal methods [41]. The activation energy for different crystallization volume fractions is not constant during the whole transformation owing to changes in the nucleation and growth behaviors during crystallization [41]. The variation of E_c can be expressed by the local activation energy $E_c(x)$. The value of $E_c(x)$ can be determined from nonisothermal DTA results using the method proposed by Ozawa according to the following relationship [41]:

$$\left[\frac{d(\ln \alpha)}{d(1/T)} \right]_x = -\frac{E_c(x)}{R}, \quad (1)$$

where R is the gas constant and T and α are the temperature and the heating rate, respectively, corresponding to the value of the crystallized fraction, x .

The value of x at a specific temperature can be determined from the DTA curves [42] by the ratio A_T/A . Here, A is the total area of the crystallization peak between temperature T_i (where crystallization begins) and temperature T_f (where the crystallization is completed) and A_T is the area between T_i and T , as shown schematically in Figure 8. The graphical representation of x as a function of T shows typical sigmoid curves for different heating rates, as presented in Figure 9, indicating that the formation of the crystalline phase proceeds by a combination of nucleation and growth processes.

Using the experimental data presented in Figure 9, the plot of $\ln(\alpha)$ versus $1/T$ for various values of x ($0.1 < x < 0.9$) was obtained, and the results are shown in Figure 10. The value of $E_c(x)$ was calculated from the slope.

Figure 11 shows the variation of $E_c(x)$ versus x for the studied glass. It is observed that for the exothermal peak of all samples, corresponding to $\text{Fe}_3(\text{PO}_4)_2$, $E_c(x)$ is high during the initiation of the crystallization process and then it decreases. In addition, it is confirmed that the activation energies of PFTL2 and PFTL3 are lower than that of PFTL1.

This means that the crystal phases of PFTL2 and PFTL3 are more easily formed than that of PFTL1, and these results support the SEM and hydrophobicity results given above. By calculating the activation energy for crystallization, we think that PFTL2 and PFTL3 had lower hydrophobicity than PFTL1 owing to the increase in the size of their surface crystal phase structures and the corresponding reduced fraction of intergranular surface voids because of their lower activation energies.

4. Conclusions

This study analyzed the effect of the addition of Li_2O_3 , TiO_2 , and Fe_2O_3 on the crystallization behavior of a P_2O_5 - CaO - SiO_2 - K_2O glass system and the effect of the crystallization of glass frit on the roughness and hydrophobicity of the coated glass surface.

We confirmed through XRD and DTA results that crystallization of P_2O_5 - CaO - SiO_2 - K_2O glass occurs with the addition of Li_2O_3 , TiO_2 , or Fe_2O_3 . In addition, through DTA analysis, it was confirmed that T_g decreases with the addition of Fe_2O_3 or TiO_2 , which indicates that Fe_2O_3 and TiO_2 act as network modifiers in phosphate glasses and weaken the glass structure. The surfaces of PFTL1-3 heated at 800°C for 5 min presented a cell-like microstructure in which we observed nanostructures owing to the crystallization of graffonite and trilitium diiron(III) tris[phosphate(V)]. This hierarchical structure is similar to those found on the surfaces of some hydrophobic leaves. For these two reasons (adding Fe_2O_3 and TiO_2 , which act as network modifiers, and broken P-O-P bonding, which increases the surface morphology), the hydrophobicity increases in accordance with the degree of crystallization of the Li_2O_3 -, TiO_2 -, and Fe_2O_3 -doped P_2O_5 - CaO - SiO_2 - K_2O glasses. However, the contact angle of the surfaces of these glasses with water never exceeded 90° , which is the general standard of hydrophobicity. We think this is owing to the particular characteristics of the phosphate groups, which are strongly hydrophilic. Through this study, we confirmed the possibility of developing inorganic and hydrophobic coating materials using the crystallization of glass. In addition, we established the need for additional research to overcome the compositional limitations of phosphate glasses to express hydrophobicity with existing hydrophobic coating materials.

Conflict of Interests

The authors declare that there is no conflict of interests regarding the publication of this paper.

Acknowledgments

This research was financially supported by the Ministry of Education, Science and Technology (MEST) and National Research Foundation of Korea (NRF) through the Human Resource Training Project for Regional Innovation.

References

- [1] E. Celia, T. Darmanin, E. Taffin de Givenchy, S. Amigoni, and F. Guittard, "Recent advances in designing superhydrophobic surfaces," *Journal of Colloid and Interface Science*, vol. 402, pp. 1–18, 2013.
- [2] V. A. Ganesh, H. K. Raut, A. S. Nair, and S. Ramakrishna, "A review on self-cleaning coatings," *Journal of Materials Chemistry*, vol. 21, no. 41, pp. 16304–16322, 2011.
- [3] Y. Y. Yan, N. Gao, and W. Barthlott, "Mimicking natural superhydrophobic surfaces and grasping the wetting process: a review on recent progress in preparing superhydrophobic surfaces," *Advances in Colloid and Interface Science*, vol. 169, no. 2, pp. 80–105, 2011.
- [4] Z. G. Guo, W. M. Liu, and B.-L. Su, "Superhydrophobic surfaces: from natural to biomimetic to functional," *Journal of Colloid and Interface Science*, vol. 353, no. 2, pp. 335–355, 2011.
- [5] Y. Zhou, M. Li, X. Zhong, Z. Zhu, P. Deng, and H. Liu, "Hydrophobic composite coatings with photocatalytic self-cleaning properties by micro/nanoparticles mixed with fluorocarbon resin," *Ceramics International*, vol. 41, no. 4, pp. 5341–5347, 2015.
- [6] J. Zhao, Z. Li, M. Zhang, and A. Meng, "Super-hydrophobic surfaces of SiO₂-coated SiC nanowires: fabrication, mechanism and ultraviolet-durable super-hydrophobicity," *Journal of Colloid and Interface Science*, vol. 444, pp. 33–37, 2015.
- [7] H. C. Barshilia, N. Selvakumar, N. Pillai, L. M. Devi, and K. S. Rajam, "Wettability of ZnO: a comparison of reactively sputtered; Thermally oxidized and vacuum annealed coatings," *Applied Surface Science*, vol. 257, no. 9, pp. 4410–4417, 2011.
- [8] J. Seo, S. Lee, J. Lee, and T. Lee, "Guided transport of water droplets on superhydrophobic-hydrophilic patterned Si nanowires," *ACS Applied Materials & Interfaces*, vol. 3, no. 12, pp. 4722–4729, 2011.
- [9] R. Taurino, E. Fabbri, M. Messori, F. Pilati, D. Pospiech, and A. Synytska, "Facile preparation of superhydrophobic coatings by sol-gel processes," *Journal of Colloid and Interface Science*, vol. 325, no. 1, pp. 149–156, 2008.
- [10] B. Balu, V. Breedveld, and D. W. Hess, "Fabrication of 'roll-off' and 'sticky' superhydrophobic cellulose surfaces-via plasma processing," *Langmuir*, vol. 24, no. 9, pp. 4785–4790, 2008.
- [11] N. L. Tarwal and P. S. Patil, "Superhydrophobic and transparent ZnO thin films synthesized by spray pyrolysis technique," *Applied Surface Science*, vol. 256, no. 24, pp. 7451–7456, 2010.
- [12] J. J. Reinoso, J. J. Romero, M. A. de la Rubia, A. del Campo, and J. F. Fernández, "Inorganic hydrophobic coatings: surfaces mimicking the nature," *Ceramics International*, vol. 39, no. 3, pp. 2489–2495, 2013.
- [13] P. Palmisano, P. Faraldi, D. Fino, and N. Russo, "Household oven self-cleaning surfaces via catalytic thermal oxidation," *Chemical Engineering Journal*, vol. 154, no. 1–3, pp. 251–257, 2009.
- [14] P. Palmisano, S. P. Hernandez, M. Hussain, D. Fino, and N. Russo, "A new concept for a self-cleaning household oven," *Chemical Engineering Journal*, vol. 176–177, pp. 253–259, 2011.
- [15] V. Dave, H. O. Gupta, and R. Chandra, "Nanostructured hydrophobic DC sputtered inorganic oxide coating for outdoor glass insulators," *Applied Surface Science*, vol. 295, pp. 231–239, 2014.
- [16] H. Hosono and Y. Abe, "Fast lithium conducting glass-ceramics in the Li₂O–CaO–TiO₂–Al₂O₃–P₂O₅ system," *Solid State Ionics*, vol. 44, no. 3–4, pp. 293–297, 1991.
- [17] H. Hosono and Y. Abe, "Porous glass-ceramics with a skeleton of the fast-lithium-conducting crystal Li_{1+x}Ti_{2-x}Al_x(PO₄)₃," *Journal of the American Ceramic Society*, vol. 75, no. 10, pp. 2862–2864, 1992.
- [18] B. K. Money and K. Hariharan, "Lithium ion conduction in lithium metaphosphate based systems," *Applied Physics A*, vol. 88, no. 4, pp. 647–652, 2007.
- [19] X. Xu, Z. Wen, X. Yang, J. Zhang, and Z. Gu, "High lithium ion conductivity glass-ceramics in Li₂O–Al₂O₃–TiO₂–P₂O₅ from nanoscaled glassy powders by mechanical milling," *Solid State Ionics*, vol. 177, no. 26–32, pp. 2611–2615, 2006.
- [20] R. C. Lucacel, M. Maier, and V. Simon, "Structural and in vitro characterization of TiO₂–CaO–P₂O₅ bioglasses," *Journal of Non-Crystalline Solids*, vol. 356, no. 50–51, pp. 2869–2874, 2010.
- [21] N. A. Ghoneim, A. M. Abdelghany, S. M. Abo-Naf, F. A. Moustafa, and K. M. Elbadry, "Spectroscopic studies of lithium phosphate, lead phosphate and zinc phosphate glasses containing TiO₂: effect of gamma irradiation," *Journal of Molecular Structure*, vol. 1035, pp. 209–217, 2013.
- [22] H. A. Elbatal, A. M. Abdelghany, F. H. Elbatal, K. M. Elbadry, and F. A. Moustafa, "UV-visible and infrared absorption spectra of gamma irradiated CuO-doped lithium phosphate, lead phosphate and zinc phosphate glasses: a comparative study," *Physica B: Condensed Matter*, vol. 406, no. 19, pp. 3694–3703, 2011.
- [23] Y. Daiko, H. Yajima, and T. Kasuga, "Preparation of porous titanium phosphate glass-ceramics for NH₃ gas adsorption with self-cleaning ability," *Journal of the European Ceramic Society*, vol. 28, no. 1, pp. 267–270, 2008.
- [24] S. V. Dorozhkin, "Amorphous calcium (ortho)phosphates," *Acta Biomaterialia*, vol. 6, no. 12, pp. 4457–4475, 2010.
- [25] S. A. M. Abdel-Hameed, M. A. Marzouk, and M. M. Farag, "Effect of P₂O₅ and MnO₂ on crystallization of magnetic glass ceramics," *Journal of Advanced Research*, vol. 5, no. 5, pp. 543–555, 2014.
- [26] A. Ananthanarayanan, G. P. Kothiyal, L. Montagne, and B. Revel, "MAS-NMR investigations of the crystallization behaviour of lithium aluminum silicate (LAS) glasses containing P₂O₅ and TiO₂ nucleants," *Journal of Solid State Chemistry*, vol. 183, no. 6, pp. 1416–1422, 2010.
- [27] E. Mohaghegh, A. Nemati, B. Eftekhari Yekta, S. Banijamali, and F. Rezaei, "Influence of Fe₂O₃ on non-isothermal crystallization kinetics and microstructure of lithium titanium phosphate glass-ceramics," *Journal of Non-Crystalline Solids*, vol. 408, pp. 130–136, 2015.
- [28] H. Liu, Y. Wang, T. Wang, R. Yang, and S. Liu, "Enhanced surface crystallization of glass by adding traditional oxide nucleating agents," *Ceramics International*, vol. 40, no. 1, pp. 453–457, 2014.
- [29] H. R. Ahmadi Mooghari, A. Nemati, B. Eftekhari Yekta, and Z. Hamnabard, "The effect of SiO₂ and K₂O on glass forming ability and structure of CaO–TiO₂–P₂O₅ glass system," *Ceramics International*, vol. 38, no. 4, pp. 3281–3290, 2012.
- [30] J. Sułowska, I. Waclawska, and Z. Olejniczak, "Structural studies of copper-containing multicomponent glasses from the SiO₂–P₂O₅–K₂O–CaO–MgO system," *Vibrational Spectroscopy*, vol. 65, pp. 44–49, 2013.
- [31] A. A. S. Lopes, R. C. C. Monteiro, R. S. Soares, M. M. R. A. Lima, and M. H. V. Fernandes, "Crystallization kinetics of a barium-zinc borosilicate glass by a non-isothermal method," *Journal of Alloys and Compounds*, vol. 591, pp. 268–274, 2014.

- [32] M. Erol, S. Kuchukbayrak, and A. Ersoy-Meriçboyu, "The application of differential thermal analysis to the study of isothermal and non-isothermal crystallization kinetics of coal fly ash based glasses," *Journal of Non-Crystalline Solids*, vol. 355, no. 9, pp. 569–576, 2009.
- [33] T. Ozawa, "Calculating the phase transformation kinetics using impedance spectroscopy for Sb_2Te_3 ," *Polymer*, vol. 12, pp. 150–158, 1971.
- [34] S. M. Salman, S. N. Salama, and H. A. Abo-Mosallam, "The effect of aluminum and germanium oxides on the crystallization process and magnetic properties of $\text{Li}_2\text{O}-\text{Fe}_2\text{O}_3-\text{SiO}_2$ glass system," *Ceramics International*, vol. 41, no. 1, pp. 1521–1529, 2015.
- [35] M. Navarro, E. Engel, J. A. Planell, I. Amaral, M. Barbosa, and M. P. Ginebra, "Surface characterization and cell response of a PLA/CaP glass biodegradable composite material," *Journal of Biomedical Materials Research, Part A*, vol. 85, no. 2, pp. 477–486, 2008.
- [36] E. A. Abou Neel, I. Ahmed, J. J. Blaker et al., "Effect of iron on the surface, degradation and ion release properties of phosphate-based glass fibres," *Acta Biomaterialia*, vol. 1, no. 5, pp. 553–563, 2005.
- [37] E. A. Abou Neel, W. Chrzanowski, and J. C. Knowles, "Effect of increasing titanium dioxide content on bulk and surface properties of phosphate-based glasses," *Acta Biomaterialia*, vol. 4, no. 3, pp. 523–534, 2008.
- [38] Z. Burton and B. Bhushan, "Surface characterization and adhesion and friction properties of hydrophobic leaf surfaces," *Ultramicroscopy*, vol. 106, no. 8-9, pp. 709–719, 2006.
- [39] A. B. D. Cassie and S. Baxter, "Wettability of porous surfaces," *Transactions of the Faraday Society*, vol. 40, pp. 546–551, 1944.
- [40] A. A. Abu-Sehly, S. N. Alamri, and A. A. Joraid, "Measurements of DSC isothermal crystallization kinetics in amorphous selenium bulk samples," *Journal of Alloys and Compounds*, vol. 476, no. 1-2, pp. 348–351, 2009.
- [41] A. A. Joraid, S. N. Alamri, and A. A. Abu-Sehly, "Model-free method for analysis of non-isothermal kinetics of a bulk sample of selenium," *Journal of Non-Crystalline Solids*, vol. 354, no. 28, pp. 3380–3387, 2008.
- [42] A. Arora, E. R. Shaaban, K. Singh, and O. P. Pandey, "Non-isothermal crystallization kinetics of $\text{ZnO}-\text{BaO}-\text{B}_2\text{O}_3-\text{SiO}_2$ glass," *Journal of Non-Crystalline Solids*, vol. 354, no. 33, pp. 3944–3951, 2008.

Research Article

Laser-Doping through Anodic Aluminium Oxide Layers for Silicon Solar Cells

Pei Hsuan Doris Lu, Alison Lennon, and Stuart Wenham

School of Photovoltaic and Renewable Energy Engineering, The University of New South Wales, Sydney, NSW 2052, Australia

Correspondence should be addressed to Pei Hsuan Doris Lu; p.lu@unsw.edu.au

Received 2 February 2015; Revised 26 June 2015; Accepted 1 July 2015

Academic Editor: Zijie Yan

Copyright © 2015 Pei Hsuan Doris Lu et al. This is an open access article distributed under the Creative Commons Attribution License, which permits unrestricted use, distribution, and reproduction in any medium, provided the original work is properly cited.

This paper demonstrates that silicon can be locally doped with aluminium to form localised p^+ surface regions by laser-doping through anodic aluminium oxide (AAO) layers formed on the silicon surface. The resulting p^+ regions can extend more than $10\ \mu\text{m}$ into the silicon and the electrically active p-type dopant concentration exceeds $10^{20}\ \text{cm}^{-3}$ for the first $6\text{--}7\ \mu\text{m}$ of the formed p^+ region. Anodic aluminium oxide layers can be doped with other impurities, such as boron and phosphorus, by anodising in electrolytes containing the extrinsic impurities in ionic form. The ions become trapped in the formed anodic oxide during anodisation, therefore enabling the impurity to be introduced into the silicon, with aluminium, during laser-doping. This codoping process can be used to create very heavily doped surface layers which can reduce contact resistance on metallisation, whilst the deeper doping achieved by the intrinsic aluminium may act to shield the surface from minority carriers. Laser-doping through AAO layers can be performed without introducing any voids in the silicon or fumes which may be harmful to human health.

1. Introduction

Laser-doping is a process of incorporating dopants into a semiconductor by using a laser to scribe through a layer that contains a dopant source. Introduction of p-type dopants by laser-doping of silicon can be used to form p^+ silicon surface regions which can act as local emitter regions for n-type solar cells or reduce both the contact resistance at the metal/silicon interface and the dark saturation current density by shielding the minority carriers from the high surface recombination velocity at the silicon interface of p-type solar cells [1, 2]. An approach that has been reported by many is to form aluminium-alloyed local back surface field (BSF) regions by firing screen printed aluminium paste through openings by either laser ablation or laser-doping in a rear dielectric layer [3–6]. This process can therefore potentially eliminate the multiple steps required in performing masked solid-state diffusion processes for the fabrication of silicon solar cells. Wang et al. reported the use of a poly boron solution which was spin-coated on a silicon surface as a dopant source for laser-doping [2]; however it has been shown that very low laser speeds are required to achieve significant dopant incorporation from

this dopant source [1, 7]. Furthermore, fumes generated due to laser scribing through the poly boron film may present a risk to human health [8]. Dielectric layers have also been previously investigated as dopant sources for a subsequent laser-doping process, with the advantage of this process being that the dielectric layer can passivate the surface outside of the laser-doped regions [9–12].

In this paper we report the use of anodic aluminium oxide (AAO) as a dopant source for laser-doping and in particular the formation of p^+ doped silicon regions. These layers, which can be formed by anodising aluminium over an intervening silicon dioxide or silicon nitride dielectric layer on a silicon wafer, have been shown to improve the effective minority carrier lifetime in silicon wafers [13–15] and may also impart enhanced light trapping for thin silicon solar cells due to their nanoporous structure [16]. Being able to also provide a source of aluminium to dope the underlying silicon and form p^+ regions for metal contacting purposes may make these layers useful multifunctional materials for future photovoltaic applications. In [14], residual aluminium has been reported at the valley of pyramid and this residual aluminium could also contribute as a dopant source in laser-doping process. In

the paper, we demonstrate laser-doping of silicon using the intrinsic aluminium of an AAO layer, metallic aluminium of the residual aluminium from anodisation process, and the extrinsic impurities incorporated in the anodic oxide layer by anodising the aluminium in different electrolytes. It has been previously shown that during anodisation, ions from the electrolyte can be trapped in the AAO layer [17, 18]. We show the incorporation of both boron and phosphorus into silicon by laser-doping through an AAO layer formed by anodising aluminium in boric acid (H_3BO_3) and phosphoric acid (H_3PO_4), respectively.

2. Experimental

Alkaline-textured Czochralski (Cz) boron-doped 1–3 Ω cm silicon wafer fragments of area ~ 16 cm² were lightly diffused with phosphorus to an emitter sheet resistance of ~ 100 Ω/\square . The residual phosphorus at the rear surface was removed by etching and 10 nm of SiO_2 was thermally grown on both surfaces. Silicon nitride was deposited using plasma-enhanced chemical vapour deposition (Roth and Rau AK400) to a thickness of 65 and 200 nm on the front and rear surfaces of the wafer fragments, respectively.

An aluminium layer of thickness 600 nm was thermally evaporated onto the rear SiN_x surface of wafer fragments and anodised in an electrolyte comprising either (i) 0.5 M H_2SO_4 at 25 V; (ii) 0.5 M H_2SO_4 and 0.5 M H_3BO_3 at 25 V; or in 0.5 M H_3PO_4 at 37 V. Anodisation was performed as previously described by Lu et al. [13]. The anodisation rate when the electrolyte of 0.5 M H_3PO_4 was used is much slower than when it was anodized in 0.5 M H_2SO_4 ; therefore, the anodisation voltage for the electrolyte of 0.5 M H_3PO_4 was increased to maintain a similar anodisation time. A dopant layer of poly boron source (PBF1; manufactured by FILMTRONICS) was applied to the remaining wafers by spin-coating at 2000 rpm for 30 s and then heating at 200°C for 13 min. Regions of area 2 cm \times 2 cm were laser-doped through either the spin-coated layer of poly boron source or the AAO layer by scribing lines spaced 20 μm apart as laser beam diameter ($1/e^2$) ($=20$ μm) was used by a 532 nm laser at a speed of 500 mm/s and power of 15 W.

Exemplar lines were also laser-scribed through the different dopant sources for scanning electron microscope (SEM) imaging. The secondary ion mass spectrometry (SIMS) doping profiles of the laser-doped regions were measured using a Cameca ims4f with cesium (Cs^+) sputtering ions at voltage of 10 kV. Electrochemical capacitance voltage measurements were performed using a circular measuring area with a diameter of 3.57 mm. Finally, TEM cross-sectional images of the laser-doped regions were recorded to ascertain the structural properties of the laser-doped regions.

3. Results and Discussion

Figure 1(a) shows the SIMS profile of a region that was laser-doped through spin-coated poly boron dopant source. The profile shows the presence of both the B^{10} and B^{11} isotopes of boron, which have a natural abundance of 20% and 80%, respectively [19]. The boron from the poly boron solution is

typically B^{11} dominant [20] which may explain why the natural abundance ratio is not strictly observed in the profile. The boron from the spin-on source was incorporated in the silicon to a depth of 12 μm ; however the boron concentration is around 10^{19} cm⁻³ only in the depth of 1 to 8 μm .

Laser-doping offers the ability to selectively heat a region without heating the bulk of the Si wafer. Laser beams can generate sufficient heat to melt the Si. The wide range in laser power and wavelength enables patterning and melting of Si for different applications. Laser fluence (energy per unit area) which can be controlled by laser power and laser speed determines the thermal energy introduced into the Si; laser wavelength determines the penetration depth of the laser beam within the Si wafer. During laser-doping the silicon under the laser-irradiated region starts to melt at 1414°C and the molten front extends into the silicon. When the thermal energy is dissipated, recrystallisation of the molten silicon starts to occur [1, 21]. Impurities from both the applied dopant source and the SiN_x layer are introduced into the molten region and diffuse down their concentration gradients in the melt. The process of impurity incorporation is further complicated by the existence of temperature gradients which sensitively depend on the laser energy profile and differences in the segregation coefficients of the impurities that are introduced into the molten silicon. As the laser-melted region cools the doped molten silicon recrystallises and impurities may continue to diffuse as the crystallised silicon cools further. Impurities that have larger diffusion coefficients in molten silicon are incorporated deeper in the silicon [1] with the incorporated impurity concentration being also determined to some extent by the impurity's segregation coefficient for silicon. The fact that boron was incorporated to a depth of 12 μm in Figure 1(a) implies that the molten silicon region extended at least that far into the silicon wafer.

Figure 1(b) shows the SIMS profile of a region laser-doped through an AAO layer which was formed by anodising a 600 nm aluminium layer which had been thermally evaporated on the SiN_x surface of silicon wafer. Anodisation was performed at 25 V in an electrolyte comprising 0.5 M H_2SO_4 and 0.5 M H_3BO_3 . Aluminium was the dominant dopant introduced into the silicon during the laser-doping process, penetrating to a depth of 11 μm , whereas the boron was only incorporated to a depth of 1 μm . Note, due to the much lower boron concentration in this profile, only a B^{11} signal was detected by SIMS. The difference in the incorporation depth of the aluminium and boron in Figure 1(b) cannot be fully accounted for on the basis of their different diffusion coefficients in molten silicon (aluminium: $7.0 \pm 3.1 \times 10^{-4}$ cm²s⁻¹ compared to boron: $2.4 \pm 0.7 \times 10^{-4}$ cm²s⁻¹ [22]). Kuhlmann et al. [23] report an enhancement in the solid-state diffusion of aluminium in the presence of boron by a factor of three. It was proposed that this enhancement was due to a supersaturation of self-interstitials caused by the presence of boron. It is interesting to speculate that similar diffusion-enhancement processes may exist for diffusion in molten silicon during laser-doping processes.

Dopant incorporation into silicon during laser-doping may also be affected by the segregation coefficient of the

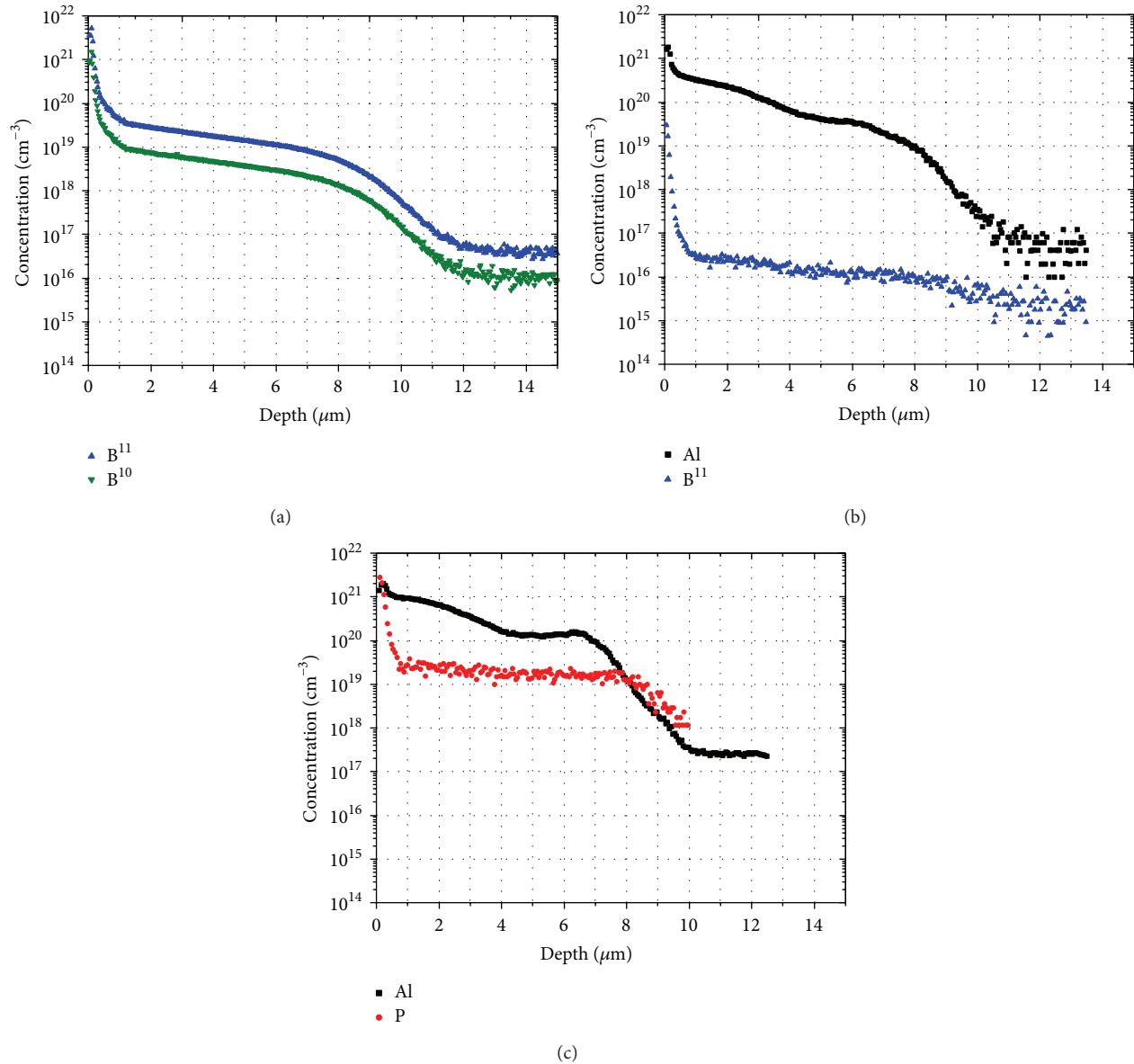


FIGURE 1: SIMS profiles of 4 cm² square laser-doped regions that were formed by scribing laser lines 20 μm apart using a 532 nm laser and a speed of 500 mm/s and laser power of 15 W. In (a) the laser lines were scribed through a spin-coated boron dopant layer. The profiles of detected boron 10 (▼) and boron 11 (▲) are shown. In (b) laser-doping was performed through an AAO layer that was formed by anodising aluminium at 25 V in an electrolyte comprising 0.5 M of H₂SO₄ and 0.5 M of H₃BO₃. The profiles show detected boron 11 (▲) and aluminium (■). In (c) laser-doping was performed through an AAO layer formed by anodising aluminium in 0.5 M H₃PO₄ at 37 V. The profile shows detected phosphorus (●) and aluminium (■).

diffusing impurities. The segregation coefficient of boron in silicon at thermal equilibrium is 0.8 which is considerably larger than the corresponding value of 0.002 for aluminium [24]. If thermal equilibrium was approached during the laser-doping process, it would be expected that significantly more boron than aluminium would be incorporated in the recrystallised silicon. The fact that this was not observed suggests that laser-doping is not an equilibrium process even at the relatively slow processing speeds used in this study, and boron incorporation in the silicon was limited by its diffusion in

the molten silicon. The effects of segregation between liquid and solid were considered to be relatively minor in the laser melting/recrystallization process, where large thermal and concentration gradients evolve over a rapid time frame, and they would be expected to vary during the recrystallization process. As has been previously noted, thermodynamic equilibrium segregation coefficients are only strictly correct for slow silicon growth rates in well stirred melts [25]. It could be argued that the higher surface concentration of boron in Figure 1(a) compared to aluminium in Figure 1(b) may be

due to boron's higher segregation coefficient; however this is difficult to substantiate in the absence of accurate data for the effective dopant concentration at the surface prior to laser-doping as the properties of the poly boron film and AAO layer are so different.

For comparison, Figure 1(c) shows the SIMS profile of a similar region laser-doped through an AAO layer that was formed by anodising a 600 nm aluminium layer at 37 V in 0.5 M H_3PO_4 . Although aluminium is incorporated in the silicon to approximately the same depth as the sample which was laser-doped through the AAO layer formed by aluminium anodisation in 0.5 M H_2SO_4 and 0.5 M H_3BO_3 (see Figure 1(b)), its concentration is higher in the doped region indicating increased aluminium incorporation in silicon in the presence of phosphorus. Nagel et al. reported that solid-state diffusion of aluminium was enhanced in the presence of phosphorus due to field-assisted diffusion arising from aluminium diffusing as negatively charged ion and phosphorus diffusing as a positive ion-vacancy pair [23, 26]. Furthermore, the aluminium profile in Figure 1(c) has a local minimum at $5\ \mu\text{m}$. This is similar to the aluminium solid-state diffusion profile (in the presence of phosphorus) reported by Kuhlmann et al. [23] that can be explained by the up-hill migration of aluminium ions towards the surface caused by the electric field of the phosphorus profile.

A significantly higher level of phosphorus incorporation was observed in Figure 1(c) compared to the boron incorporation in Figure 1(b). This could be partly due to the higher anodisation voltage that was required for anodisation in the 0.5 M H_3PO_4 electrolyte, as more impurities from the electrolyte may have become incorporated into the anodic film at higher voltages [17]. The concentration of boron and phosphorus incorporated within aluminium wires, evaporated aluminium film, and AAO was measured by dissolving aluminium wires, evaporated aluminium film, and AAO film in 3 : 1 solution of 37% (w/w) HCl (J. T. Baker) and 70% (w/w) HNO_3 (J. T. Baker) and analysing the solution by inductively coupled plasma-mass spectrometry (ICP-MS). The concentration of phosphorus within the AAO layer is more than 7 times larger than that of boron (2116 ppm to 15795 ppm) as a result of these particular anodisation conditions, which might result in a difference in surface concentration between boron and phosphorus. However, the increased phosphorus incorporation in silicon compared to boron may also be due to the larger diffusion coefficient of phosphorus ($5.1 \pm 1.7 \times 10^{-4}\ \text{cm}^2\ \text{s}^{-1}$) [22] compared to boron in molten silicon.

The difference in the incorporation depth of the aluminium and boron in Figure 2 was assumed to be at least in part due to the larger diffusion coefficient of aluminium ($7.0 \pm 3.1 \times 10^{-4}\ \text{cm}^2\ \text{s}^{-1}$) compared to boron ($2.4 \pm 0.7 \times 10^{-4}\ \text{cm}^2\ \text{s}^{-1}$) in molten silicon [22]. To examine the role of the differing diffusion coefficients in molten Si, dopant profiles were calculated assuming a Gaussian diffusion profile, a surface dopant concentration of $10^{21}\ \text{cm}^{-3}$, and a diffusion time of $30\ \mu\text{s}$ for aluminium (\blacksquare ; $D = 7.0 \times 10^{-4}\ \text{cm}^2\ \text{s}^{-1}$), B (\blacktriangle ; $D = 2.4 \times 10^{-4}\ \text{cm}^2\ \text{s}^{-1}$), and P (\bullet ; $D = 5.1 \times 10^{-4}\ \text{cm}^2\ \text{s}^{-1}$) in Figure 2 [22]. The diffusion time was selected in order to match the penetration depth of the aluminium. It is clear from Figure 1

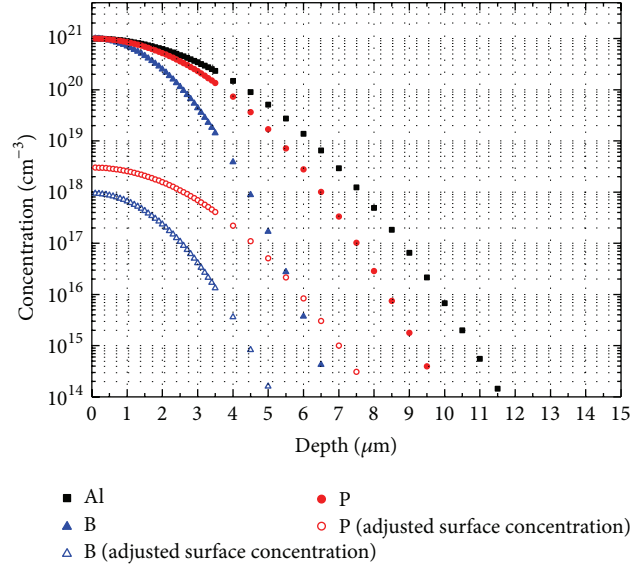


FIGURE 2: Simulated dopant profile of Al (\blacksquare), B (\blacktriangle), and P (\bullet) assuming a Gaussian diffusion profile, a surface concentration of $10^{21}\ \text{cm}^{-3}$, and a diffusion time of $30\ \mu\text{s}$. The open triangles (\triangle) and circles (\circ) represent the simulated doping profile of B and P when the surface concentration was adjusted according to concentration ratio with AAO layer.

that the measured dopant profiles cannot be fully explained by differences in the diffusion coefficients in molten silicon. Even when the surface concentration of boron and phosphorus was adjusted to the lower concentration implied by the ratio (open symbols in Figure 2), the modelling still does not explain the 3 order concentration differences between boron and phosphorus as shown in Figure 1. In other words, the difference in the incorporation depth of the Al, phosphorus, and boron in Figure 2 cannot be fully accounted for on the basis of their different diffusion coefficients in molten silicon. However, the laser-doped lines might slightly overlap to each other to create a laser-doped square for SIMS measurement. With this laser-doping condition, it is highly possible that the silicon remains in a molten state longer than simulated time used in Figure 2. The solidification time of the molten silicon can be very different at $5\ \mu\text{m}$ and the surface.

Although Figure 1 demonstrates that both intrinsic (e.g., aluminium) and extrinsic (e.g., boron and phosphorus) impurities in AAO layers can be incorporated into silicon, device performance requires that the introduced dopants are also electrically active. Figure 3 shows the p-type dopant profile, determined using electrochemical capacitance voltage (ECV) measurements, for regions laser-doped through the poly boron spin-on dopant source and through an AAO layer formed by anodising aluminium at 25 V in an electrolyte comprising 0.5 M H_2SO_4 and 0.5 M H_3BO_3 . Although the (electrical) junction depth exceeded $10\ \mu\text{m}$ in both cases, laser-doping through the AAO layer resulted in a higher dopant concentration in the p^+ region than the equivalent process using the poly boron spin-on source. The electrically active p-type dopant concentration exceeded $10^{20}\ \text{cm}^{-3}$ over the first $4\ \mu\text{m}$ of the region formed by doping through the AAO layer,

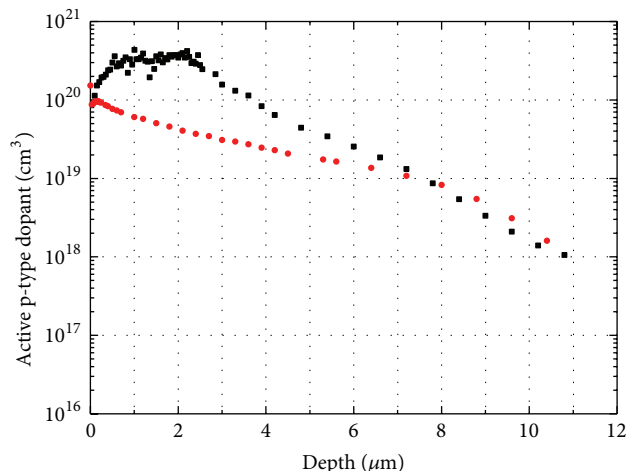


FIGURE 3: ECV profiles showing electrically active p-type dopant concentration in a 4 cm^2 region which was laser-doped through (a) spin-coated poly boron dopant source (●) and (b) an AAO layer formed by anodising aluminium at 25 V in an electrolyte comprising 0.5 M of H_2SO_4 and 0.5 M of H_3BO_3 (■). Both regions were formed by laser-doping a sequence of lines which were spaced $20 \mu\text{m}$ using a 532 nm laser and a speed of 500 mm/s and laser power of 15 W.

whereas this dopant concentration was only achieved over the first 300 nm of the region laser-doped through the poly boron spin-on source. As discussed previously, the greater amount of p-type dopant is being incorporated through melting results from laser-doping through the AAO. This is primarily due to aluminium's larger diffusion coefficient. Consequently, when laser-doping uses the same laser speed and power, more aluminium can diffuse into the silicon and diffuses further from the surface than the introduced boron. Although the laser-doping conditions were identical for both samples, the thermal energy absorbed by the silicon would have been different because the reflectance of the AAO layer at 532 nm was much higher than measured for 200 nm of SiN_x , consequently less laser power would have been less into the AAO-coated silicon.

Figure 4 shows SEM top-view images of lines laser-doped through the poly boron spin-on source (Figure 4(a)), through an AAO layer formed by anodising aluminium in 0.5 M H_2SO_4 (Figure 4(b)), and through an AAO layer formed by anodising aluminium at 25 V in an electrolyte comprising 0.5 M H_2SO_4 and 0.5 M H_3BO_3 (Figure 4(c)). All the lines were laser-doped using a laser speed of 500 mm/s and power of 15 W. Large "holes" are evident along the line laser-doped through the poly boron spin-on source, whereas the lines which were laser-doped through AAO layers were smooth and free of holes. Sugianto also observed "holes" after laser-doping through the same poly boron dopant source and attributed them to trapped gas impurities which vent at the surface. She showed that the size and density of holes decreased when the laser scan speed was increased supporting the theory that reduced impurity incorporation occurs at faster laser speeds [21]. It is also notable that the line that was laser-doped through the poly boron spin-on source appears raised above the textured silicon nitride surface. This is quite

different morphologically from the lines laser-doped through AAO layers where the level of the line lies below the surface of the dielectric layer.

Given the surface manifestation of laser-doping defects in Figure 5(a), transmission electron microscopy (TEM) cross-sectional images and energy dispersive X-ray (EDX) mapping images were used to investigate whether further evidence of gas generation or other defects could be detected below the surface of the laser-doped regions. Figure 5 shows TEM and corresponding EDX images of regions which were laser-doped through boron spin-on dopant source (Figures 5(a) and 5(c)) and through an AAO layer formed by anodisation of aluminium in 0.5 M H_2SO_4 at 25 V (Figures 5(b) and 5(d)). Both lines were formed using a laser speed of 500 mm/s and power of 15 W. A large void, which was $\sim 2 \mu\text{m}$ in length, is evident in Figure 5(a) confirming that voids are also formed in the laser-doped silicon and not just on the surface. If these voids are fully contained within the laser-doped p^+ silicon, then their electrical impact will be minor as the electron concentration is low in these regions and consequently recombination associated with the defects will be minimal. However if the voids result in crystal stress, then it is possible that crystal defects (e.g., dislocations) may be propagated into the bulk of the wafer. In comparison the laser-doped silicon region in Figure 4(b) is free of voids and crystal structure defects. The AAO layer is only partially ablated by the laser-scribing and the residue of the layer retains a network of pores.

The EDX image in Figure 5(c) depicts the laser-doped region in Figure 5(a) and indicates low levels of boron (blue) incorporation in the laser-doped silicon region. Boron is difficult to detect using EDX when the window of the detector crystal is composed of beryllium because the X-ray signal is attenuated if the element is lighter than sodium. Since this was the case for these analyses, boron identification in the EDX maps in Figure 5 may not be reliable. The EDX image in Figure 5(d) depicts the laser-doped region in Figure 5(b). Large regions of aluminium (red) can be seen in the silicon showing that the dopant has not been uniformly incorporated into the silicon lattice. The nonuniform aluminium incorporation may be accentuated by the method of scribing multiple adjacent laser lines to form a square region for analysis; however it is interesting to note the boron-doping in Figure 5(c) appeared more uniform.

In both samples a layer rich in oxygen forms at the surface of the laser-doped region. In the case of the sample that was laser-doped through the AAO layer the layer appears of uniform thickness and $\sim 50 \text{ nm}$ in thickness. It may comprise residual oxide from the dielectric stack that has become segregated to the surface of the laser-doped region or it may also form due to molten silicon reacting with oxygen from the ambient. The ramifications of this are that before metal contacting can be achieved deglazing will be necessary.

4. Conclusions

This paper demonstrates that aluminium can be introduced into silicon to form localised p^+ surface regions by laser-doping through an AAO layer formed on the silicon surface.

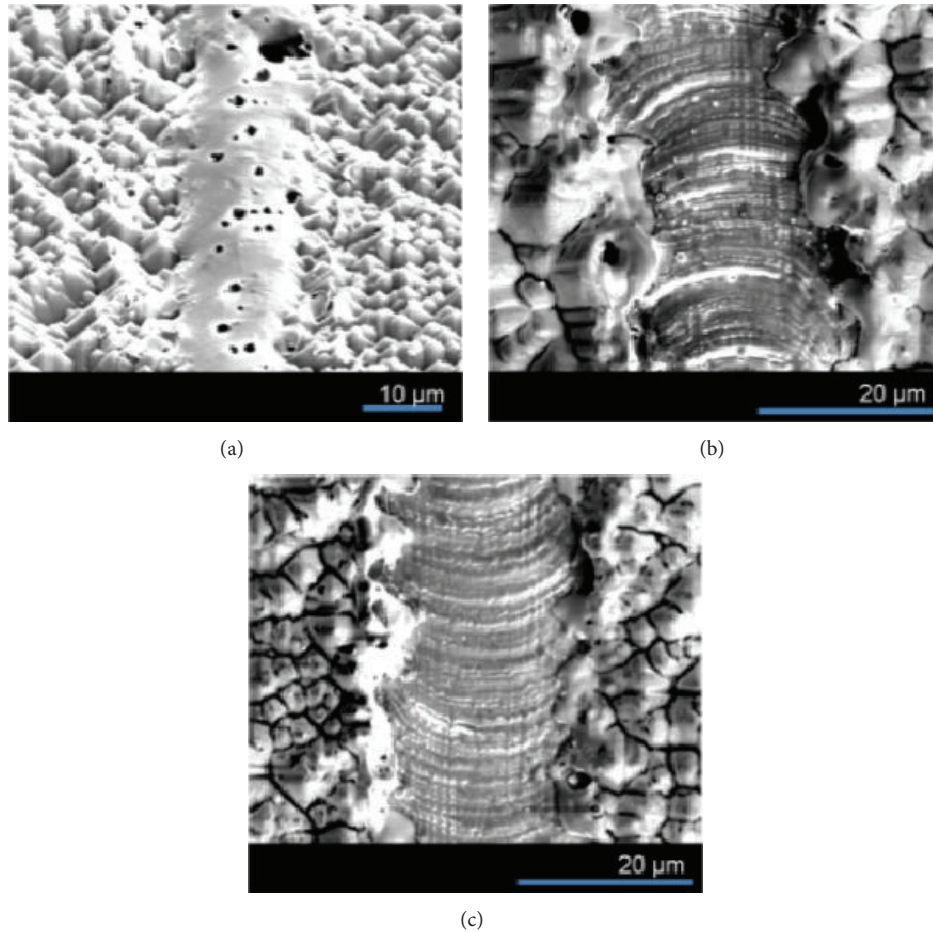


FIGURE 4: Scanning electron microscope top-view images of (a) a line laser-doped through the boron spin-on dopant source; (b) a line laser-doped through an AAO layer which was formed by anodisation of aluminium in 0.5 M H_2SO_4 ; and (c) a line laser-doped through an AAO layer which was formed by anodisation of aluminium at 25 V in an electrolyte comprising 0.5 M H_2SO_4 and 0.5 M of H_3BO_3 . All the lines were scribed by a 532 nm laser using a speed of 500 mm/s and power of 15 W.

The introduced aluminium can penetrate the silicon at least $10\ \mu\text{m}$ from the surface with the laser-doping conditions used, and unlike laser-doping through a poly boron spin-coated layer the concentration of electrically active p-type dopant exceeds $1 \times 10^{20}\ \text{cm}^{-3}$ for the first 6-7 μm of the p^+ region. A heavily doped p^+ region can be formed by laser scribed through boron-doped AAO which was formed by anodizing aluminium in the mixture of 0.5 M H_2SO_4 and 0.5 M H_3BO_3 at 25 V. The higher dopant concentration in the p^+ regions, which occurs most likely because aluminium diffuses \sim three times faster than boron in molten silicon, can result in more effective shielding of minority carriers from the silicon surface and hence improved device performance.

The anodic oxide layers can be doped with other impurities (e.g., boron and phosphorus) by anodising aluminium in electrolytes containing the extrinsic impurities in ionic form. The ions become trapped in the formed AAO layer during anodisation, therefore enabling the impurity to be introduced into the silicon, with aluminium, during laser-doping. This codoping process can be used to create very heavily doped

surface layers which can reduce contact resistance on metallisation, whilst the deeper doping achieved by the intrinsic aluminium may act more to shield the surface from minority carriers.

It is concluded that laser-doping through AAO layers may be a useful way of forming localised p^+ regions in p-type silicon solar cells. The process can result in more heavily doped p^+ regions than the previously described method of laser-doping through a poly boron source. Furthermore, it can be performed without introducing defects in the silicon or fumes which may be harmful to human health. If AAO layers can be used in this way to create local p^+ regions, whilst also enabling high carrier lifetimes and therefore cell voltages, they may represent a multifunctional material for silicon solar cell passivation and contact formation.

Disclaimer

The views expressed herein are not necessarily the views of the Australian Government, and the Australian Government

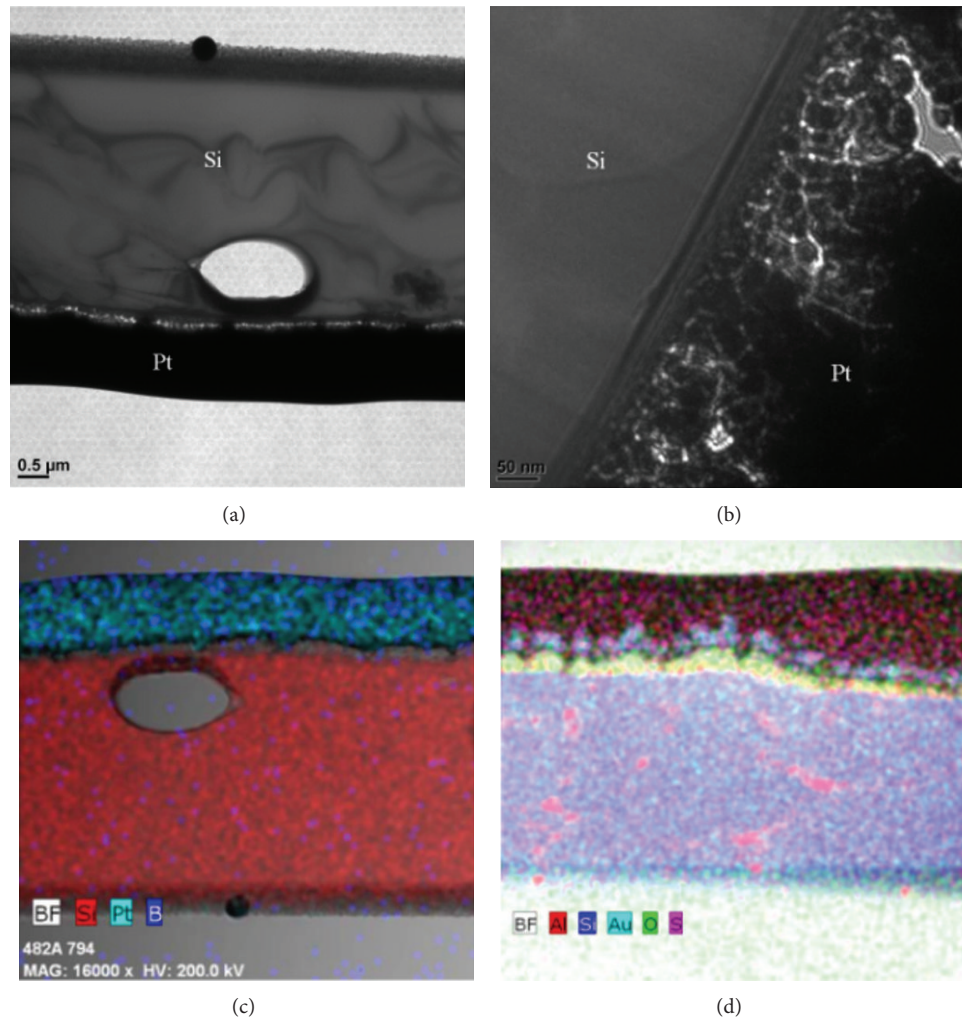


FIGURE 5: Transmission electron microscopy cross-sectional images of regions: (a) laser-doped through a spin-coated boron dopant layer and (b) laser-doped through an AAO layer formed by aluminium anodisation at 25 V in 0.5 M H_2SO_4 . The laser-doping was performed using a 532 nm laser and a speed of 500 mm/s and operation power of 15 W. (c) and (d) show EDX mapping images of (a) and (b), respectively. Note that the orientation of (c) and (d) is changed from (a) and (b).

does not accept responsibility for any information or advice contained herein.

Conflict of Interests

The authors declare that there is no conflict of interests regarding the publication of this paper.

Acknowledgment

This program has been supported by the Australian Government through the Australian Renewable Energy Agency (ARENA). The Australian Government, through ARENA, is supporting Australian research and development in solar photovoltaic and solar thermal technologies to help solar power become cost competitive with other energy sources.

References

- [1] B. Hallam, C. Chan, A. Sugianto, and S. Wenham, "Deep junction laser doping for contacting buried layers in silicon solar cells," *Solar Energy Materials and Solar Cells*, vol. 113, pp. 124–134, 2013.
- [2] Z. Wang, P. Han, H. Lu et al., "Advanced PERC and PERL production cells with 20.3% record efficiency for standard commercial p-type silicon wafers," *Progress in Photovoltaics: Research and Applications*, vol. 20, no. 3, pp. 260–268, 2012.
- [3] S. W. Glunz, J. Benick, D. Biro et al., "n-Type silicon—enabling efficiencies > 20% in industrial production," in *Proceedings of the 35th IEEE Photovoltaic Specialists Conference (PVSC '10)*, pp. 50–56, IEEE, Honolulu, Hawaii, USA, June 2010.
- [4] A. Metz, D. Adler, S. Bagus et al., "Industrial high performance crystalline silicon solar cells and modules based on rear surface passivation technology," *Solar Energy Materials and Solar Cells*, vol. 120, pp. 417–425, 2014.

- [5] B. Tjahjono, M. J. Yang, V. Wu, J. Ting, J. Shen, O. Tan et al., "Optimizing CELCO cell technology in one year of mass production," in *Proceeding of 28th European Photovoltaic Solar Energy Conference and Exhibition*, Paris, France, September 2013.
- [6] L. Tous, R. Russell, M. Debucquoy et al., "Power-loss analysis of advanced PERC cells reaching 20.5% energy conversion efficiency," *Energy Procedia*, vol. 38, pp. 467–473, 2013.
- [7] A. Sugianto, B. Hallam, X. Bai et al., "Over 20%-efficient laser-doped passivated rear contact solar cells on industrial-sized commercial grade p-type CZ wafers," in *Proceedings of the 27th European Photovoltaic Solar Energy Conference and Exhibition*, pp. 700–705, Frankfurt, Germany, 2012.
- [8] (ATSDR), *Toxic Substances Portal for Boron*, ATSDR, 2010, <http://www.atsdr.cdc.gov/phs/phs.asp?id=451&tid=80>.
- [9] B. Paviet-Salomon, S. Gall, R. Monna et al., "Laser doping using phosphorus-doped silicon nitrides," *Energy Procedia*, vol. 8, pp. 700–705, 2011.
- [10] D. Suwito, U. Jäger, J. Benick, S. Janz, M. Hermle, and S. W. Glunz, "Industrially feasible rear passivation and contacting scheme for high-efficiency n-type solar cells yielding a Voc of 700 mV," *IEEE Transactions on Electron Devices*, vol. 57, no. 8, pp. 2032–2036, 2010.
- [11] P. Ortega, I. Martín, G. Lopez et al., "P-type c-Si solar cells based on rear side laser processing of $\text{Al}_2\text{O}_3/\text{SiC}_x$ stacks," *Solar Energy Materials and Solar Cells*, vol. 106, pp. 80–83, 2012.
- [12] I. Martín, P. Ortega, M. Colina, A. Orpella, G. López, and R. Alcobilla, "Laser processing of $\text{Al}_2\text{O}_3/a\text{-SiC}_x\text{:H}$ stacks: a feasible solution for the rear surface of high-efficiency p-type c-Si solar cells," *Progress in Photovoltaics: Research and Applications*, vol. 21, no. 5, pp. 1171–1175, 2013.
- [13] P. H. Lu, K. Wang, Z. Lu, A. J. Lennon, and S. R. Wenham, "Anodic aluminum oxide passivation for silicon solar cells," *IEEE Journal of Photovoltaics*, vol. 3, no. 1, pp. 143–151, 2013.
- [14] Z. Lu, P. H. Lu, J. Cui, K. Wang, and A. Lennon, "Self-patterned localized metal contacts for silicon solar cells," *Journal of Materials Research*, vol. 28, no. 15, pp. 1984–1994, 2013.
- [15] J. Cui, X. Wang, and A. Lennon, "Light-induced anodisation of aluminium for rear surface passivation of silicon solar cells," in *Proceedings of the 28th European PV Solar Energy Conference and Exhibition*, Paris, France, 2013.
- [16] Y. Li, Z. Lu, and A. J. Lennon, "Optical modeling of anodic aluminum oxide for light-trapping in silicon solar cells," in *Proceedings of the Solar Conference*, Melbourne, Australia, 2012.
- [17] J. Lambert, C. Guthmann, C. Ortega, and M. Saint-Jean, "Permanent polarization and charge injection in thin anodic alumina layers studied by electrostatic force microscopy," *Journal of Applied Physics*, vol. 91, no. 11, pp. 9161–9169, 2002.
- [18] L. Zhang, G. E. Thompson, M. Curioni, and P. Skeldon, "Anodizing of aluminium in sulfuric acid/boric acid mixed electrolyte," *Journal of the Electrochemical Society*, vol. 160, no. 4, pp. C179–C184, 2013.
- [19] P. G. Bentley and A. N. Hamer, "Boron-10 abundance in nature," *Nature*, vol. 182, no. 4643, pp. 1156–1157, 1958.
- [20] R. E. Zeebe, "Stable boron isotope fractionation between dissolved $\text{B}(\text{OH})_3$ and $\text{B}(\text{OH})_4^-$," *Geochimica et Cosmochimica Acta*, vol. 69, no. 11, pp. 2753–2766, 2005.
- [21] A. Sugianto, *Development of commercial high-efficiency silicon solar cells using selective emitters and passivated rear contacts [Ph.D. thesis]*, School of Photovoltaics and Renewable Energy Engineering, University of New South Wales, Sydney, Australia, 2011.
- [22] H. Kodera, "Diffusion coefficients of impurities in silicon melt," *Japanese Journal of Applied Physics*, vol. 2, no. 4, pp. 212–219, 1963.
- [23] U. Kuhlmann, D. Nagel, and R. Sittig, "Short-time diffusion of aluminium in silicon and co-diffusion with phosphorus and boron," *Defect and Diffusion Forum*, vol. 143–147, pp. 1009–1014, 1997.
- [24] B. R. Bathey and M. C. Cretella, "Solar-grade silicon," *Journal of Materials Science*, vol. 17, no. 11, pp. 3077–3096, 1982.
- [25] P. S. Ravishankar, L. P. Hunt, and R. W. Francis, "Effective segregation coefficient of boron in silicon ingots grown by the czochralski and bridgman techniques," *Journal of the Electrochemical Society*, vol. 131, no. 4, pp. 872–874, 1984.
- [26] D. Nagel, C. Frohne, and R. Sittig, "Rapid thermal diffusion of aluminum in silicon and its interaction with phosphorus," *Applied Physics A: Materials Science & Processing*, vol. 60, no. 1, pp. 61–65, 1995.

Research Article

Nanocrystallization of Vanadium Borophosphate Glass for Improving the Electrical and Catalytic Properties

Su-Yeon Choi and Bong-Ki Ryu

Department of Material Science and Engineering, Pusan National University, Busan 609-735, Republic of Korea

Correspondence should be addressed to Bong-Ki Ryu; bkryu@pusan.ac.kr

Received 20 March 2015; Accepted 13 May 2015

Academic Editor: Min Liu

Copyright © 2015 S.-Y. Choi and B.-K. Ryu. This is an open access article distributed under the Creative Commons Attribution License, which permits unrestricted use, distribution, and reproduction in any medium, provided the original work is properly cited.

75V₂O₅-10P₂O₅-15B₂O₃ ternary-system glasses were prepared and nanocrystallized to examine the catalytic effect and the variations in their structural and electrical properties. These glasses were annealed in a graphite mold above the glass transition temperature for 2 h and heat-treated at the crystallization temperature for 1, 3, and 5 h. Fourier transform infrared spectroscopy (FTIR) was used to analyze the structural changes in the B-O bonds after nanocrystallization, while X-ray photoelectron spectroscopy (XPS) analysis showed a decrease in V⁵⁺ and an increase in V⁴⁺. X-ray diffraction (XRD) analysis of the structure array (BO₃ + V₂O₅ ↔ BO₄ + 2VO₂) verified these inferred changes. Structural changes induced by the heat treatment were confirmed by analyzing the molecular volume determined from the sample density. Conductivity and catalytic effects were discussed based on the migration of vanadate ions with different valence states due to the increase in VO₂ nanocrystallinity at 275°C. Both conductance and the catalytic effect were higher after nanocrystallization at 275°C for 1 h compared to the annealed sample. Furthermore, compared to the sample heat-treated for 1 h, the conductance and catalytic effect were increased and decreased, respectively, for samples nanocrystallized at 275°C for 3 and 5 h.

1. Introduction

Vanadate glasses containing large amounts of V₂O₅ have multivalent ions of various states mixed in their structure. These glasses have been developed for infrared transmission and as atomic-exchange electroconductive glasses using electron conduction. Studies focusing on improving the performance of these glasses involve changing the electrical conduction properties through low valency (V⁴⁺) to high valency (V⁵⁺) metal-ion electron hopping [1], changing the catalytic properties for the oxidation reaction by altering the valency change between V⁴⁺ and V⁵⁺ [2], and examining the correlation between the glass composition and its characteristics while focusing on the type and condition of V ions or the type and the amount of alkali or alkaline earth metals [3–7].

In 2012, we substituted B₂O₃ for P₂O₅ to improve the chemical resistance and electrical conductivity of vanadium phosphate-based glasses, and we were able to investigate the significance of the correlation between the resulting structure and the electrical, thermal, and chemical properties

[6]. However, the effect of the substitution was insignificant. Moreover, the analysis of the catalytic activity of the oxidation reaction, which is characteristic of V₂O₅, with respect to the vanadate glass was insufficient. On the other hand, if vanadate glass is crystallized and the structure becomes denser, electron tunneling in the glass would occur with a higher frequency [8]. This behavior leads to frequent valency changes in the V cation. It is hypothesized that this change influences the change in the catalytic effect and electrical conductivity. In particular, if the nanocrystalline phases are generated, the specific surface area of the crystalline phases will be maximized. So, property changes due to crystallization appear to be more prominent.

In this study, P₂O₅ was used as a glass former, to which V₂O₅ or other metal oxides are added in order to achieve V₂O₅-like characteristics. We maximized the electrical conductivity and catalytic properties of V₂O₅-B₂O₃-P₂O₅ ternary glass by maximizing the amount of the substitute (B₂O₃ for P₂O₅) to form 75V₂O₅-15B₂O₃-10P₂O₅ ternary glass. It was confirmed that nanocrystallizing this ternary

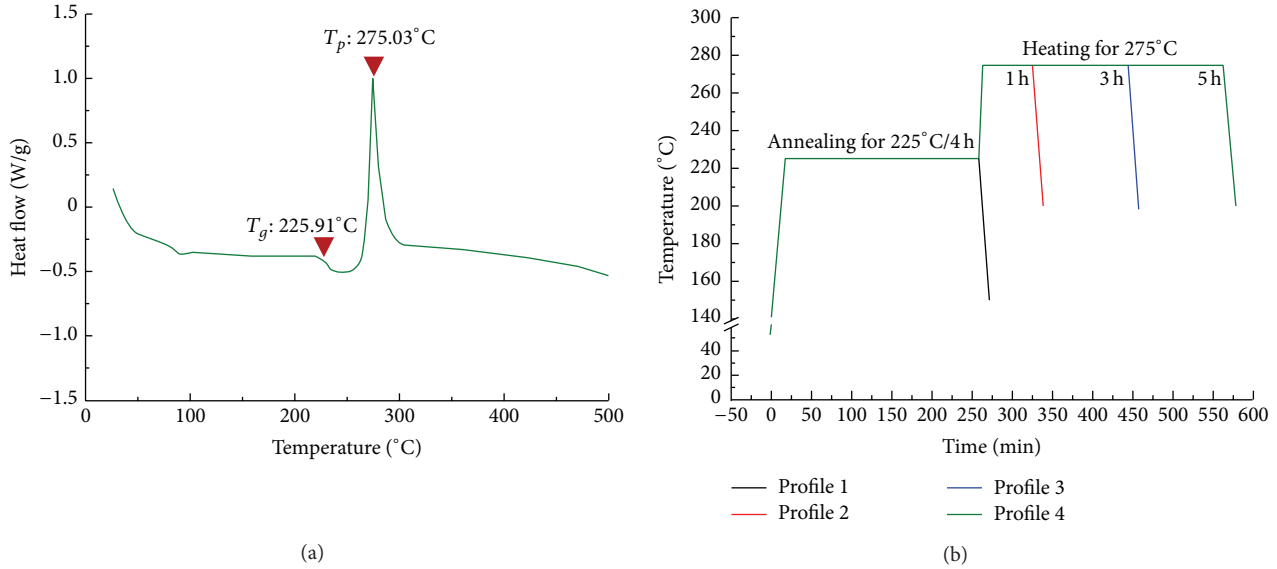


FIGURE 1: Differential scanning calorimetry (a) and resulting heat-treatment profile (b) for all the V_2O_5 -based glasses used in this study.

glass produces $\text{VO}_2(\text{VO}_4)$, $\text{V}_2\text{O}_5(\text{VO}_5)$, and $\text{B}_2\text{O}_3(\text{BO}_4)$ crystalline phases, and the structural change in the nanocrystalline phase was caused by increasing the duration of heat treatment for crystallization. From the results, it was evident that this behavior affected the ratio of V^{5+} to V^{4+} .

We presumed that the changes in the electrical conduction and catalytic properties were induced by the heat treatment. The causes behind the characteristic changes and the action mechanism were investigated through qualitative and quantitative analysis of X-ray diffraction (XRD) patterns, X-ray photoelectron spectroscopy (XPS), and Fourier transform infrared (FTIR) spectroscopy. We examined the quantitative physical properties such as density and molar volume to verify the predicted action mechanism.

2. Materials and Methods

2.1. Glass Preparation and Nanocrystallization. $75\text{V}_2\text{O}_5$ - $15\text{B}_2\text{O}_3$ - $10\text{P}_2\text{O}_5$ glass samples were prepared using reagent-grade $\text{NH}_4\text{H}_2\text{PO}_4$, V_2O_5 , and B_2O_3 (Junsei Chemical Co., Ltd., Japan). The constituents were mixed in an alumina mortar for 10 min to produce multiple batches. Well-mixed batches were first melted in an alumina crucible using an electrical furnace at 200°C for 1 h (first calcination), subsequently at 500°C for 2 h (second calcination), and finally at 800°C for 2 h. The resultant melt was quenched between two stainless steel plates.

The as-prepared sample was crushed in an automatic grinding mixer and sieved through a 325 mesh. This powder (particle size below $44\ \mu\text{m}$) was used for differential scanning calorimetry (DSC), XRD, XPS, FTIR, and thermogravimetric analysis (TGA) measurements.

DSC was performed on the samples using an SDT (SDT Q600, TA instrument, USA) to determine both the glass transition (T_g) and the crystallization (T_c) temperatures, as shown in Figure 1(a). The glasses were annealed in a graphite

mold above T_g for 4 h and heat-treated at T_c for 1, 3, or 5 h. Detailed heating profiles are provided in Figure 1(b).

The glass samples used for the experiments (electrical conductivity, density, and molar volume) were rectangular parallelepipeds and their surfaces were polished using SiC paper (#220–1000).

2.2. Measurement. XRD measurements were taken in a Rigaku Co. RINT 2000 using $\text{Cu-K}\alpha$ radiation in the 10 – $80^\circ 2\theta$ range with a step size of 0.02° . The existence of the nanocrystal phase was confirmed using the resultant XRD patterns. The nanocrystal phases were observed by field emission scanning electron microscopy (FE-SEM, Carl Zeiss, Supra 25).

We investigated the structural changes using FTIR spectroscopy. Powdered samples mixed with KBr (mixing ratio 1:1200) were prepared and dried at 100°C in a desiccator to form pellets. A Spectrum GX (Perkin Elmer Co, USA) spectrometer was used to perform FTIR. Room temperature IR spectra were recorded from 400 to $1400\ \text{cm}^{-1}$ (injection number of times: 20; resolving power: $2\ \text{cm}^{-1}$).

XPS was used to analyze the change in the valency of vanadium cations in the glass. XPS measurements were taken using the ESCALAB250 XPS system and the Theta Probe XPS system using monochromatic $\text{Al-K}\alpha$ ($h\nu = 1486.6\ \text{eV}$) radiation. The analysis area was $400\ \mu\text{m}$ and the data was compensated using C1s ($284.6\ \text{eV}$) as the reference.

The catalytic properties and electrical conductivity are the main characteristics considered in this study. First, in order to measure the electrical conductivity of each specimen, the carrier density was measured at room temperature using a Hall-effect measurement system (HMS-3000 Hall Measurement System, ECOPIA). Furthermore, to examine the catalytic effect of the glass samples applied to the oxidation of fatty acids (linoleic acid and stearic acid) and carbon, we performed TGA on two samples obtained by mixing 20 mg of

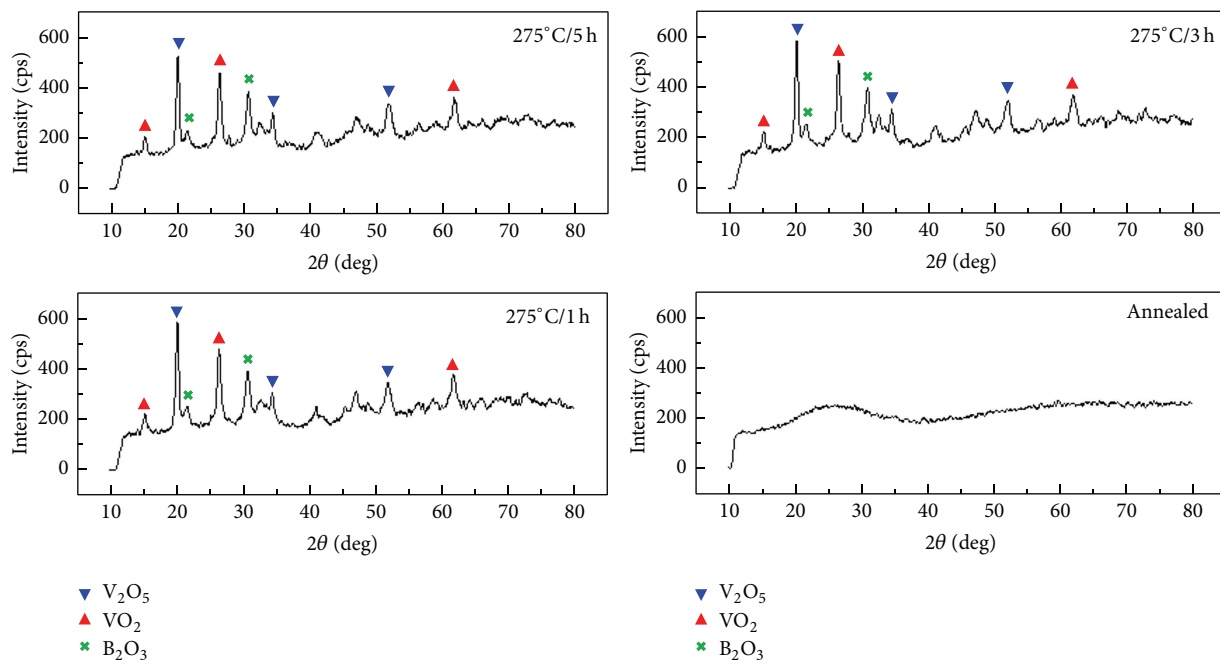


FIGURE 2: XRD patterns of $75\text{V}_2\text{O}_5$ - $15\text{B}_2\text{O}_3$ - $10\text{P}_2\text{O}_5$ glasses heat-treated at 275°C .

fatty acid with 20 mg of glass powder and gas chromatography with a mass spectrometer (GC-MSD) on a sample obtained by mixing 2 mg of carbon with 8 mg of glass powder. TGA measurements were obtained between room temperature and 600°C at a heating rate of $10^\circ\text{C}/\text{min}$ in an atmosphere of 5 vol% using a simultaneous TGA/DSC (Q600, TA Instruments, Inc.). The fatty acids used in the experiments are reagent-grade stearic acid (95%) and technical grade linoleic acid (60–74%, GC), both from Sigma-Aldrich Co. GC-MSD measurements were obtained between room temperature and 450°C at a heating rate of $10^\circ\text{C}\cdot\text{min}^{-1}$ in an atmosphere of He and O_2 using a 5975MSD-6890N GC (Agilent). He gas was used at a flow rate of 20 mL/min and O_2 gas was used at a flow rate of 2 mL/min.

Changes in quantitative properties due to structural changes were confirmed using the molar volume and density measurements. The densities of the glass samples were measured using the Archimedes method using a GH-200 (AND Co, Korea), and the molar volume (V_M) was calculated from the measured density using $V_M \equiv \bar{M}/\rho$ [9], where \bar{M} is the average molar weight of glass.

3. Results and Discussion

3.1. Analysis of Nanocrystal Phases. Figure 2 shows the diffraction patterns of all the samples studied, which were annealed for 4 h and heat-treated at 275°C for different durations (1, 3, and 5 h). A V_2O_5 phase (V^{5+} /JCPDS-PDF 85-0601) coexisting with the VO_2 (V^{4+} /JCPDS-PDF 73-0514) and B_2O_3 (BO_4 /JCPDS-PDF 760781) phases was detected in samples heat-treated at 275°C . As the holding time at 275°C increased, the relative amounts of VO_2 and B_2O_3 increased while the relative amount of V_2O_5 decreased; that is, VO_2

and BO_4 structures are strengthened by nanocrystallizing the $75\text{V}_2\text{O}_5$ - $15\text{B}_2\text{O}_3$ - $10\text{P}_2\text{O}_5$ ternary glass. Combining this fact with the results of the FTIR analysis (Section 3.3), which explains the structural change of BO_3 to BO_4 , the nanocrystallization of the VO_2 phase occurred and this nanocrystal was strengthened while the V_2O_5 phase was comparatively weakened as the heat treatment at 275°C progressed. This suggested that a structural change, indicated by the reaction $\text{BO}_3 + \text{VO}_5(\text{V}_2\text{O}_5) \rightarrow \text{BO}_4 + \text{VO}_4(\text{VO}_2)$, was induced by the heat treatment at 275°C . This structural change is a factor that affects the electrical conduction and catalytic properties of the vanadate glass.

Figure 3 shows the SEM images of all samples studied, which were annealed for 4 h and heat-treated at 275°C for different durations (1, 3, and 5 h). Nanocrystallines of VO_2 phase were detected in samples heat-treated at 275°C . As the holding time at 275°C increased, the amounts of nanocrystalline increased.

3.2. XPS Spectroscopy. To quantitatively determine the change in the vanadium ion valency, we performed an XPS analysis on each glass sample. The V 2p spin orbit doublet spectra of $75\text{V}_2\text{O}_5$ - $15\text{B}_2\text{O}_3$ - $10\text{P}_2\text{O}_5$ glasses are shown in Figure 4. The XPS analysis was performed while maintaining the same X-ray energy, X-ray-to-sample positioning, and sampling time for all the four samples in accordance with the nanocrystallization conditions. V 2p peaks appeared asymmetrically in each sample, indicating that the vanadium ions are present in more than one oxidation state [10]. According to previous studies on vanadium phosphate glasses, core level spectra of V^{5+} appear at a binding energy (BE) of 517.3 eV, while that of V^{4+} appears at 516.0 eV [11–14]. Therefore, when the V 2p_{3/2} core level spectrum is fitted to the BE

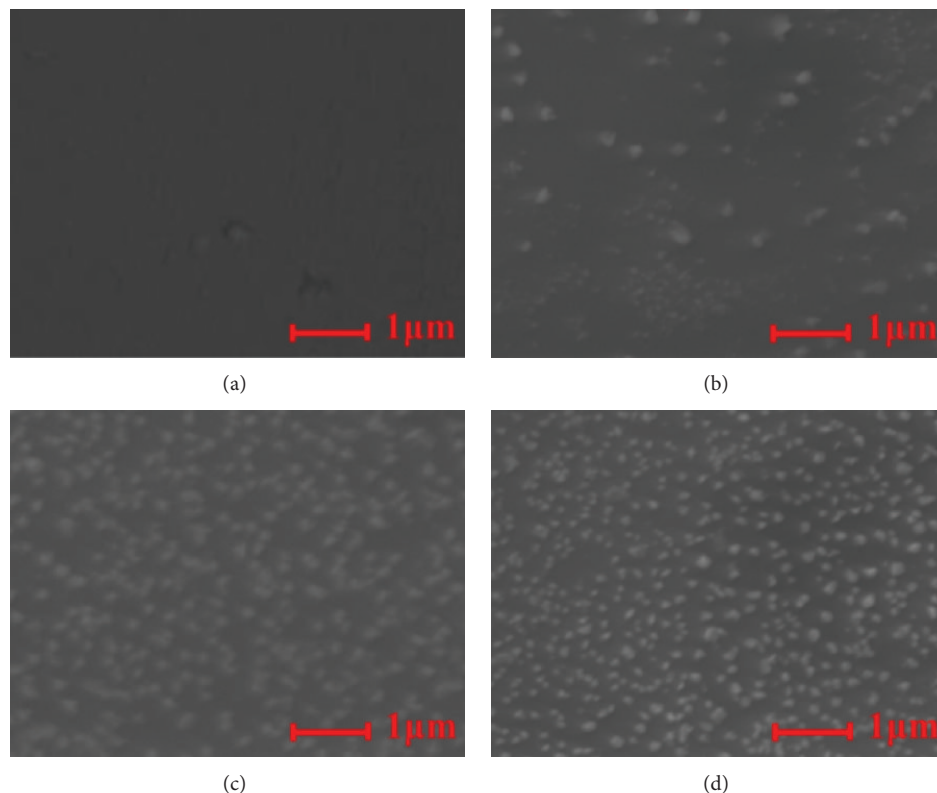


FIGURE 3: SEM images of $75\text{V}_2\text{O}_5\text{-}15\text{B}_2\text{O}_3\text{-}10\text{P}_2\text{O}_5$ glasses (a) annealed at 225°C and heated for crystallization at 275°C for (b) 1, (c) 3, and (d) 5 h.

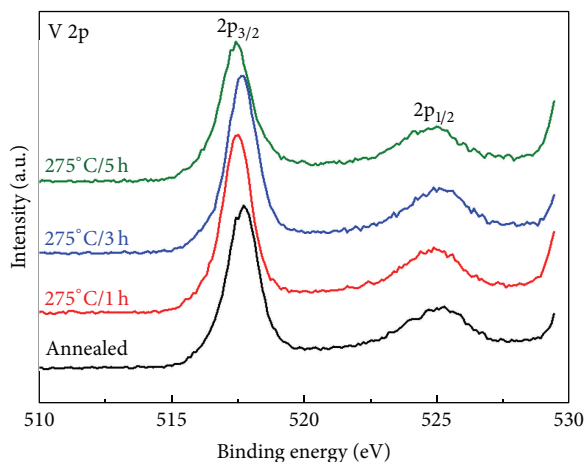


FIGURE 4: Core level V 2p spectra for the $75\text{V}_2\text{O}_5\text{-}15\text{B}_2\text{O}_3\text{-}10\text{P}_2\text{O}_5$ glasses heat-treated at 275°C .

of 517.3 eV of the V^{5+} ions and 516.1 eV of the V^{4+} ions, quantitative analysis for the concentration of V^{5+} and V^{4+} became possible [15]. The V^{5+} and V^{4+} peaks of the $75\text{V}_2\text{O}_5\text{-}15\text{B}_2\text{O}_3\text{-}10\text{P}_2\text{O}_5$ glass, obtained from the vanadium Gaussian-Lorentzian peaks, fitted using the least squares method, are shown in Figure 5. The relative content ratios of $\text{V}^{5+}/\text{V}_{\text{total}}$ and $\text{V}^{4+}/\text{V}_{\text{total}}$ obtained using this fit are shown in Table 1.

It was found that the content of the V^{5+} in glass was reduced and V^{4+} was increased by nanocrystallizing $75\text{V}_2\text{O}_5\text{-}15\text{B}_2\text{O}_3\text{-}10\text{P}_2\text{O}_5$ glass and increasing the heat treatment time for crystallization. This means that the V^{5+} to V^{4+} reduction reaction occurs during nanocrystallization at 275°C and increments in the heat treatment duration. This behavior is in agreement with the trends in the catalytic properties (Section 3.5) and electrical conductivity (Section 3.4). We have confirmed that the changes in concentration and state of vanadium ions due to nanocrystallization contribute directly to the characteristic change in the $75\text{V}_2\text{O}_5\text{-}15\text{B}_2\text{O}_3\text{-}10\text{P}_2\text{O}_5$ glass.

3.3. FTIR Spectroscopy. XPS analysis was performed to verify the changes in the concentration and state of the vanadium ions in the glass due to nanocrystallization. The structural changes were expected to induce a change in the concentrations of V^{5+} and V^{4+} . Results of FTIR spectroscopy provided a direct evidence for the BO_4 restructuring observed in the XRD analysis. The infrared spectra (at $400\text{--}2000\text{ cm}^{-1}$) of the $75\text{V}_2\text{O}_5\text{-}15\text{B}_2\text{O}_3\text{-}10\text{P}_2\text{O}_5$ glass annealed for 4 h and heat-treated at 275°C for different durations (1, 3, and 5 h) are shown in Figure 6. The vibration modes of the borate network were found to be active mainly in three infrared regions, as previously reported [16, 17]. The group of bands located at $1200\text{--}1600\text{ cm}^{-1}$ is attributed to the B-O bonds in the trigonal

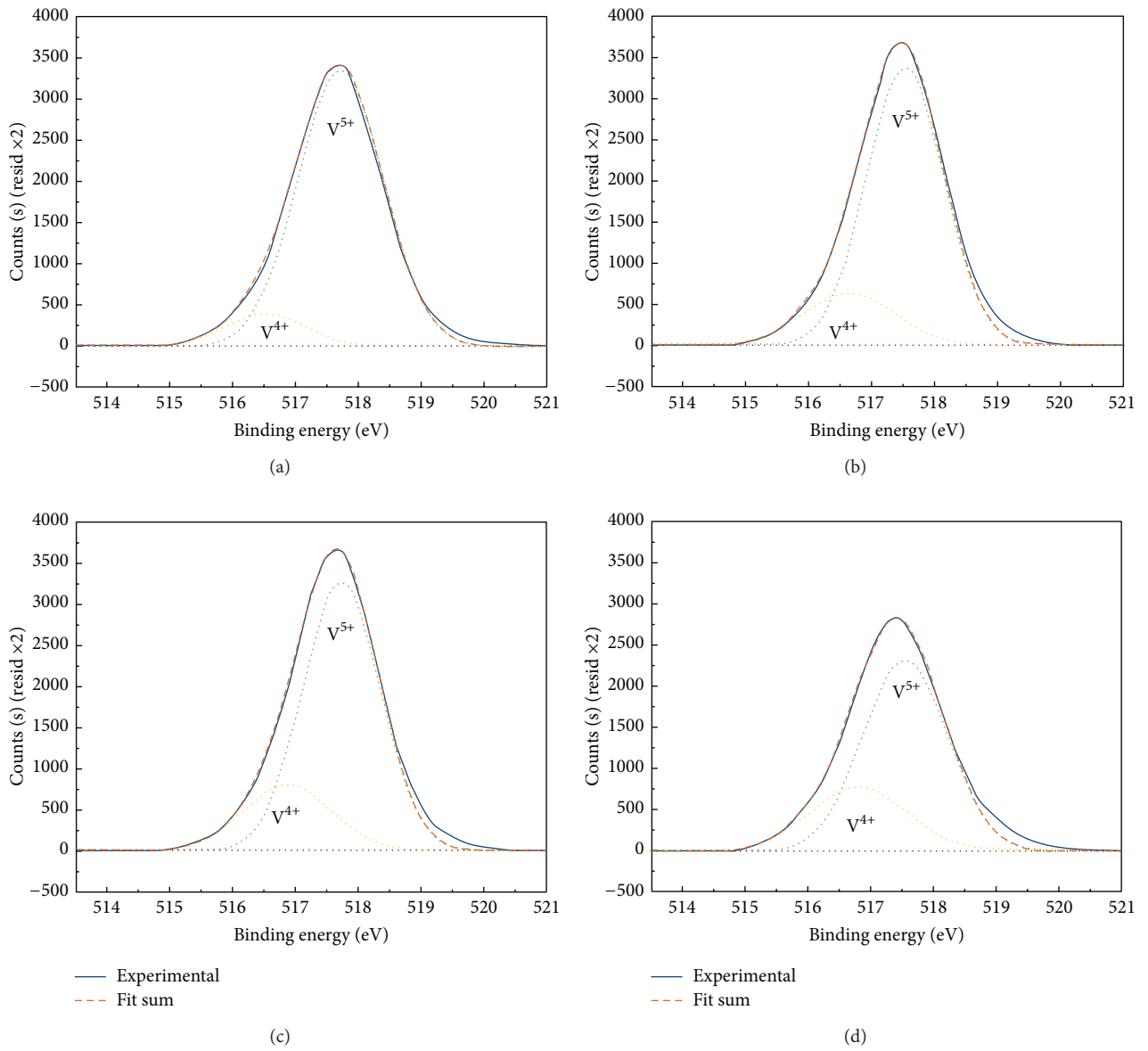


FIGURE 5: V $2p_{3/2}$ core level spectra fitted with a single peak of V^{5+} and V^{4+} for glasses (a) annealed at 225°C and heated for crystallization at 275°C for (b) 1, (c) 3, and (d) 5 h.

TABLE 1: Peak positions, areas, and relative concentrations of V^{4+} and V^{5+} resulting from the curve fittings of the V 2p spectra of the $75V_2O_5-15B_2O_3-10P_2O_5$ glasses heat-treated at 275°C .

Heating process	Peak BE	Height counts	FWHM (eV)	Area	$[V^{5+}]/[V_{\text{total}}]$	$[V^{4+}]/[V_{\text{total}}]$
Annealed	517.71	3353.98	1.60	5705.38	0.9033	0.0967
	516.52	390.71	1.47	611.07		
$275^{\circ}\text{C}/1\text{h}$	517.53	3374.83	1.45	5214.94	0.8202	0.1798
	516.64	632.89	1.70	1143.24		
$275^{\circ}\text{C}/3\text{h}$	517.74	3275.23	1.45	5052.32	0.7823	0.2177
	516.88	802.80	1.65	1406.09		
$275^{\circ}\text{C}/5\text{h}$	517.54	2328.67	1.58	3919.33	0.7230	0.2770
	516.80	779.33	1.81	1501.61		

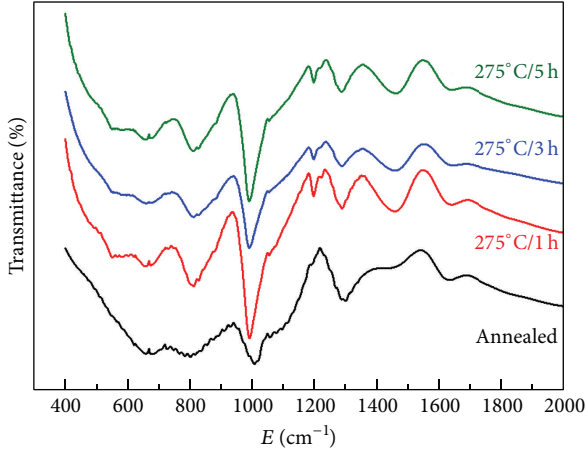


FIGURE 6: Infrared spectra of $75\text{V}_2\text{O}_5\text{-}15\text{B}_2\text{O}_3\text{-}10\text{P}_2\text{O}_5$ glass heat-treated at 275°C .

BO_3 units. The second group of bands, located at $800\text{--}1200\text{ cm}^{-1}$, could be ascribed to the B-O bond stretching in the tetrahedral BO_4 units. A third group of absorption bands was observed at around 600 cm^{-1} , which can be attributed to the bending of O-B-O linkages in the borate network [18, 19].

The absence of a peak at 809 cm^{-1} indicates that no boroxol ring was formed [20], which suggests that the glass system under investigation consists of randomly connected BO_3 and BO_4 groups. The absorption peaks at 1195 and 1465 cm^{-1} are related to the fundamental asymmetrical stretching vibration of the B-O bond in the trigonal BO_3 units [21, 22]. Mitigation of the slope of the absorption band indicated that B-O bond stretching in the trigonal BO_3 units occurred during heat treatment at 275°C . In addition, the absorption peak intensity at 1468 cm^{-1} (BO_3 structure) shifted to lower wave numbers ($1468\text{--}1430\text{ cm}^{-1}$) as the heat treatment was significantly reduced. The stretching vibration of the B-O bond in the tetrahedral BO_4 units appeared at $1050\text{--}900\text{ cm}^{-1}$. The absorption peak at 1019 cm^{-1} , attributed to the B-O bond stretching vibration in the tetrahedral BO_4 units, shifted to higher wave numbers ($1019\text{--}1020\text{ cm}^{-1}$) upon heat treatment at 275°C [17, 23].

From the FTIR analysis, shift of the vibrational band indicated that nanocrystallization at 275°C with increasing durations of heat treatment strengthened the BO_4 unit structure and weakened the BO_3 unit structure. This fact, coupled with the XRD analysis results, allowed us to examine the $\text{BO}_3 + \text{VO}_5(\text{V}_2\text{O}_5) \rightarrow \text{BO}_4 + \text{VO}_4(\text{VO}_2)$ structural change that occurred in the glass. This structural change affects the electrical conduction and catalytic properties of the vanadate glass.

3.4. Electrical Conductivity. The changes in the electrical conductivity of the heat-treated specimens are shown in Table 2. Electrical conductivity was increased by heat-treating the samples at 275°C and increasing the duration of the heat treatment.

The resulting conductivity value of $1.42003 \times 10^{-7}\ \Omega^{-1}$ obtained by heat treatment at 275°C for 1 h was approximately

TABLE 2: Electrical conductivity of $75\text{V}_2\text{O}_5\text{-}15\text{B}_2\text{O}_3\text{-}10\text{P}_2\text{O}_5$ glasses heat-treated at 275°C .

Heating process	Electric resistance	Electrical conductivity
Annealed	35857142.86	$0.278884E - 07$
$275^\circ\text{C}/1\text{ h}$	7042105.263	$1.42003E - 07$
$275^\circ\text{C}/3\text{ h}$	1765000	$5.66572E - 07$
$275^\circ\text{C}/5\text{ h}$	1330769.231	$7.51445E - 07$

5.1 times greater than the conductivity of the annealed glass. Furthermore, the resulting value of $7.51445 \times 10^{-7}\ \Omega^{-1}$ obtained by heat treatment at 275°C for 5 h was approximately 26.9 times greater than the conductivity of annealed glass.

Combining result of the electrical conductivity with those of the XRD and XPS analyses, it was hypothesized that the change in the electrical properties was because of the changes in the VO_5 and VO_4 structures caused by the change in the coordination number, which was due to the nanocrystallization. Electrical conductivity of this glass system is related to the metal ion value ratio C, which for vanadium-containing oxide glasses is defined as $= [\text{V}^{4+}]/([\text{V}^{4+}][\text{V}^{5+}]$. According to Morinaga and Fujino [24], the electrical conductivity of vanadate glasses increases as C approaches 0.5. Heat-treating the $75\text{V}_2\text{O}_5\text{-}15\text{B}_2\text{O}_3\text{-}10\text{P}_2\text{O}_5$ glass at 275°C nanocrystallizes and strengthens the VO_2 phase while reducing the V_2O_5 phase. This indicates that the V^{5+} ions changed to V^{4+} as values of C approached 0.5. From these inferences, it can be predicted that this behavior leads to an increase in the electrical conductivity and that increasing the conduction path length, number of electronic transfer ports, and the VO_2 nanocrystalline phase contribute to this increased conductivity.

3.5. Catalytic Property. TGA results of two samples containing 20 mg of glass powder nanocrystallized at each heat treatment condition mixed with 20 mg of stearic acid or linoleic acid are shown in Figure 7 and Table 3. Linoleic acid ($\text{CH}_3(\text{CH}_2)_4\text{CH}=\text{CHCH}_2\text{CH}=\text{CH}(\text{CH}_2)_7\text{CO}_2\text{H}$) is a typical unsaturated fatty acid with two double bonds, and stearic acid ($\text{CH}_3(\text{CH}_2)_{16}\text{COOH}$) is a typical saturated higher fatty acid with a carbon number of 18. Weight loss occurs when each fatty acid was partially converted to CO_2 gas by an oxidation reaction.

The finish temperature of weight loss, which is the temperature at which the oxidation reaction of linoleic acid and stearic acid is complete, associated with the conversion of the acid to CO_2 gas caused by crystallization due to 1 h heat treatment at 275°C , shifted to lower temperatures (356.05 to 324.15°C for linoleic acid and 378.67 to 341.75°C for stearic acid). Subsequently, the finish temperature of weight loss increases gradually by increasing the heat treatment duration. The finish temperature of samples heat-treated for 5 h was 340.96°C and 362.16°C for linoleic and stearic acids, respectively.

GC-MSD results of a sample containing 2 mg glass powder nanocrystallized at each heat treatment condition mixed with 8 mg of carbon are shown in Figure 8. Carbon

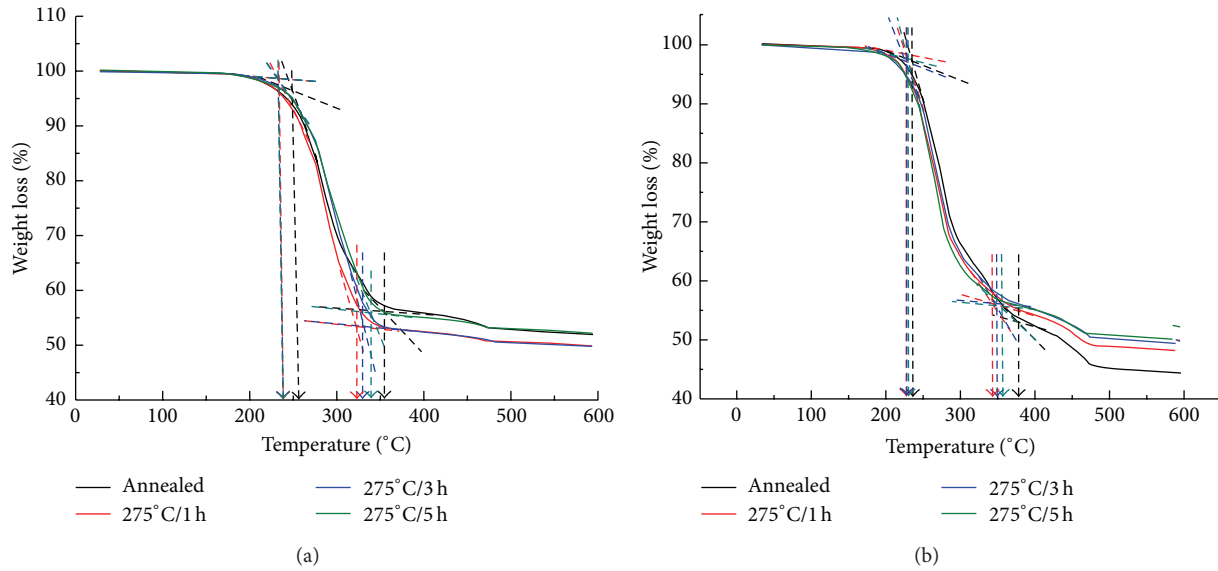


FIGURE 7: Weight loss of (a) linoleic and (b) stearic acids with $75\text{V}_2\text{O}_5\text{-}15\text{B}_2\text{O}_3\text{-}10\text{P}_2\text{O}_5$ glass heat-treated at 275°C .

TABLE 3: Weight loss of linoleic and stearic acids with $75\text{V}_2\text{O}_5\text{-}15\text{B}_2\text{O}_3\text{-}10\text{P}_2\text{O}_5$ glass heat-treated at 275°C .

Heating process	Linoleic acid		Stearic acid	
	Start temp. of weight loss	Finish temp. of weight loss	Start temp. of weight loss	Finish temp. of weight loss
Annealed	254.19	356.05	235.56	378.67
$275^\circ\text{C}/1\text{h}$	245.24	324.15	233.23	341.75
$275^\circ\text{C}/3\text{h}$	244.02	330.92	233.55	350.02
$275^\circ\text{C}/5\text{h}$	244.23	340.96	233.62	362.16

converted into CO_2 gas by an oxidation reaction, and hence, the desorption intensity of CO_2 gas increases.

The sudden increase point of the desorption intensity, which is the temperature at which the oxidation reaction of carbon is complete, associated with the conversion of the carbon to CO_2 gas because of nanocrystallization after 1 h heat treatment at 275°C , shifted from 395.13°C to 281.25°C (Table 4). Thereafter, the sudden increase point of the desorption intensity gradually decreased by increasing the heat treatment duration. The sudden increase point after 5 h of heat treatment was 387.98°C .

Prior research results have shown that the V^{5+} to V^{4+} reduction reaction causes a catalytic effect in the oxidation reaction of reactants (linoleic and stearic acids and carbon), and the XRD, XPS, and FTIR analyses of the structural changes due to the glass nanocrystallization lead to the following conclusion. We hypothesize that, by nanocrystallizing a given composition of glass at 275°C , nanocrystal phases are produced and the glass structure is changed to a relatively more closed structure (see Section 3.6). It was determined that the tunneling effect, which is the electron transfer mechanism in the vanadate glass structure, becomes more active. However, as the heat treatment time became progressively longer, the catalytic effect diminished in strength. By increasing the heat treatment time, the relative amount

TABLE 4: Sudden increase point of the desorption intensity of CO_2 gas from carbon with $75\text{V}_2\text{O}_5\text{-}15\text{B}_2\text{O}_3\text{-}10\text{P}_2\text{O}_5$ glass heat-treated at 275°C .

Heating process	Sudden increase point of the desorption ($^\circ\text{C}$)
Annealed	395.15
$275^\circ\text{C}/1\text{h}$	281.25
$275^\circ\text{C}/3\text{h}$	376.24
$275^\circ\text{C}/5\text{h}$	388.98

of the VO_2 phase increased while that of VO_5 decreased, changing the vanadium ion valency from V^{5+} to V^{4+} . Thus, the V^{5+} activity and the reduction reaction of V^{4+} decrease gradually, weakening the catalytic property. Therefore, glass nanocrystallization due to heat treatment creates a denser structure than annealed glass. This causes the V^{5+} to V^{4+} reduction reaction and catalytic action of the oxidation of fatty acid to become active. On the other hand, as the heat treatment time increased, the reduction reaction decreased, indicating that the catalytic effects declined gradually.

3.6. Other Properties. We examined the density and molar volume to obtain indirect evidence of the structural changes and the associated catalytic properties described above.

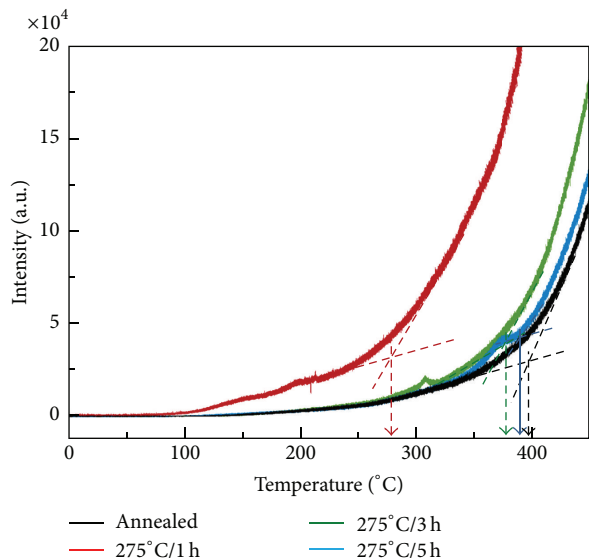


FIGURE 8: Desorption intensity of CO₂ gas from carbon conversion with 75V₂O₅-15B₂O₃-10P₂O₅ glass heat-treated at 275°C.

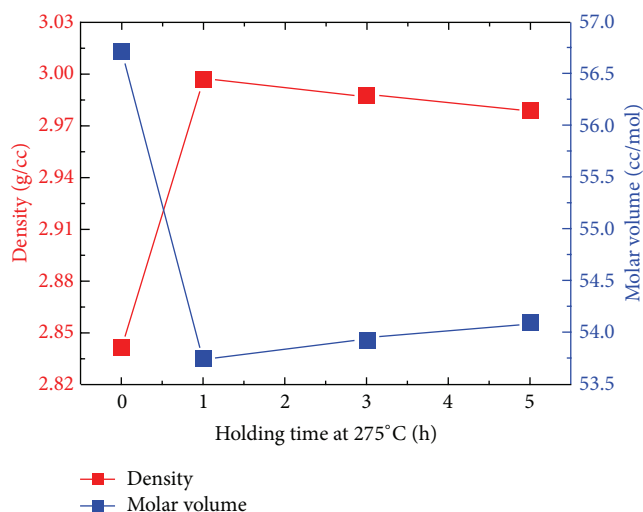


FIGURE 9: Density and molar volume of 75V₂O₅-15B₂O₃-15P₂O₅ glasses heat-treated at 275°C.

Looking at the changes in density and molar volume of 75V₂O₅-15B₂O₃-10P₂O₅ glasses shown in Figure 9, we observe that the density greatly increased and the molar volume greatly decreased after heat treatment at 275°C. On the other hand, when the heat treatment duration was increased, the density slightly decreased and the molar volume slightly increased.

The results from Figure 9 provide indirect evidence that describes the changes in the catalytic properties. When the glass is nanocrystallized by heat treatment, its structural density is much higher compared to the annealed glass, which leads to the enhanced catalytic activity. Increasing the heat treatment duration then leads to weaker catalytic activity because the structure gradually becomes less dense.

4. Conclusions

The purpose of this study was to examine and verify the correlation between the changes in the catalytic and electrical properties and the structure due to the nanocrystallization of 75V₂O₅-15B₂O₃-10P₂O₅ glass containing a mix of V⁵⁺, V⁴⁺, BO₄, and BO₃. Using various equipment of structural analysis, we confirmed the BO₃ + VO₅(V₂O₅) → BO₄ + VO₄(VO₂) change in structure by nanocrystallizing and increasing the duration of heat treatment.

The changes in the catalytic properties and electrical conductivity were due to the nanocrystal structure and the state of the vanadium ions. The heat treatment used for nanocrystallization caused the electrical conductivity to increase continually; this is because the ion ratio, C value, approaches 0.5 owing to the transition of V⁵⁺ to V⁴⁺. On the other hand, after being improved for the purpose of nanocrystallization, the catalytic effect decreased as the duration of heat treatment increased. This is because, during nanocrystallization, the glass structure is dense and the tunneling effect occurs more actively. This behavior accelerates the reaction responsible for the catalytic activity. However, by increasing the duration of heat treatment, the vanadium ion valency changes from V⁵⁺ to V⁴⁺, and the activity of V⁵⁺ decreases; that is, the reduction reaction site of V⁴⁺ decreases gradually, causing the catalytic property to weaken. In addition, we indirectly and quantitatively confirmed the structural change through the increase in density and the decrease in molar volume due to nanocrystallization and the decrease in density and the increase in molar volume due to increasing the duration of heat treatment.

Conflict of Interests

The authors declare that there is no conflict of interests regarding the publication of this paper.

References

- [1] L. Murawski, C. H. Chung, and J. D. Mackenzie, "Electrical properties of semiconducting oxide glasses," *Journal of Non-Crystalline Solids*, vol. 32, no. 1-3, pp. 91-104, 1979.
- [2] G. Calestani, L. Marghignani, A. Montenero, and M. Bettinelli, "DC conductivity of ZnOV₂O₅ glasses," *Journal of Non-Crystalline Solids*, vol. 86, no. 3, pp. 285-292, 1986.
- [3] Y. Kawamoto, M. Fukuzuka, Y. Ohta, and M. Imai, "Electronic conduction and glass structure in V₂O₅-BaO-K₂O-ZnO glasses," *Physics and Chemistry of Glasses*, vol. 20, p. 199, 1979.
- [4] A. M. Nassar, P. A. Moustafa, and M. A. Salem, "Electrical properties of some vanadate semiconducting glasses," *Indian Journal of Pure and Applied Physics*, vol. 20, no. 5, pp. 337-340, 1982.
- [5] C. H. Chung and J. D. Mackenzie, "Electrical properties of binary semiconducting oxide glasses containing 55 mole % V₂O₅," *Journal of Non-Crystalline Solids*, vol. 42, no. 1-3, pp. 357-370, 1980.
- [6] K. S. Han, C. W. Hwang, D. H. Kim et al., "Effects of substituting B₂O₃ for P₂O₅ on the structures and properties of V₂O₅-P₂O₅

- glass systems," *Electronic Materials Letters*, vol. 8, no. 6, pp. 655–658, 2012.
- [7] L. Chen, B. Yang, X. Zhang, W. Dong, and K. Cao, "Methane oxidation over a V_2O_5 catalyst in the liquid phase," *Energy and Fuels*, vol. 20, no. 3, pp. 915–918, 2006.
- [8] D. G. Gwoo, T. H. Kim, K. S. Han, W. G. Choi, J. H. Kim, and B. K. Ryu, "Electrical properties of crystallized 30B2O3-70V2O5 glass," *Electronic Materials Letters*, vol. 9, no. 3, pp. 309–313, 2013.
- [9] N. J. Kim, S. H. Im, D. H. Kim, D. K. Yoon, and B. K. Ryu, "Structure and properties of borophosphate glasses," *Electronic Materials Letters*, vol. 6, no. 3, pp. 103–106, 2010.
- [10] G. D. Khattak, A. Mekki, and M. A. Gondal, "XPS studies of pulsed laser induced surface modification of vanadium phosphate glass samples," *Journal of Physics and Chemistry of Solids*, vol. 74, no. 1, pp. 13–17, 2013.
- [11] G. D. Khattak, A. Mekki, and L. E. Wenger, "X-ray photoelectron spectroscopy (XPS) and magnetic susceptibility studies of vanadium phosphate glasses," *Journal of Non-Crystalline Solids*, vol. 355, no. 43-44, pp. 2148–2155, 2009.
- [12] M. Demeter, M. Neumann, and W. Reichelt, "Mixed-valence vanadium oxides studied by XPS," *Surface Science*, vol. 454–456, no. 1, pp. 41–44, 2000.
- [13] Y. Chen, K. Xie, and Z. Liu, "XPS studies of V_2O_5 thin film at different temperatures and oxygen partial pressures," *Applied Surface Science*, vol. 126, no. 3-4, pp. 347–351, 1998.
- [14] J. Mendialdua, R. Casanova, and Y. Barbaux, "XPS studies of V_2O_5 , V_6O_{13} , VO_2 and V_2O_3 ," *Journal of Electron Spectroscopy and Related Phenomena*, vol. 71, no. 3, pp. 249–261, 1995.
- [15] A. Mekkia, G. D. Khattaka, and L. E. Wengerb, "XPS and magnetic studies of vanadium tellurite glasses," *Journal of Electron Spectroscopy and Related Phenomena*, vol. 175, no. 1-3, pp. 21–26, 2009.
- [16] E. I. Kamitsos, M. A. Karakassides, and G. D. Chryssikos, "Vibrational spectra of magnesium-sodium-borate glasses. 2. Raman and mid-infrared investigation of the network structure," *Journal of Physical Chemistry*, vol. 91, no. 5, pp. 1073–1079, 1987.
- [17] S. G. Motke, S. P. Yawale, and S. S. Yawale, "Infrared spectra of zinc doped lead borate glasses," *Bulletin of Materials Science*, vol. 25, no. 1, pp. 75–78, 2002.
- [18] B. K. Sharma, D. C. Dube, and A. Mansingh, "Preparation and characterisation of V_2O_5 - B_2O_3 glasses," *Journal of Non-Crystalline Solids*, vol. 65, no. 1, pp. 39–51, 1984.
- [19] A. Abd-El-Moneim, "DTA and IR absorption spectra of vanadium tellurite glasses," *Materials Chemistry and Physics*, vol. 73, no. 2-3, pp. 318–322, 2002.
- [20] A. A. Alemi, H. Sedghi, A. R. Mirmohseni, and V. Golsanamlu, "Synthesis and characterization of cadmium doped lead-borate glasses," *Bulletin of Materials Science*, vol. 29, no. 1, pp. 55–58, 2006.
- [21] Y. D. Yiannopoulos, G. D. Chryssikos, and E. I. Kamitsos, "Structure and properties of alkaline earth borate glasses," *Physics and Chemistry of Glasses*, vol. 42, no. 3, pp. 164–172, 2001.
- [22] E. E. Horopanitis, G. Perentzis, A. Beck, L. Guzzi, G. Peto, and L. Papadimitriou, "Correlation between structural and electrical properties of heavily lithiated boron oxide solid electrolytes," *Journal of Non-Crystalline Solids*, vol. 354, no. 2–9, pp. 374–379, 2008.
- [23] A. Makishima and J. D. Mackenzie, "Calculation of bulk modulus, shear modulus and Poisson's ratio of glass," *Journal of Non-Crystalline Solids*, vol. 17, no. 2, pp. 147–157, 1975.
- [24] K. Morinaga and S. Fujino, "Preparation and properties of $SnO-SnCl_2-P_2O_5$ glass," *Journal of Non-Crystalline Solids*, vol. 282, no. 1, pp. 118–124, 2001.

Research Article

Nanoscale Ferroelectric Switchable Polarization and Leakage Current Behavior in $(\text{Ba}_{0.50}\text{Sr}_{0.50})(\text{Ti}_{0.80}\text{Sn}_{0.20})\text{O}_3$ Thin Films Prepared Using Chemical Solution Deposition

Venkata Sreenivas Puli,^{1,2,3} Shiva Adireddy,¹ Dhiren K. Pradhan,²
Ram S. Katiyar,² and Douglas B. Chrisey¹

¹Department of Physics and Engineering Physics, Tulane University, New Orleans, LA 70118, USA

²Department of Physics, University of Puerto Rico, San Juan, PR 00936, USA

³Department of Mechanical Engineering, University of Texas, El Paso, TX 79968, USA

Correspondence should be addressed to Venkata Sreenivas Puli; pvsril23@gmail.com

Received 19 March 2015; Accepted 20 April 2015

Academic Editor: Hassan Karimi-Maleh

Copyright © 2015 Venkata Sreenivas Puli et al. This is an open access article distributed under the Creative Commons Attribution License, which permits unrestricted use, distribution, and reproduction in any medium, provided the original work is properly cited.

Nanoscale switchable ferroelectric $(\text{Ba}_{0.50}\text{Sr}_{0.50})(\text{Ti}_{0.80}\text{Sn}_{0.20})\text{O}_3$ -BSTS polycrystalline thin films with a perovskite structure were prepared on Pt/TiO_x/SiO₂/Si substrate by chemical solution deposition. X-ray diffraction (XRD) spectra indicate that a cubic perovskite crystalline structure and Raman spectra revealed that a tetragonal perovskite crystalline structure is present in the thin films. Sr²⁺ and Sn⁴⁺ cosubstituted film exhibited the lowest leakage current density. Piezoresponse Force Microscopy (PFM) technique has been employed to acquire out-of-plane (OPP) piezoresponse images and local piezoelectric hysteresis loop in polycrystalline BSTS films. PFM phase and amplitude images reveal nanoscale ferroelectric switching behavior at room temperature. Square patterns with dark and bright contrasts were written by local poling and reversible nature of the piezoresponse behavior was established. Local piezoelectric butterfly amplitude and phase hysteresis loops display ferroelectric nature at nanoscale level. The significance of this paper is to present ferroelectric/piezoelectric nature in present BSTS films at nanoscale level and corroborating ferroelectric behavior by utilizing Raman spectroscopy. Thus, further optimizing physical and electrical properties, BSTS films might be useful for practical applications which include nonvolatile ferroelectric memories, data-storage media, piezoelectric actuators, and electric energy storage capacitors.

1. Introduction

Perovskite oxide materials are the most studied functional materials for ferroelectric, ferromagnetic, magnetoresistive, and memristive applications. BaTiO₃ and its solid solutions are attractive candidate materials for multifunctional applications. These ferroelectric ceramics and thin films are key materials for nonvolatile ferroelectric random access memories (FE-RAMs) and volatile dynamic random access memories (DRAMs), capacitors, and various other applications [1, 2]. By suitable site engineering (chemical doping/substitution) with either isovalent or aliovalent elements at Ba²⁺ or/and Ti⁴⁺ site in BaTiO₃ (BTO) leads to changes in

the structure with improved electrical properties, the magnitude of dielectric constant, ferroelectric to paraelectric phase transition temperature, and dielectric tunable properties in the wide range of temperature to meet the variety of device applications.

Various BTO based solid solutions have attracted considerable attention due to their remarkable dielectric, ferroelectric, piezoelectric, pyroelectric, and optical properties which are suitable for high energy storage capacitors and multilayer ceramic capacitor (MLCC) applications and they have been extensively studied for improved electrical properties, which include Ba(Ti,Sn)O₃ [3], (Ba,Sr)(Ti,Sn)O₃ [4], Ba(Zr,Ti)O₃ [5], (Ba,Ca)TiO₃ [5–7],

$\text{Ba}(\text{Ti}, \text{Sn})\text{O}_3-x(\text{Ba}, \text{Ca})\text{TiO}_3$ [8], $(1-x)\text{Ba}(\text{Zr}_{0.2}\text{Ti}_{0.8})\text{O}_3-x(\text{Ba}_{0.7}\text{Ca}_{0.3})\text{TiO}_3$ [9–13], $(\text{Ba}_{1-x}\text{Ca}_x)(\text{Ti}_{0.92}\text{Sn}_{0.08})\text{O}_3$ [14], and $(1-x)(\text{Ba}, \text{Ca})(\text{Ti}, \text{Sn})\text{O}_3-x(\text{Ba}, \text{Ca})(\text{Ti}, \text{Zr})\text{O}_3$ [15]. Shift in the Curie temperature to lower temperature to that of pure BTO ($T_c \sim 120\text{--}130^\circ\text{C}$) is often observed when isovalent ions are doped (e.g., Sr^{2+} doping for Ba^{2+} site or Zr^{4+} doping for Ti^{4+} site) in BTO lattice [16]. Improved electrical properties were also observed for Ca substituted BTO, with a modest increase in T_c [5]. By varying wt.% of Sn^{4+} in $(\text{Ba}_{0.95}\text{Ca}_{0.05})(\text{Ti}_{1-x}\text{Sn}_x)\text{O}_3(\text{BCTS}_x)$ ceramics, a series of phase transitions were evolved which include inceptive orthorhombic phase (O) at $0 \leq x \leq 0.04$ to a two-phase coexistence of pseudocubic-orthorhombic phase (PC-O) at $0.06 \leq x \leq 0.10$ and further to a multiphase coexistence of rhombohedral-pseudocubic-orthorhombic phase (R-PC-O) at $x = 0.11$ with an ultrahigh piezoelectric response ($d_{33} \sim 670$ pC/N, $dS/dE \sim 1214$ pm/V) at room temperature [8]. Similar phase transition behavior was observed for Er-doped BiFeO_3 films, with enhanced electrical properties such as ferroelectric and leakage properties derived from the phase transition of rhombohedral to tetragonal and orthorhombic symmetry structure as Er-doped concentration (x) increased gradually to 0.15 then to the orthorhombic structure when $x = 0.20$ [17]. By varying Sr^{2+} content at Ba^{2+} site in $(\text{Ba}_{0.91}\text{Ca}_{0.09-x}\text{Sr}_x)(\text{Ti}_{0.92}\text{Sn}_{0.08})\text{O}_3$ ceramics, the phase transition of rhombohedral-orthorhombic and orthorhombic-tetragonal merged to near room temperature and outstanding electrical properties were obtained at room temperature due to phase coexistence (orthorhombic and tetragonal) [18].

Particularly, ferroelectric barium strontium titanate $[\text{Ba}_{1-x}\text{Sr}_x\text{TiO}_3\text{-(BST)}]$ ($0 \leq x \leq 1$) ceramics and thin films are promising for capacitor applications due to their low leakage current at operable voltages, large breakdown voltage, and high dielectric constant with low dielectric loss [19]. Various compositions of BST thin films were well studied for tunable microwave device applications such as phase shifters, delay lines, tunable filters, and voltage controlled oscillators due to high dielectric constant and tunability (change in the dielectric constant under an applied electric field) and good temperature stability [20, 21].

Barium tin titanate $[\text{Ba}(\text{Ti}_{1-x}\text{Sn}_x)\text{O}_3\text{-(BTS)}]$ also received much research attention because of its high dielectric constant and relaxor ferroelectric characteristics and these are good candidate materials for applications in microelectronic devices [22–24]. Ferroelectric-paraelectric phase transition temperature decreased with increasing Sn^{4+} concentration in $\text{Ba}(\text{Ti}_{0.85}\text{Sn}_{0.15})\text{O}_3$, with more diffused phase transition behavior [25]. BTS solid solutions have a ferroelectric phase transition between 0° and 130°C , when the Sn^{4+} ratio is between $x = 0$ and 0.20 and these solid solutions exhibit stable ferroelectric properties with a Curie temperature around room temperature at $x = 0.1$ to 0.15 [26, 27]. However to further improve the reproducibility and stability with improved physical and electrical properties of these materials, codoping/substitution at both Ba^{2+} and Ti^{4+} site in BTO lattice is essential and various research groups around the globe are working in this direction. Wang et al. [28]

reported $(\text{Ba}_{1-x}\text{Sr}_x)(\text{Ti}_{0.9}\text{Sn}_{0.1})\text{O}_3$ ($0 \leq x \leq 0.3$ -BS_xTS) thin films prepared by radio frequency magnetron sputtering with a large ferroelectric hysteresis behavior and low leakage current behavior at 25°C . Souza et al. [4] reported BSTS nanopowder synthesis using soft chemical method and pseudocubic crystallographic structure was obtained for these powders. They also reported dielectric and ferroelectric properties for BSTS polycrystalline pseudocubic thin films prepared using soft chemical method [29]. Further, it was noticed that only few reports exist in literature about the local piezoelectric properties measurement on BST [30, 31] and BSTS ceramics [32] at nanoscale level. In general, nanoscale science (nanoscience) and nanotechnology best describe the materials' properties at nanometer length scale, which is one billionth (10^{-9}) of a meter. Materials' properties at nanoscale level behave differently from that of micron sized materials. Improved properties at nanoscale architecture are due to altered atomic configurations and increased surface area to volume ratio. Both nanoscience and nanotechnology are interdisciplinary and have vast variety of applications in scientific, industrial, and biological fields. However, to the best of our knowledge, nanoscale ferroelectric switchable polarization studies have not been performed in complete so far on the BSTS system by utilizing piezoresponse force microscopy (PFM) technique. Therefore, the present study focuses on the ferroelectric switching behavior at nanoscale level by utilizing PFM studies along with other bulk properties including X-ray diffraction \sim XRD, Raman spectroscopy, and leakage current (current density-voltage) behavior of the BSTS films deposited on Pt/TiO_x/SiO₂/Si substrates by chemical solution deposition (spin coating). Temperature and electric field dependent dielectric properties, micro Raman, and ferroelectric polarization measurements on this film are in progress and will be reported elsewhere.

2. Experimental Details

Stoichiometric $(\text{Ba}_{0.50}\text{Sr}_{0.50})(\text{Ti}_{0.80}\text{Sn}_{0.20})\text{O}_3$ -BSTS used in this study was prepared using chemical solution deposition as outlined in Figure 1. Barium acetate ($\text{Ba}(\text{C}_2\text{H}_3\text{O}_2)_2$, Aldrich), strontium acetate ($\text{Sr}(\text{CH}_3\text{CO}_2)_2$, Aldrich), tin acetate ($\text{Sn}(\text{CH}_3\text{CO}_2)_2$, Aldrich), and titanium (IV) butoxide ($\text{Ti}(\text{OCH}_2\text{CH}_2\text{CH}_2\text{CH}_3)_4$, Aldrich) were used as precursors. 2-Methoxy ethanol ($\text{CH}_3\text{OCH}_2\text{CH}_2\text{OH}$, 99.8%, Aldrich) was used as a solvent to facilitate the dehydration by boiling as it boils at 125°C and Acetic acid (CH_3COOH , 99.99% Aldrich) was used as the chelating agent for the alkoxides. Stock solution was directly deposited onto Pt/TiO_x/SiO₂/Si substrates by spin coating (precoating 1000 rpm 10 s followed by 3000 rpm for 30 s). Resultant films underwent two different preannealing (pyrolysis) heat treatments. In the first step, films were heat-treated at 250°C for 2 min. These steps were repeated for obtaining desired thickness, and finally in the second step the films were annealed at 750°C temperature for obtaining crystalline dense BSTS films. Flow chart of the preparation of BSTS thin film by chemical solution deposition process is shown in Figure 1.

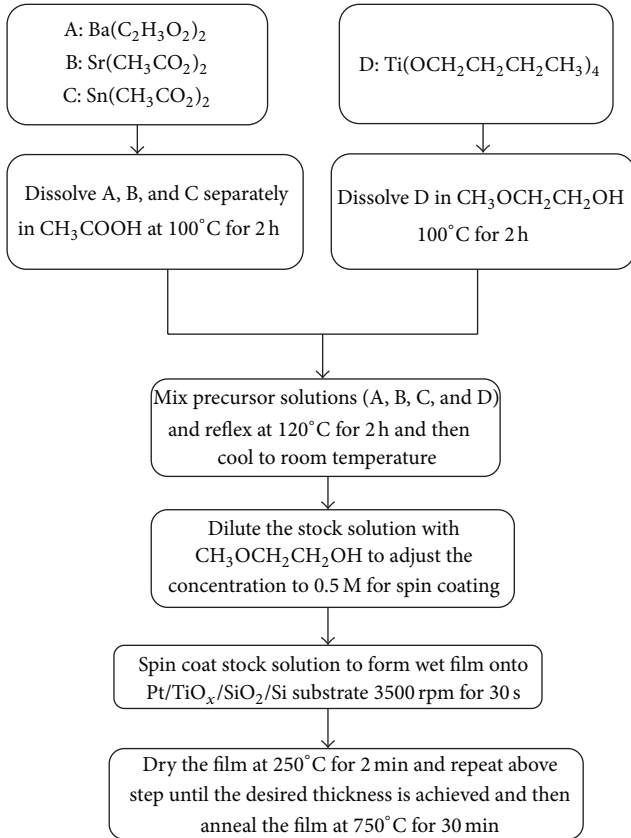


FIGURE 1: Flow chart of the preparation of $(\text{Ba}_{0.50}\text{Sr}_{0.50})(\text{Sn}_{0.20}\text{Ti}_{0.80})\text{O}_3$ -BSTS thin film by chemical solution deposition process.

The crystal structure of BSTS films was characterized using an X-ray diffractometer (Rigaku) employing the Bragg-Brentano (θ - 2θ) method with Cu $K\alpha$ ($\lambda = 1.5418 \text{ \AA}$) as the radiation source. Room temperature Raman spectroscopy measurements were performed using SA T64000 spectrograph consisting of a double monochromator coupled to the third stage with $1800 \text{ grooves mm}^{-1}$ grating. Radiation $\sim 514.532 \text{ nm}$ from a Coherent Innova 99 argon ion laser was focused over a less than 2 mm diameter circle area by using a Raman microprobe with an $80\times$ objective. Thickness of the BSTS films was determined independently using an Ambios XP-200 profilometer and a spectral reflectance based Filmetrics instrument which was around 360 nm .

Platinum (Pt) dots were sputtered to form the top electrode ($250 \mu\text{m}$) by utilizing a shadow mask by means of direct current (DC) magnetron sputtering. Electrical properties were measured on thin films grown on Pt (top electrode) and Pt/TiO_x/SiO₂/Si (bottom electrode) substrate in metal-insulator-metal (M-I-M) configuration. Leakage current measurements were done under vacuum (10^{-4} torr) with Keithley electrometer (model 6517A). And nanoscale ferroelectric switching behavior of the films was measured by a Veeco piezoresponse force microscope (PFM) operated in contact mode and local piezoelectric hysteresis loops were

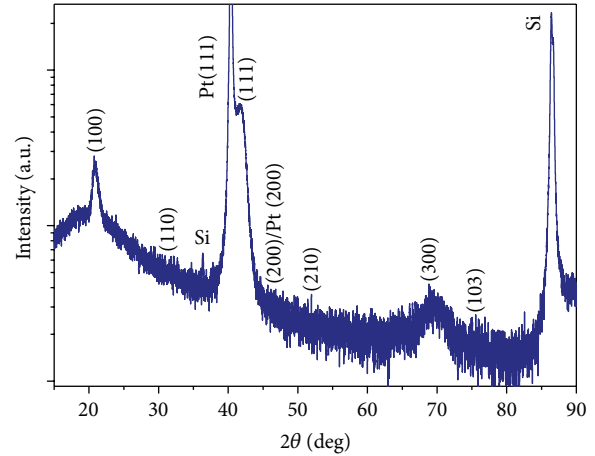


FIGURE 2: XRD patterns with 2θ - θ scans of $(\text{Ba}_{0.50}\text{Sr}_{0.50})(\text{Sn}_{0.20}\text{Ti}_{0.80})\text{O}_3$ -BSTS thin film.

obtained without top electrode (whereas tip itself acts as top electrode in these measurements).

3. Results and Discussion

XRD profiles of BSTS film samples are measured at room temperature. The XRD patterns indicate that BSTS has a perovskite crystalline structure as shown in Figure 2, which is also demonstrated by the Raman spectroscopic measurements. However from the XRD patterns it is not clear what the exact phase at room temperature is and we cannot obtain detailed information about the structure of the films. Hence we made room temperature Raman spectroscopic measurements to obtain the information on the crystal structure of the BSTS films from vibrational spectroscopy.

A close relationship between lattice dynamics and ferroelectricity is obtained using Raman spectroscopy. Crystalline phase is confirmed using Raman spectra. There are fifteen degrees of freedom in ABO_3 perovskite materials above the cubic-tetragonal phase transition, which are divisible into $4F_{1u} + 1F_{2u}$ [33]. However, one of the F_{1u} symmetry modes corresponds to the acoustic branch and the remaining $3F_{1u}$ and $1F_{2u}$ belong to the optical branches in the cubic phase with O_h^1 or $Pm3m$ point group symmetry [33]. In paraelectric cubic phase in ABO_3 perovskites there are 12 optical modes, which transform into the triply degenerate irreducible representations of the O_h^1 point group ($\Gamma_{\text{cub}} = 3F_{1u} + 1F_{2u}$) [33]. In cubic perovskite phase, the F_{1u} modes are IR active and the F_{2u} mode is neither IR nor Raman active, the so-called "silent mode", whereas in the ferroelectric tetragonal phase each triply degenerate F_{1u} mode splits into $A_1 + E$ modes, while the F_{2u} silent mode splits into $B_1 + E$ modes. These Raman modes include $3 A_1(\text{TO}) + 3 A_1(\text{LO}) + 3 E(\text{TO}) + 3 E(\text{LO}) + 1 E(\text{LO} + \text{TO}) + 1 B_1$ [34]. However, all the A_1 and E modes are both Raman and IR active, whereas B_1 mode is only Raman active. The high temperature cubic-phase Raman optical modes (A_1 and E) are further split into longitudinal optical (LO) and transverse optical (TO) branches due to

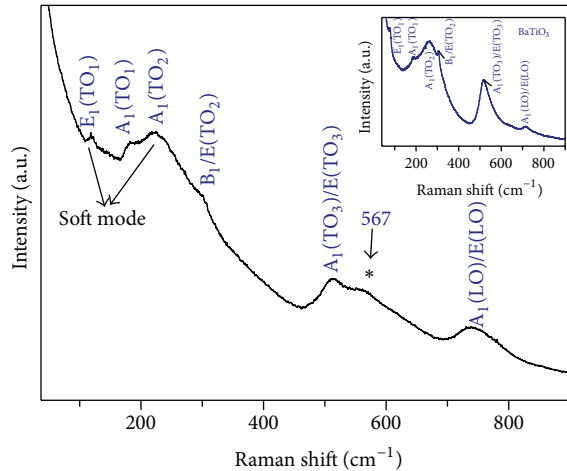


FIGURE 3: Raman spectroscopic images of $(\text{Ba}_{0.50}\text{Sr}_{0.50})(\text{Sn}_{0.20}\text{Ti}_{0.80})\text{O}_3$ -BSTS thin film and BaTiO_3 (BTO) thin films (inset).

presence of long-range ordering electrostatic forces [34]. It is well known that the Raman peaks should not be present in the ideal cubic phase. Figure 3 illustrates the room temperature Raman spectra for BSTS thin films. The room-temperature Raman spectra of the polycrystalline BSTS films are very similar and contain all main features typical of BaTiO_3 (BTO) (Figure 3 inset).

Six characteristic major Raman modes centered were indexed as $E_1(\text{TO}_1) \sim 115 \text{ cm}^{-1}$, $A_1(\text{TO}_1) \sim 177 \text{ cm}^{-1}$, $A_1(\text{TO}_2) \sim 222 \text{ cm}^{-1}$, $B_1/E(\text{TO}_2) \sim 301 \text{ cm}^{-1}$, $A_1(\text{TO}_3) \sim 511 \text{ cm}^{-1}$, and $A_1(\text{LO})/E(\text{LO}) \sim 742 \text{ cm}^{-1}$. Similar to pure BaTiO_3 film sample, BSTS thin film. The $E(\text{TO}_1)$ soft mode is underdamped and shifted to $\sim 115 \text{ cm}^{-1}$ [34, 35]. As shown in Figure 3, the A_1 soft mode only exists in ferroelectric phase and this $A_1(\text{TO}_2)$ mode is observed at 221 cm^{-1} ; on the contrary to that of pure BTO at 262 cm^{-1} , a considerable downshift in Raman frequency is noticed; similar results were reported for BST-0.3 ceramics and thin films [35].

However the weak $B_1/E(\text{TO}_2)$ mode which has been associated with the tetragonal-cubic phase transition was observed at around 301 cm^{-1} . This mode has a mixed character of the B_1 and $E(\text{TO}_2)$ derived from the F_{2u} cubic silent mode [36, 37]. The interference of the asymmetric sharp $A_1(\text{TO}_1)$ mode at 177 cm^{-1} with the broad $A_1(\text{TO}_2)$ mode at about 222 cm^{-1} results in an antiresonance effect at 177 cm^{-1} . The asymmetric $A_1(\text{TO}_3)$ mode couples weakly with the $A_1(\text{TO}_2)$ mode [38]. The presence of well-built peak related to the $A_1(\text{LO})$ mode confirms tetragonal structure in the BSTS films at room temperature [39, 40].

Shift in $A_1(\text{TO}_1)$ and $A_1(\text{TO}_2)$ modes either to lower or higher wave number region is attributed to the asymmetric Ti-O phonon vibrations in BaTiO_3 lattice, while the $A_1(\text{TO}_3)/E(\text{TO}_3)$ mode at around 511 cm^{-1} is due to O-Ti-O symmetric stretching vibrations. On the other hand, the peak position of Raman mode $B_1/E(\text{TO}_2)$ shifted to lower wave number region and $A_1(\text{LO})/E(\text{LO})$ mode is shifted to higher wave number region when compared to pure BaTiO_3

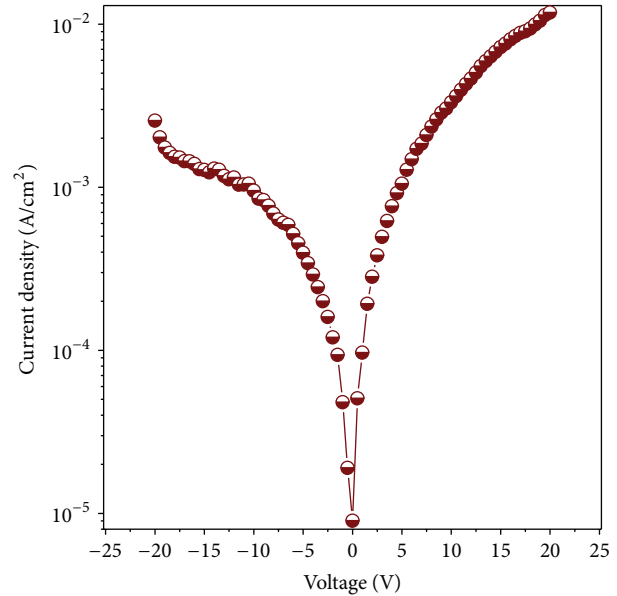


FIGURE 4: Leakage current behavior (current density versus voltage) of BSTS thin film.

films. It is well known from the literature that the phonon frequencies may shift to either lower or higher peak positions and are compositional dependent. Due to either tensile or compressive stress, the phonon wave numbers are expected to shift towards either higher or lower region [35]. Increasing Sr^{2+} concentration at BST thin film, the lattice of the films is compressed; thus the tensile stress which is deduced from the lattice compression might be accountable for the $A_1(\text{LO})/E(\text{LO})$ mode shift towards a higher wave number region in Raman spectra and as well residual stress is not released in the films [39].

Moreover we also observed an additional disordered activated Raman mode at about 567 cm^{-1} in the BSTS films marked by asterisk which does not appear for pure BaTiO_3 . Similar Raman mode was reported for $\text{Ba}_{1-x}\text{Sr}_x\text{TiO}_3$ thin films [35, 39]. Wang et al. [41] also reported similar Raman modes around 535 cm^{-1} and 750 cm^{-1} and they shifted to higher wavenumber region for compositionally graded multilayered $(\text{Ba}_{0.8}\text{Sr}_{0.2})(\text{Ti}_{1-x}\text{Zr}_x)\text{O}_3$ (BSTZ) thin films, which might be attributed to increasing internal strain in the films. Presence of this disordered activated Raman mode is also expected from the eight-site model due to disorder of Ti ions, which can occupy four off-center sites in the tetragonal phase in perovskite oxides [35]. Apparently Sr^{2+} substitution at Ba^{2+} site in BTO lattice caused local distortions and partially breaks the translational symmetry in the lattice and there it is more complicated in disorder-activated background in BST films [35]. All the main Raman modes in BSTS films become broadened which is attributed to structural disorder in the crystalline BSTS lattice [39].

To investigate the leakage current behavior of the films, current density ($\log J$) versus the dc bias voltage (V) characteristics on the metal-insulator-metal (MIM) configuration for the BSTS film annealed at 750°C for 30 min and Figure 4

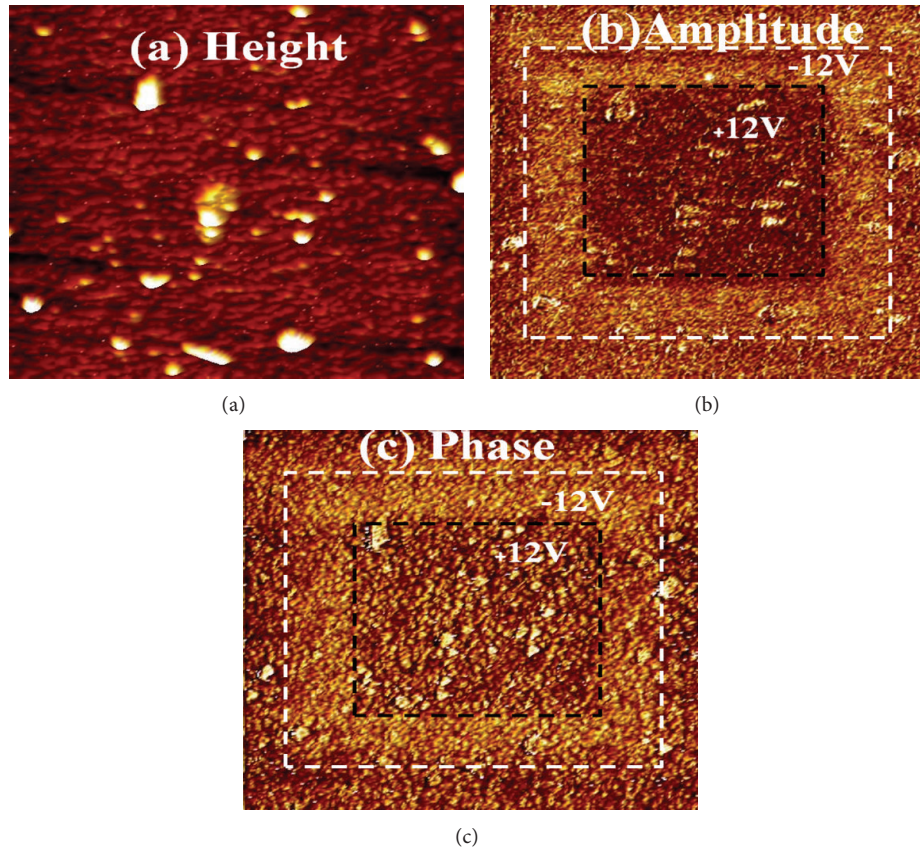


FIGURE 5: (a) Surface topography (PFM) image, (b) PFM amplitude image, (c) PFM phase image, and square patterns of different areas written on the surface confirm the switchability of ferroelectric polarization under ± 12 V bias voltage of BSTS films.

presents the obtained results. The voltage-step and the delay-time after applying each voltage-step were fixed at 0.5 V and 1 s, respectively. The films exhibit low to moderate leakage current density ($\sim 10^{-5}$ – 10^{-2} A/cm²). For low voltages the leakage current is low and at high voltages the leakage currents are increased from the beginning 0 to 20 V. The observed log J - V -loops are noticeably asymmetrical (Figure 4). The possible asymmetry of the two branches in the leakage currents might be due to the fact that the positive and negative bias were measured on single pad (top electrode Pt dot on shadow mask), rather than using different Pt top electrode pad. Low to moderate leakage current density might be due to the possible degradation effect of the film. Thin film degradation and asymmetry can be avoidable by measuring the leakage current for positive and negative bias are measured on different top Pt electrode pads [42]. Controlling this asymmetric behavior in thin films improved device reliability and stability can be achieved.

Ferroelectric (piezoelectric) nature at the nanoscale level is determined by piezoresponse force microscopy (PFM). PFM is a powerful tool for imaging and characterizing ferroelectric domain structures at nanoscale level [43, 44]. The piezoresponse for the BSTS films is obtained utilizing commercially available Si-tip of the PFM in contact mode by applying a DC voltage between the tip (top electrode) and the Pt/TiO_x/SiO₂/Si substrate as bottom electrode of

the film. As shown in Figure 5(a), the BSTS films exhibit atomically flat surface with overall mesh-like pattern with a root-mean-square roughness of approximately 1.5 nm over an area of $8 \times 8 \mu\text{m}^2$. The topographical height image also reveals a polycrystalline structure with 0.2 Å sized grains. Square patterns were written on the film with $8 \times 8 \mu\text{m}^2$ areas (outer square) at -12 V; the domain changes its orientation and the central $4 \times 4 \mu\text{m}^2$ area (inner square) with $+12$ V DC bias is applied; it reverses its polarity. Figures 5(b) and 5(c) show the representative out-of-plane PFM phase and amplitude of ferroelectric domains written on the BSTS film surface at room temperature. From Figures 5(b) and 5(c) it is observed that the ferroelectric switching contrast in the BSTS film. It is also clear from the phase and amplitude images that there exists a strong domain switching response for both negative (outer square) and positive bias (inner square). The square patterns clearly show the oppositely written regions establishing that the BSTS films show nanoscale switching behavior which confirms ferroelectric piezoelectric nature. The out-of-plane piezoresponse local hysteresis loops were determined as a function of applied voltage and the PFM hysteresis loop both in amplitude and phase is shown in Figure 6. The phase change is about 180° and is observed for a complete polarization reversal of the grain. Butterfly shaped amplitude hysteresis and phase images confirm the ferroelectric piezoelectric properties at the nanoscale level.

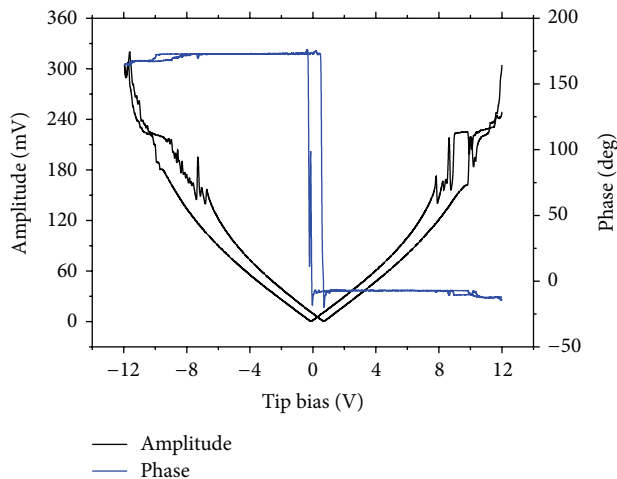


FIGURE 6: Local hysteresis loops measured by PFM amplitude and phase loops from microscopic measurements of BSTS films.

The observed local coercive voltage minima from the amplitude loops are found to be +0.75 V and -0.10 V.

4. Conclusion

In summary, we have investigated the structural, leakage current, and nanoscale ferroelectric switching behavior of $(\text{Ba}_{0.50}\text{Sr}_{0.50})(\text{Sn}_{0.20}\text{Ti}_{0.80})\text{O}_3$ -BSTS thin films by chemical solution deposition on $\text{Pt}/\text{TiO}_x/\text{SiO}_2/\text{Si}$ substrates. XRD and Raman spectra confirm perovskite crystalline structure in the BSTS films. All the main peaks corresponding to tetragonal symmetric group were present in the room temperature Raman spectra. Tetragonal $A_1(\text{LO})/E(\text{LO})$ mode shift towards a higher wave number region in Raman spectra might be attributed to tensile stress in the films. Local piezoelectric activity of the BSTS films was investigated by Piezoresponse Force Microscopy (PFM) technique. PFM studies revealed nanoscale ferroelectric switching in the chemical solution deposited annealed samples.

Conflict of Interests

The authors declare that there is no conflict of interests regarding the publication of this paper.

Acknowledgment

This work was supported by the National Science Foundation under Grant NSF-EFRI RESTOR no. 1038272.

References

- [1] J. F. Scott and C. A. P. de Araujo, "Ferroelectric memories," *Science*, vol. 246, no. 4936, pp. 1400–1405, 1989.
- [2] J. F. Scott, *Ferroelectric Memories*, Springer Series in Advanced Microelectronics, Springer, 2000.
- [3] S. J. Zhang, R. Xia, and T. R. Shrout, "Modified $(\text{K}_{0.5}\text{Na}_{0.5})\text{NbO}_3$ based lead-free piezoelectrics with broad temperature usage

range," *Applied Physics Letters*, vol. 91, no. 13, Article ID 132913, 2007.

- [4] I. A. Souza, A. Z. Simões, E. Longo, and J. A. Varela, "Synthesis of $\text{Ba}_{0.5}\text{Sr}_{0.5}(\text{Ti}_{0.80}\text{Sn}_{0.20})\text{O}_3$ prepared by the soft chemical method," *Materials Letters*, vol. 61, no. 19-20, pp. 4086–4089, 2007.
- [5] V. S. Puli, D. K. Pradhan, B. C. Riggs, D. B. Chrisey, and S. Katiyar, "Structure, ferroelectric, dielectric and energy storage studies of $\text{Ba}_{0.70}\text{Ca}_{0.30}\text{TiO}_3$, $\text{Ba}(\text{Zr}_{0.20}\text{Ti}_{0.80})\text{O}_3$ ceramic capacitors," *Integrated Ferroelectrics*, vol. 157, no. 1, pp. 1–8, 2014.
- [6] N. N. Baskaran and H. Chang, "Thermo-Raman and dielectric constant studies of $\text{Ca}_x\text{Ba}_{1-x}\text{TiO}_3$ ceramics," *Materials Chemistry and Physics*, vol. 77, no. 3, pp. 889–894, 2003.
- [7] T. Mitsui and W. B. Westphal, "Dielectric and X-ray studies of $\text{Ca}_x\text{Ba}_{1-x}\text{TiO}_3$ and $\text{Ca}_x\text{Sr}_{1-x}\text{TiO}_3$," *Physical Review*, vol. 124, no. 5, pp. 1354–1359, 1961.
- [8] L.-F. Zhu, B.-P. Zhang, X.-K. Zhao et al., "Phase transition and high piezoelectricity in $(\text{Ba,Ca})(\text{Ti}_{1-x}\text{Sn}_x)\text{O}_3$ lead-free ceramics," *Applied Physics Letters*, vol. 103, no. 7, Article ID 072905, 2013.
- [9] I. Coondoo, N. Panwar, H. Amorín, M. Alguero, and A. L. Kholkin, "Synthesis and characterization of lead-free $0.5\text{Ba}(\text{Zr}_{0.2}\text{Ti}_{0.8})\text{O}_3$ - $0.5(\text{Ba}_{0.7}\text{Ca}_{0.3})\text{TiO}_3$ ceramic," *Journal of Applied Physics*, vol. 113, no. 21, Article ID 214107, 2013.
- [10] E. Venkata Ramana, A. Mahajan, M. P. F. Graça, S. K. Mendiratta, J. M. Monteiro, and M. A. Valente, "Structure and ferroelectric studies of $(\text{Ba}_{0.85}\text{Ca}_{0.15})(\text{Ti}_{0.9}\text{Zr}_{0.1})\text{O}_3$ piezoelectric ceramics," *Materials Research Bulletin*, vol. 48, no. 10, pp. 4395–4401, 2013.
- [11] J. P. Praveen, K. Kumar, A. R. James, T. Karthik, S. Asthana, and D. Das, "Large piezoelectric strain observed in sol-gel derived BZT-BCT ceramics," *Current Applied Physics*, vol. 14, no. 3, pp. 396–402, 2014.
- [12] Y. D. Kolekar, A. Bhaumik, P. A. Shaikh, C. V. Ramana, and K. Ghosh, "Polarization switching characteristics of $0.5\text{BaTi}_{0.8}\text{Zr}_{0.2}\text{O}_3$ - $0.5\text{Ba}_{0.7}\text{Ca}_{0.3}\text{TiO}_3$ lead free ferroelectric thin films by pulsed laser deposition," *Journal of Applied Physics*, vol. 115, Article ID 154102, 2014.
- [13] V. S. Puli, D. K. Pradhan, D. B. Chrisey et al., "Structure, dielectric, ferroelectric, and energy density properties of $(1-x)\text{BZT-xBCT}$ ceramic capacitors for energy storage applications," *Journal of Materials Science*, vol. 48, no. 5, pp. 2151–2157, 2013.
- [14] L.-F. Zhu, B.-P. Zhang, X.-K. Zhao, L. Zhao, P.-F. Zhou, and J.-F. Li, "Enhanced piezoelectric properties of $(\text{Ba}_{x-1}\text{Ca}_x)(\text{Ti}_{0.92}\text{Sn}_{0.08})\text{O}_3$ lead-free ceramics," *Journal of the American Ceramic Society*, vol. 96, no. 1, pp. 241–245, 2013.
- [15] S. Mahajan, O. P. Thakur, K. Sreenivas, and C. Prakash, "Effect of Nd doping on structural, dielectric and ferroelectric properties of $\text{Ba}(\text{Zr}_{0.05}\text{Ti}_{0.95})\text{O}_3$ ceramic," *Integrated Ferroelectrics*, vol. 122, no. 1, pp. 83–89, 2010.
- [16] V. S. Puli, D. K. Pradhan, S. Adireddy et al., *Investigations on the Dielectric, Ferroelectric and Energy Storage Properties of Barium Zirconate-Titanate/Barium Calcium-Titanate Based Ceramic for High Energy Density Capacitors*, Nova Science Publishers, Hauppauge, NY, USA, 2014.
- [17] W. Xing, Y. Ma, Z. Ma, Y. Bai, J. Chen, and S. Zhao, "Improved ferroelectric and leakage current properties of Er-doped BiFeO_3 thin films derived from structural transformation," *Smart Materials and Structures*, vol. 23, no. 8, Article ID 085030, 2014.
- [18] X. Wang, X. Chao, P. Liang, L. Wei, and Z. Yang, "Polymorphic phase transition and enhanced electrical properties of

- (Ba_{0.91}Ca_{0.09-x}Sr_x)(Ti_{0.92}Sn_{0.08})O₃ lead-free ceramics,” *Ceramics International*, vol. 40, no. 7, pp. 9389–9394, 2014.
- [19] Y.-P. Wang and T.-Y. Tseng, “Electronic defect and trap-related current of (Ba_{0.4}Sr_{0.6})TiO₃ thin films,” *Journal of Applied Physics*, vol. 81, no. 10, pp. 6762–6766, 1997.
- [20] W. Chang, J. S. Horwitz, A. C. Carter et al., “The effect of annealing on the microwave properties of Ba_{0.5}Sr_{0.5}TiO₃ thin films,” *Applied Physics Letters*, vol. 74, no. 7, pp. 1033–1035, 1999.
- [21] L. M. B. Alldredge, W. Chang, S. B. Qadri, S. W. Kirchoefer, and J. M. Pond, “Ferroelectric and paraelectric Ba_{0.5}Sr_{0.5}TiO₃ film structure distortions at room temperature and their effects on tunable microwave properties,” *Applied Physics Letters*, vol. 90, no. 21, Article ID 212901, 2007.
- [22] M. Tsukada, M. Mukaida, and S. Miyazawa, “Structural and dielectric properties of Ba(Ti_{1-x}Sn_x)O₃ thin films,” *Japanese Journal of Applied Physics*, vol. 35, no. 9, pp. 4908–4912, 1996.
- [23] N. Yasuda, H. Ohwa, and S. Asano, “Dielectric properties and phase transitions of Ba(Ti_{1-x}Sn_x)O₃ solid solution,” *Japanese Journal of Applied Physics, Part I: Regular Papers and Short Notes and Review Papers*, vol. 35, no. 9, pp. 5099–5103, 1996.
- [24] K. H. Yoon, J. H. Park, and J. H. Jang, “Solution deposition processing and electrical properties of Ba(Ti_{1-x}Sn_x)O₃ thin films,” *Journal of Materials Research*, vol. 14, no. 7, pp. 2933–2939, 1999.
- [25] J. W. Zhai, B. Shen, X. Yao, and L. Y. Zhang, “Dielectric and ferroelectric properties of Ba(Sn_{0.15}Ti_{0.85})O₃ thin films grown by a sol-gel process,” *Materials Research Bulletin*, vol. 39, no. 11, pp. 1599–1606, 2004.
- [26] S. Halder, P. Victor, A. Laha et al., “Pulsed excimer laser ablation growth and characterization of Ba(Sn_{0.1}Ti_{0.9})O₃ thin films,” *Solid State Communications*, vol. 121, no. 6-7, pp. 329–332, 2002.
- [27] J. Zhai, B. Shen, X. Yao, L. Zhang, and H. Chen, “Dielectric properties of Ba(Sn_xTi_{1-x})O₃ thin films grown by a sol-gel process,” *Journal of the American Ceramic Society*, vol. 87, no. 12, pp. 2223–2227, 2004.
- [28] M.-C. Wang, C.-C. Tsai, N.-C. Wu, and K.-M. Hung, “Structural and dielectric characterization of the (Ba_{1-x}Sr_x)(Ti_{0.9}Sn_{0.1})O₃ thin films deposited on Pt/Ti/SiO₂/Si substrate by radio frequency magnetron sputtering,” *Journal of Applied Physics*, vol. 92, no. 4, pp. 2100–2107, 2002.
- [29] I. A. Souza, A. Z. Simões, S. Cava et al., “Ferroelectric and dielectric properties of Ba_{0.5}Sr_{0.5}Ti_{0.80}Sn_{0.20}O₃ thin films grown by the soft chemical method,” *Journal of Solid State Chemistry*, vol. 179, pp. 2972–2976, 2006.
- [30] R. Nath, S. Zhong, S. P. Alpay, B. D. Huey, and M. W. Cole, “Enhanced piezoelectric response from barium strontium titanate multilayer films,” *Applied Physics Letters*, vol. 92, no. 1, Article ID 012916, 2008.
- [31] H. Miao, C. Tan, X. Zhou, X. Wei, and F. Li, “More ferroelectrics discovered by switching spectroscopy piezoresponse force microscopy?” *Europhysics Letters*, vol. 108, no. 2, Article ID 27010, 2014.
- [32] J.-C. Carru, M. Mascot, and D. Fasquelle, “Electrical characterizations of lead free Sr and Sn doped BaTiO₃ ferroelectric films deposited by sol-gel,” in *Ferroelectrics—Material Aspects*, M. Lallart, Ed., chapter 3, InTech, 2011.
- [33] Y. I. Yuzyuk, V. A. Alyoshin, I. N. Zakharchenko, E. V. Sviridov, A. Almeida, and M. R. Chaves, “Polarization-dependent Raman spectra of heteroepitaxial (Ba,Sr)TiO₃/MgO thin films,” *Physical Review B*, vol. 65, no. 13, Article ID 134107, 9 pages, 2002.
- [34] D. A. Tenne, A. Soukiassian, X. X. Xi, H. Choosuwan, R. Guo, and A. S. Bhalla, “Lattice dynamics in Ba_xSr_{1-x}TiO₃ thin films studied by Raman spectroscopy,” *Journal of Applied Physics*, vol. 96, no. 11, pp. 6597–6605, 2004.
- [35] R. S. Katiyar, M. Jain, and Y. I. Yuzyuk, “Raman spectroscopy of bulk and thin-layer (Ba,Sr)TiO₃ ferroelectrics,” *Ferroelectrics*, vol. 303, pp. 101–105, 2004.
- [36] M. Didomenico Jr., S. H. Wemple, S. P. S. Porto, and R. P. Bauman, “Raman spectrum of single-domain BaTiO₃,” *Physical Review*, vol. 174, no. 2, pp. 522–530, 1968.
- [37] J. D. Freire and R. S. Katiyar, “Lattice dynamics of crystals with tetragonal BaTiO₃ structure,” *Physical Review B*, vol. 37, no. 4, pp. 2074–2085, 1988.
- [38] A. Scalabrin, A. S. Chaves, D. S. Shim, and S. P. S. Porto, “Temperature dependence of the A₁ and E optical phonons in BaTiO₃,” *Physica Status Solidi B*, vol. 79, no. 2, pp. 731–742, 1977.
- [39] L. Z. Cao, B. L. Cheng, S. Y. Wang et al., “Influence of stress on Raman spectra in Ba_{1-x}Sr_xTiO₃ thin films,” *Journal of Physics D: Applied Physics*, vol. 39, no. 13, pp. 2819–2823, 2006.
- [40] R. Naik, J. J. Nazarko, C. S. Flattery et al., “Temperature dependence of the Raman spectra of polycrystalline Ba_{1-x}Si_xTiO₃,” *Physical Review B*, vol. 61, no. 17, pp. 11367–11372, 2000.
- [41] C. Wang, B. L. Cheng, S. Y. Wang, S. Y. Dai, and Z. H. Chen, “Raman spectra study on multilayered compositional graded (Ba_{0.8}Sr_{0.2})(Ti_{1-x}Zr_x)O₃ thin films,” *Key Engineering Materials*, vol. 280–283, pp. 1909–1912, 2005.
- [42] P. Ehrhart and R. Thomas, “Electrical properties of (Ba,Sr)TiO₃ thin films revisited: the case of chemical vapor deposited films on Pt electrodes,” *Journal of Applied Physics*, vol. 99, no. 11, Article ID 114108, 2006.
- [43] A. Gruverman, O. Auciello, and H. Tokumoto, “Imaging and control of domain structures in ferroelectric thin films via scanning force microscopy,” *Annual Review of Materials Science*, vol. 28, no. 1, pp. 101–123, 1998.
- [44] A. Gruverman and S. V. Kalinin, “Piezoresponse force microscopy and recent advances in nanoscale studies of ferroelectrics,” *Journal of Materials Science*, vol. 41, no. 1, pp. 107–116, 2006.

Research Article

Ferromagnetic Property of Co and Ni Doped TiO₂ Nanoparticles

Qing Wang, Xiaoming Liu, Xuegang Wei, Jianfeng Dai, and Weixue Li

School of Science, Lanzhou University of Technology, Lanzhou 730050, China

Correspondence should be addressed to Qing Wang; wangqing@lut.cn

Received 12 March 2015; Accepted 14 April 2015

Academic Editor: Zijie Yan

Copyright © 2015 Qing Wang et al. This is an open access article distributed under the Creative Commons Attribution License, which permits unrestricted use, distribution, and reproduction in any medium, provided the original work is properly cited.

The Co and Ni doped diluted magnetic semiconductor nanoparticle TiO₂ is prepared by sol-gel method. Ti_{0.97}Co_{0.03}O₂, Ti_{0.97}Ni_{0.03}O₂, Ti_{0.97}Co_{0.06}O₂, and Ti_{0.97}Ni_{0.06}O₂ samples were characterized by X-ray scattering techniques and high resolution transmission electron microscope. The results show that there are no other phases existing in TiO₂. As to the sample of high-concentration dopant, the X-ray scattering techniques have explored the existing of CoTiO₃ and NiTiO₃. The ferromagnetic measurement shows that the magnetization of the sample of high-concentration dopant increases in the same external magnetic field. However, the relatively higher dopant Co and Ni may form more interstitial ions and paramagnet matters, reducing the oxygen vacancy concentration and finally leading to the decrease of remanent magnetization and coercivity of the materials.

1. Introduction

The diluted magnetic semiconductors (DMS) share the qualities of both semiconductors and magnetic materials, such as ferromagnetism and magnetic and magnetoelectricity. Moreover, the application of the diluted magnetic semiconductors is widely promising in various fields, such as spin light-emitting diode [1], logic device [2], the electric charge of spin valve crystal and spin of electron [3], and nonvolatile memory. As a result, it is one of the hottest research spots and attracts a great number of attentions [4–9].

TiO₂ is a high refractive index transparent and high dielectric constant material. It is also a wide bandgap semiconductor, which can readily generate ferromagnetism when heat treated in vacuum or hydrogen. Since TiO₂ exhibits the characteristics of both the semiconductor and the magnetic material, it can realize the dual control of both electric and magnetic fields by using the electric charge and spin properties of electrons. To achieve the application of the diluted magnetic semiconductors TiO₂, it is important to prepare room-temperature diluted magnetic semiconductor materials with high saturation magnetization intensity. Up to now, the room-temperature ferromagnetism of diluted magnetic semiconductors has been improved by changing the producing method, annealing atmosphere and the appearance of the samples, and doping different metallic ions and

nonmetallic ions. Many methods have been used to prepare diluted magnetic semiconductors, such as molecular beam epitaxy (MBE) [10], magnetron sputtering [11], pulsed laser deposition [12], ion implantation [13], and sol-gel method [14]. Different methods have great influence on the properties of material. For example, sol-gel method has the advantages of easy operation and low costs. Moreover, this method can prepare nanoparticles with narrow size distribution and controllable chemical composition at a lower temperature. In this paper, the Co and Ni doped TiO₂ nanoparticles were prepared by the sol-gel method, and the microstructure and ferromagnetism of samples were studied.

2. Experiments

The following is the process of the experiments. Firstly, the 0.057 mol [CH₃(CH₂)₃O]₄Ti is added to anhydrous ethanol (99.9%) with the volume ratio of 1 : 3, and the solution is fully mixed until it converts into the uniform transparent light yellow liquid. Secondly, 622 mg, 1270 mg Co(NO)₃·6H₂O, 621 mg, and 1268 mg Ni(NO)₃·6H₂O are dissolved in 10 mL anhydrous ethanol, respectively. Thirdly, while mixing, 4 mL glacial acetic acid, 2 mL concentrated nitric acid, and 3 mL deionized water are added to the mixed solution, respectively. Fourthly, after the mixed solution is stirred for 4 hours at room temperature, it is aged for 72 hours at room

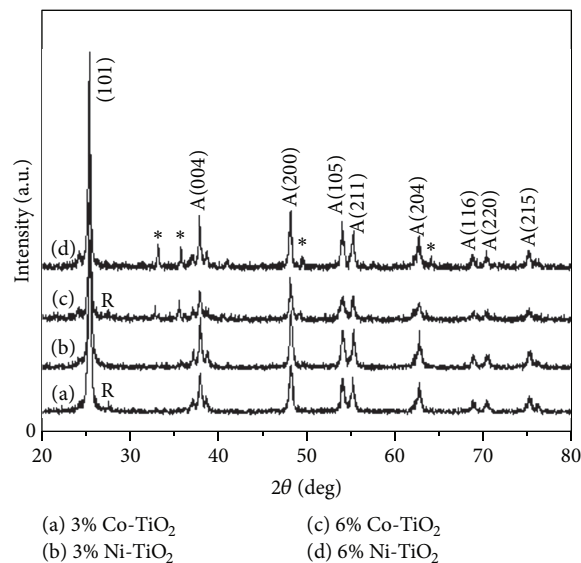


FIGURE 1: XRD patterns of CN-01, CN-02, CN-03, and CN-04 samples annealed at 500°C for 1 h in the air (A: anatase; R: rutile; and *: disturbance phases).

temperature. When the solution converts into stable collosol, the stable collosol is put in the drying oven set at 80°C and dried for 24 hours, by which xerogel is produced. Finally, Markov furnace is used to lay xerogel in the air with an annealing temperature of 500°C to anneal for an hour. After being ground, the nanoparticle TiO₂ is obtained with different concentration and elements. Ti_{0.97}Co_{0.03}O₂ (CN-01), Ti_{0.97}Ni_{0.03}O₂ (CN-02), Ti_{0.97}Co_{0.06}O₂ (CN-03), and Ti_{0.97}Ni_{0.06}O₂ (CN-04) are prepared.

3. Results and Discussion

In the present work, the prepared samples were characterized by X-ray diffraction (XRD, D8 advance) with CuK α radiation ($\lambda = 0.15406$ nm). Figure 1 is the XRD patterns of Co and Ni doped TiO₂ nanoparticles with different doping concentration. Compared with the standard data (JCPDS, 78-2486), a small amount of rutile is found in the sample of doped Co, while in the sample of doped Ni there is no observation of rutile. The doped 3 mol% sample is pure TiO₂ phase structure, and no other phases were observed, while in the doped 6 mol% sample there are disturbance phases, which are produced mainly due to high dosage concentration. Moreover, from Figure 1, it is observed that the diffraction peaks of Ni doped sample are sharper and stronger than Co doped samples, so that the crystallinity of Ni doped TiO₂ is more superior than that of Co doped sample. By comparing 3 mol% Co doped sample with 6 mol% Co doped sample, it is found that there is no obvious change of diffraction angle, and the only difference is that the diffraction peak of Co doped 3 mol% is stronger, which means superfluous doped Co will decrease the crystallinity. As for the doped Ni, the diffraction peak of doped 3 mol% Ni is stronger than that of doped 6 mol% Ni. By using the Scherrer equation $D = 0.9\lambda/\beta \cos \theta$ and taking (101) crystal face diffraction peak as standard, it is

calculated that the sizes of doped 3 mol% Co grain and doped 3 mol% Ni grain are 29.71 nm and 34.15 nm, respectively.

High Resolution Transmission Electron Microscopy (HRTEM, JEM-2010) is used to observe the microstructure of the sample and the change of the interplanar spacing between doped samples. Figure 2 shows the results of HRTEM observation of samples CN-01 and CN-02. Figure 2(a) shows that the sizes of the prepared nanoparticles are between 30 and 40 nm, and the images of their corresponding electron diffraction rings are inserted below. The diffraction ring of the nanoparticles is presented as a spotty ring micrograph, and there are no other phases of diffraction spots such as Co, CoO, Co₃O₄, CoTiO₃, or CoTi₂O₅. This means that no structure change of anatase TiO₂ was found. According to the standard electron diffraction ring data (JCPDS, 78-2486), the corresponding crystal face of the diffraction ring can be judged; they are (101), (103), (200), and (105) from outside to inside.

Figure 2(b) is the corresponding lattice structure. In the figure, there is no extra lattice imperfection; on the contrary, the observation shows that there are many regularly arranged wrinkled stripes, which means they have high crystallisation degree. The interplanar spacing is 0.3533 nm, and its corresponding crystal face (101) is slightly increased compared with the standard micrograph (JCPDS, 78-2486), which is caused by lattice distortion. Thus, it is proved again that Co²⁺ replaces Ti²⁺ in the lattice of TiO₂. Figure 2(c) is the appearance of the sample of doped Ni. As the figures show, the shape of nanoparticles is block, and the sizes are between 10 nm and 40 nm. The pictures of their corresponding electron diffraction rings are inserted below, and the diffraction ring of the nanoparticles is also presented as a spotty ring micrograph. In Figure 2(d), it is measured that the corresponding interplanar spacing of crystal face is 0.3528, which means Ni²⁺ replaces Ti²⁺.

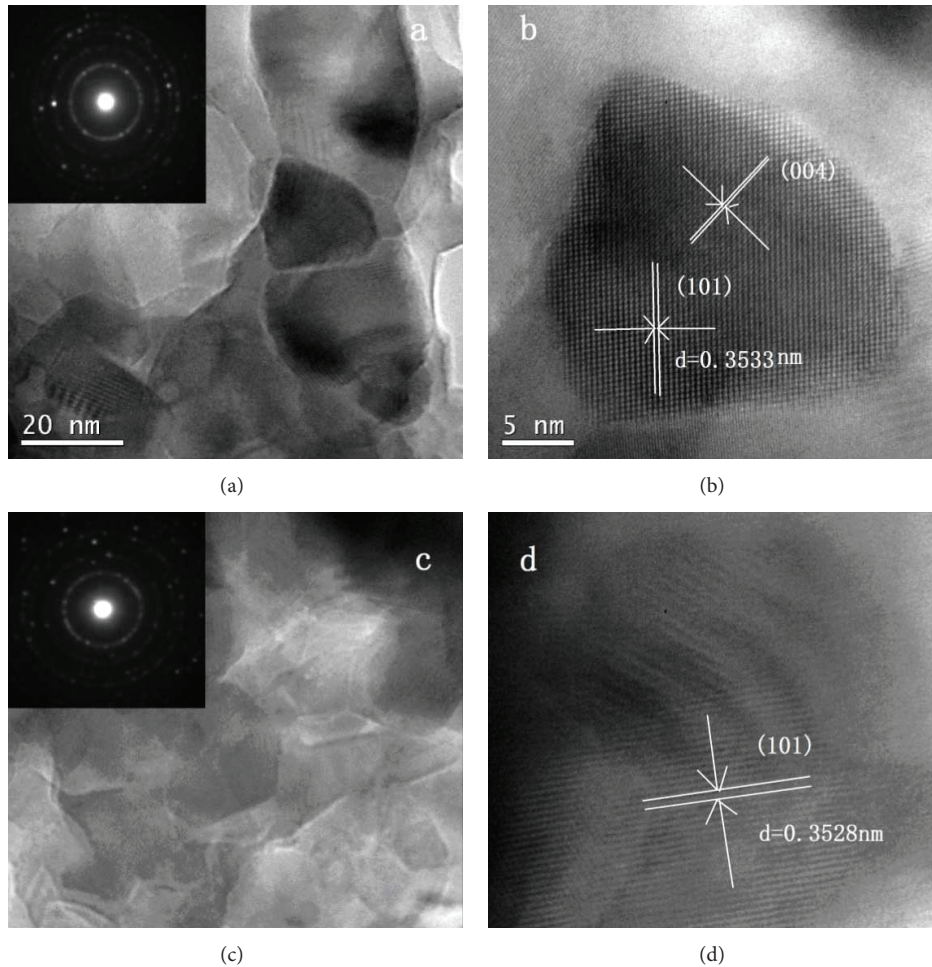


FIGURE 2: (a–d) display the HRTEM micrographs: (a, b) CN-01; (c, d) CN-03.

Figures 3(a) and 3(b) are the EDS (Genesis XM2) spectra of the samples CN-01 and CN-03, respectively. The figures show except the samples come from the characteristic peak (8.1 and 8.9 Kev) of Cu in the bronze grating which carry the samples in the experiment; in the samples, there are only O, Ti, Co (CN-01) and O, Ti, Ni (CN-03) three elements. In Figure 3(a), the atom percentages of O, Ti, and Co are 65.22, 33.81, and 0.97, respectively, while in Figure 3(b), the percentages are 65.02, 33.96, and 1.02. The results show that, in the doped samples, there are only doped elements, and the percentage of the doped elements is close to the doped 3 mol% in the experiment.

The magnetic properties were investigated by a vibrating sample magnetometer (VSM 7403, Lakeshore, USA). Figure 4 is the magnetic hysteresis loops of the four samples tested at 300 K. The figure shows that all the samples are magnetic at room temperature. In Figure 4(a), in the relatively weak applied magnetic field, the intensity of magnetization of the sample CN-02 reaches its saturation condition, while the intensity of magnetization produced by sample CN-01 is stronger than that of sample CN-02. Moreover, in the applied magnetic field, the intensity of magnetization sample CN-01 does not reach its saturation condition at 2000

(Oe). The illustrations are residual magnetization (M_r) and coercivity (H) of sample CN-01 and sample CN-02 measured at room temperature, from which the residual magnetization produced by sample CN-01 is higher than that of sample CN-02, but it is evident that its coercivity is lower than sample CN-02. It proves that magnetism produced by the samples is relevant to Co^{2+} and Ni^{2+} themselves.

Figure 4(b) is the magnetic hysteresis loops of samples CN-03 and CN-04. The figure shows that hysteresis produced by the samples has not reached the saturation condition, the quality of which also exists in the nanoribbon or nanoparticles of TiO_2 doped with Co^{2+} or Ni^{2+} [13, 14]. After comparing the samples CN-01 and CN-02, the intensity of magnetization produced by samples CN-03 and CN-04 increases to different extent, but the residual magnetization (M_r) and coercivity (H) are apparently decreased, as is shown in Table 1. The major reason is that, with the increase of dosage concentration, more doping ion Co^{2+} or Ni^{2+} replaces Ti^{4+} in the samples which increase the intensity of magnetization produced by the samples. The reason why the residual magnetization (M_r) and coercivity (H) produced by them are apparently decreased is that the high dosage concentration

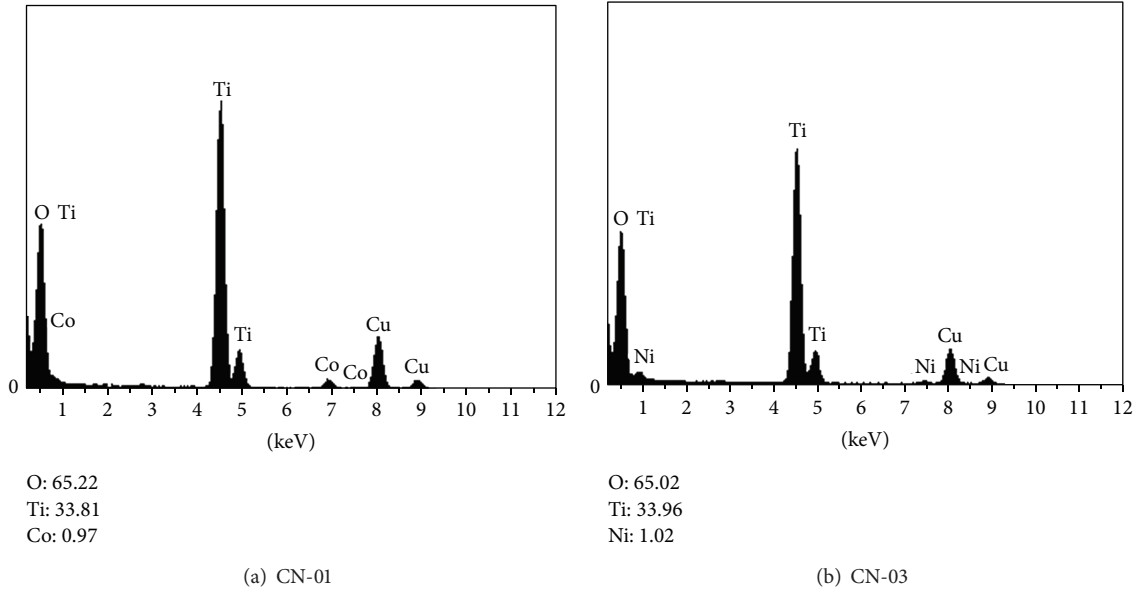


FIGURE 3: EDS spectra of 3 mol% doped TiO_2 samples. (a) CN-01. (b) CN-03.

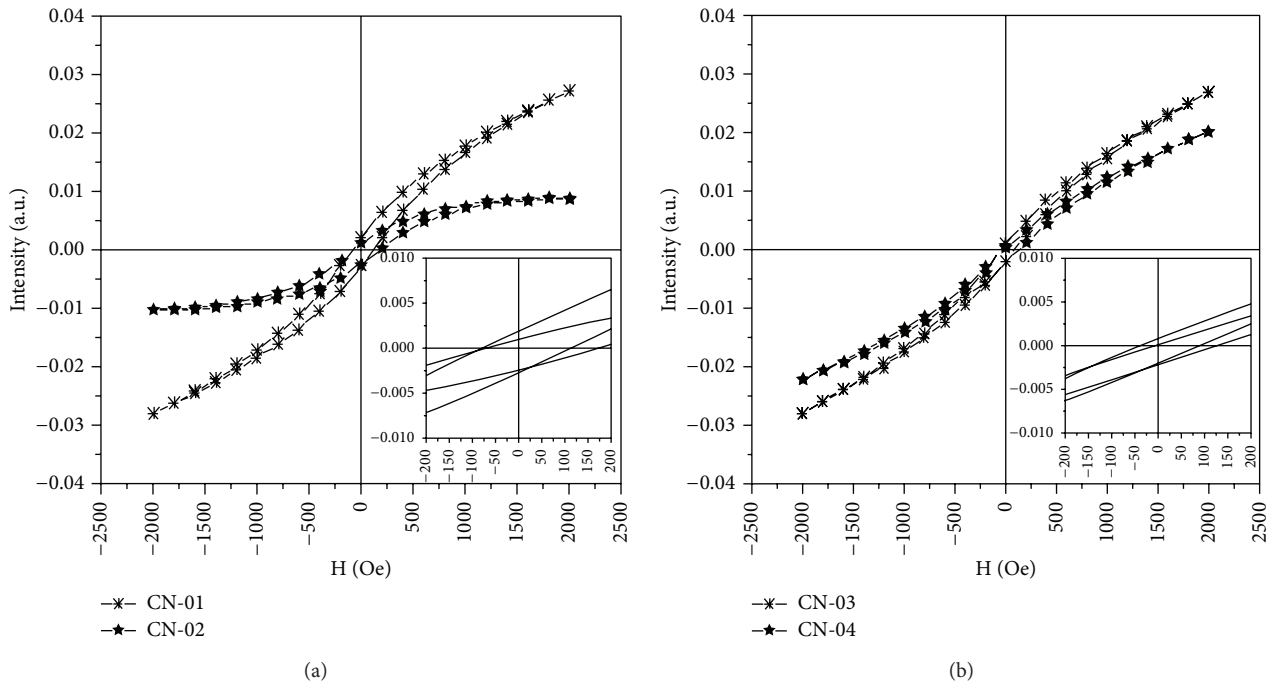


FIGURE 4: The magnetic hysteresis loops measured at room temperature for the CN-01, CN-02, CN-03, CN-04 samples.

produces paramagnetic phases TiCoO_3 and TiNiO_3 in the growing process of crystal. Moreover, in Figures 4(a) and 4(b), the intensity of magnetization produced by Co^{2+} doped TiO_2 is greater than Ni^{2+} . Since there exist differences in orbital electron number of Co^{2+} and $\text{Ni}^{2+}3d$, it is certain that the room-temperature ferromagnetism produced by the samples has relevance with the orbital electron of doped Co^{2+} and $\text{Ni}^{2+}3d$, not from the defects of the samples themselves.

It is still not clear about the origin of DMS ferromagnetism. There are currently two theories to explain the observed ferromagnetism. One is the ferromagnetic exchange coupling mediated by carriers, and the other is the bound magnetic polaron (BMP) model, which is related to the defects in materials. The above study means that the origin of DMS ferromagnetism is due to the carriers exchange coupling.

TABLE 1: The Ms, Hc, and Mr parameters of samples CN-01, CN-02, CN-03, and CN-04.

Sample	Ms (emu/g)	Hc (Oe)	Mr (emu/g)
6 mol% Co	0.027	88.6	0.0009
6 mol% Ni	0.020	132.9	0.0003
3 mol% Co	0.027	115.2	0.0021
3 mol% Ni	0.008	181.7	0.0011

4. Conclusions

By using the sol-gel method, the diluted magnetic semiconductor nanoparticle Co and Ni doped TiO₂ is produced with the concentration of 3 mol% and 6 mol%. The research results show that firstly Co²⁺ doped samples CN-01 and CN-03 produce the phase of rutile, while in the same condition, Ni²⁺ doped samples CN-02 and CN-04 belong to anatase structure and there is no rutile phase. Moreover, the XRD peak of Ni²⁺ doped samples is stronger than Co²⁺ doped samples of the same concentration. Secondly, the differences of electronic states of Co²⁺ and Ni²⁺ influence the growth patterns of the samples: Co²⁺ doped samples grow spherically and Ni²⁺ doped samples grow massively. Finally, the diluted magnetic semiconductor nanoparticles TiO₂ doped by metal ion and room-temperature ferromagnetism have relevance with doped cations themselves which mainly rely on the interaction between the doped cations and 3D orbital electron.

Conflict of Interests

The authors declare that there is no conflict of interests regarding the publication of this paper.

References

- [1] G. Kioseoglou and A. Petrou, "Spin light emitting diodes," *Journal of Low Temperature Physics*, vol. 169, no. 5-6, pp. 324–337, 2012.
- [2] D. A. Allwood, G. Xiong, C. C. Faulkner, D. Atkinson, D. Petit, and R. P. Cowburn, "Magnetic domain-wall logic," *Science*, vol. 309, no. 5741, pp. 1688–1692, 2005.
- [3] M. Hafeez, A. Ali, S. Manzoor, and A. S. Bhatti, "Anomalous optical and magnetic behavior of multi-phase Mn doped Zn₂SiO₄ nanowires: a new class of dilute magnetic semiconductors," *Nanoscale*, vol. 6, no. 24, pp. 14845–14855, 2014.
- [4] S. Mehraj, M. S. Ansari, and Alimuddin, "Structural, electrical and magnetic properties of (Fe, Co) co-doped SnO₂ diluted magnetic semiconductor nanostructures," *Physica E: Low-Dimensional Systems and Nanostructures*, vol. 65, pp. 84–92, 2015.
- [5] D. Yao, X. Zhou, and S. Ge, "Raman scattering and room temperature ferromagnetism in Co-doped SrTiO₃ particles," *Applied Surface Science*, vol. 257, no. 22, pp. 9233–9236, 2011.
- [6] N. Bahadur, R. Pasricha, S. Chand, and R. K. Kotnala, "Effect of Ni doping on the microstructure and high Curie temperature ferromagnetism in sol-gel derived titania powders," *Materials Chemistry and Physics*, vol. 133, no. 1, pp. 471–479, 2012.
- [7] Y.-B. Sun, X.-Q. Zhang, G.-K. Li, and Z.-H. Cheng, "Effects of oxygen vacancy location on the electronic structure and spin density of Co-doped rutile TiO₂ dilute magnetic semiconductors," *Chinese Physics B*, vol. 21, no. 4, Article ID 047503, 2012.
- [8] P. Varshney, G. Srinet, and R. Kumar, "Room temperature ferromagnetism in sol-gel prepared Co-doped ZnO materials," *Science in Semiconductor Processing*, vol. 15, pp. 314–319, 2012.
- [9] G. Drera, M. C. Mozzati, P. Galinetto et al., "Enhancement of room temperature ferromagnetism in N-doped TiO_{2-x} rutile: correlation with the local electronic properties," *Applied Physics Letters*, vol. 97, no. 1, Article ID 012506, 2010.
- [10] S. A. Chambers and T. Droubay, "Clusters and magnetism in epitaxial Co-doped TiO₂ anatase," *Applied Physics Letters*, vol. 82, no. 8, pp. 1257–1259, 2003.
- [11] K. A. Griffin, A. B. Pakhomov, C. M. Wang, S. M. Heald, and K. M. Krishnan, "Cobalt-doped anatase TiO₂: a room temperature dilute magnetic dielectric material," *Journal of Applied Physics*, vol. 97, no. 10, pp. D320–D322, 2005.
- [12] H. H. Nguyen, W. Prellier, J. Sakai, and A. Ruyter, "Substrate effects on the room-temperature ferromagnetism in Co-doped TiO₂ thin films grown by pulsed laser deposition," *Journal of Applied Physics*, vol. 95, no. 11, pp. 7378–7380, 2004.
- [13] C. M. Wang, V. Shutthanandan, S. Thevuthasan, T. Droubay, and S. A. Chambers, "Microstructure of Co-doped TiO₂ (110) rutile by ion implantation," *Journal of Applied Physics*, vol. 97, no. 7, Article ID 073502, 2005.
- [14] R. Suryanarayanan, V. M. Naik, P. Kharel, P. Talagala, and R. Naik, "Ferromagnetism at 300 K in spin-coated films of Co doped anatase and rutile-TiO₂," *Solid State Communications*, vol. 133, no. 7, pp. 439–443, 2005.

Research Article

Photocatalytically Active $\text{YBa}_2\text{Cu}_3\text{O}_{7-x}$ Nanoparticles Synthesized via a Soft Chemical Route

Zhenjiang Shen,^{1,2} Yongming Hu,^{1,3} Linfeng Fei,¹ Kun Li,¹ Wanping Chen,¹
Haoshuang Gu,³ and Yu Wang¹

¹Department of Applied Physics and Materials Research Center, The Hong Kong Polytechnic University, Hung Hom, Hong Kong

²College of Physics and Electronic Engineering, Hainan Normal University, Haikou 571158, China

³Key Lab of Ferro- & Piezoelectric Materials and Devices of Hubei Province, Faculty of Physics & Electronic Technology, Hubei University, Wuhan 430062, China

Correspondence should be addressed to Zhenjiang Shen; zjshenmail@163.com

Received 28 January 2015; Accepted 28 February 2015

Academic Editor: Min Liu

Copyright © 2015 Zhenjiang Shen et al. This is an open access article distributed under the Creative Commons Attribution License, which permits unrestricted use, distribution, and reproduction in any medium, provided the original work is properly cited.

$\text{YBa}_2\text{Cu}_3\text{O}_{7-x}$ (YBCO) nanoparticles (NPs) were synthesized via a soft chemical approach and they were found photocatalytically active at room temperature. Using metal acetate as precursors, a well-designed soft chemical procedure was carried out to produce YBCO NPs. The very small particle size and/or large number of defects might have led the NPs to semiconductors with vigorous photocatalytic activities. This work provides a direct and efficient route to obtain multifunction in YBCO based nanomaterials which are based on specific size and surface effects.

1. Introduction

High temperature superconductivity has been one of the most important chapters in the field of solid-state physics since it was discovered in 1986 [1]. As one of the most important high-Tc oxide superconductors, $\text{YBa}_2\text{Cu}_3\text{O}_{7-x}$ (YBCO) owns a well-defined cation stoichiometry and is easy to synthesize [2]. Research related to YBCO physical and chemical properties has been reported in a great number of publications [3–5].

Along with industrial advance, environmental issues such as the remediation of hazardous waste, contaminated ground-waters, and control of toxic air contaminant have arisen [6]. Photocatalysis by polycrystalline semiconductor oxides is a way to degrade organic and inorganic pollutants [7]. Many semiconductor materials have been investigated and used because of their photodegradation properties [8]. One of the most famous photocatalysts is TiO_2 , which has showed excellent photocatalytic effect as reported [9–15]. Meanwhile, doped TiO_2 and many other complex oxides were also investigated for their photocatalytic properties [16–19]. As mentioned in the literature, the superconductivity of YBCO can be derived from its unique structure [20–22].

The distortion of Cu-O crystal plane caused by a certain amount of oxygen deficiency plays a significant role in superconductivity [23]. However, in some structure modified cases, the normal crystal structure related to superconductivity may be changed, resulting in nonsuperconductivity of YBCO materials (which may eventually transform to the semiconductor) [24, 25]. It is known that the fixed band gap in a semiconductor is the origin of its photocatalysis. Besides, nanosize single crystal may also exhibit different characteristics with traditional materials because of its special structure and size [4, 26–32]. In this case, YBCO may have photocatalytic activities. Although the electrical properties of YBCO have been investigated thoroughly and extensively, few studies if any on photocatalytic activities of YBCO materials have been reported up until now.

As a conventional synthesis technique, soft chemical method has potential to be applied for large-scale preparation on account of many factors: simple instruments, controllable procedures, cheap original chemicals, and high dimension uniformity [33–35]. In this work, YBCO nanoparticles (NPs) were synthesized through soft chemical method. In addition to conventional structure measurements, the photocatalytic

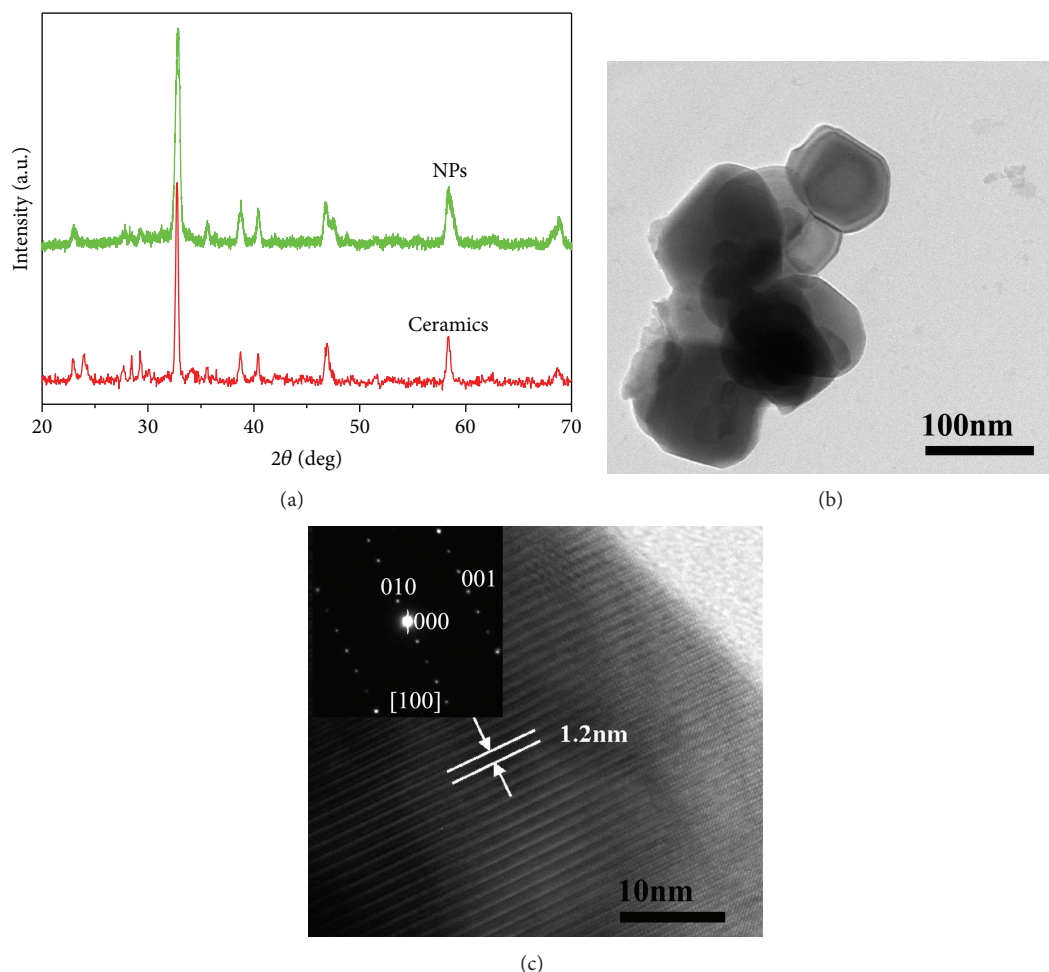


FIGURE 1: (a) XRD patterns of YBCO NPs (NPs, green line) and corresponding ceramics (red line) sintering at 900°C for 2 h. (b) TEM image of YBCO NPs. (c) HRTEM image of YBCO NPs, inset: the SAED pattern.

properties of YBCO NPs and YBCO ceramics were systematically investigated. The superconductivity of the YBCO ceramics was also studied for comparison.

2. Experimental Methods

$\text{YBa}_2\text{Cu}_3\text{O}_{7-x}$ NPs were synthesized from precursors $\text{Y}(\text{CH}_3\text{COO})_3 \cdot 4\text{H}_2\text{O}$, $\text{Ba}(\text{CH}_3\text{COO})_2$ and $\text{Cu}(\text{CH}_3\text{COO})_2 \cdot \text{H}_2\text{O}$ with stoichiometric ratio of 1:2:3. The pH value of the stable solution was adjusted to 1~2 by adding certain amount of aqueous ammonia ($\text{NH}_3 \cdot \text{H}_2\text{O}$) and nitric acid (HNO_3). After annealing in flowing oxygen environment at 900°C for 2 hours, black YBCO NPs powders were obtained. Furthermore, YBCO ceramics were prepared through conventional process using YBCO NPs as precursors. The pellet was sintered in flowing oxygen environment at 900°C for 2 hours. In the photocatalytic measurement, YBCO NPs were dispersed in methylene blue (MB) with certain concentration, and the ceramics were grinded into powders as contrast.

Phase structures of the final samples were studied on a Philips X-ray diffraction (XRD) system using $\text{CuK}\alpha$

($\lambda = 1.5406 \text{ \AA}$) as the radiation source. Transmission electron microscopy (TEM) images and high-resolution transmission electron microscopy (HRTEM) images were obtained through a JEOL 2011 transmission electron microscope at an acceleration voltage of 200 kV. The superconducting transition temperatures were measured by Closed Cycle Refrigerator System. The UV absorption spectra were measured using a Shimadzu UV-2550 (Kyoto, Japan) spectrophotometer. Photocatalytic activities of the NPs for degradation of MB were evaluated by agitating the solution and irradiating the samples using a 250 W high-pressure Hg lamp. The initial concentration of MB was $1.8 \times 10^{-5} \text{ mg/L}$ with a catalyst loading of $1.5 \times 10^{-3} \text{ mol/L}$ in the experiment.

3. Results and Discussion

XRD patterns of as-synthesized YBCO NPs and ceramics are shown in Figure 1(a). It can be seen that the diffraction peaks correspond to pure-phase YBCO, which has a perovskite structure with an orthorhombic symmetry. In our case, pure-phase and higher crystallized YBCO NPs could be formed by using chelate compound as precursor, which can function

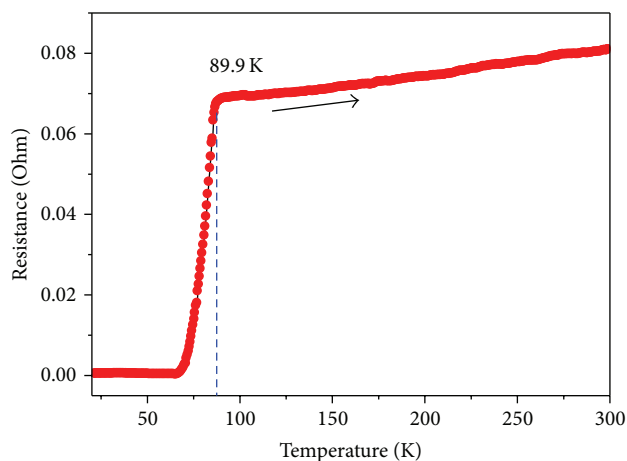


FIGURE 2: Resistance-temperature curve of YBCO ceramics sample.

stably in a strong acid environment with pH value 1~2. Further structure characterizations of YBCO NPs were made using TEM as shown in Figures 1(b) and 1(c). One can see that the YBCO NPs have an average diameter of about 100 nm. Figure 1(c) shows the HRTEM image and SAED pattern of the sample. As presented, the NPs are highly crystallized with a lattice spacing of about 1.2 nm, corresponding to interlayer spacing of the (010) planes in the YBCO crystal lattice.

To prove the superconductivity of YBCO ceramics synthesized from YBCO NPs, the conducting properties of the samples were determined. The resistance versus temperature curve in Figure 2 clearly shows that the YBCO ceramics exhibited behaviour of a typical high- T_c superconductor. It has transition temperature width from onset temperature 89.9 K to zero-resistance temperature 64.9 K.

The photocatalytic activities of YBCO NPs and ceramics powders were evaluated by the decomposition of methylene blue (MB) under the irradiation of a medium-pressure Hg lamp. A group of MB solution with no catalysts was also treated as contrast. In the literature, MB is usually used as standard dyes in photocatalytic activity testing for its photostability. Figure 3 shows the photodegradation of MB solution as a function of reaction time for different catalysts. In the photocatalysis measurement, we took groups of photodegraded solution several times and then used the spectrophotometer to measure the UV adsorption spectra. C_0 and C_t represent the intensity of the maximum absorption peaks of the UV adsorption spectra of solution initially and at time t . Take nature logarithm function of ratio C_0/C_t to obtain the ordinate in Figure 3. It can be seen that MB solution without catalyst is stable under irradiation. This phenomenon was also found when the YBCO ceramic powders were used as photocatalyst. However, in the presence of YBCO NPs, the MB concentration dropped to almost zero after 7 hours of irradiation. Such remarkable contrast could also be observed in the insets ((a) and (b)) in Figure 3. The colour of MB solution using YBCO ceramics powders as photocatalyst shows no changes during the 7-hour irradiation. On the other hand, almost all dyes in the MB solution which carried YBCO NPs were degraded after 7 hours. Therefore it can

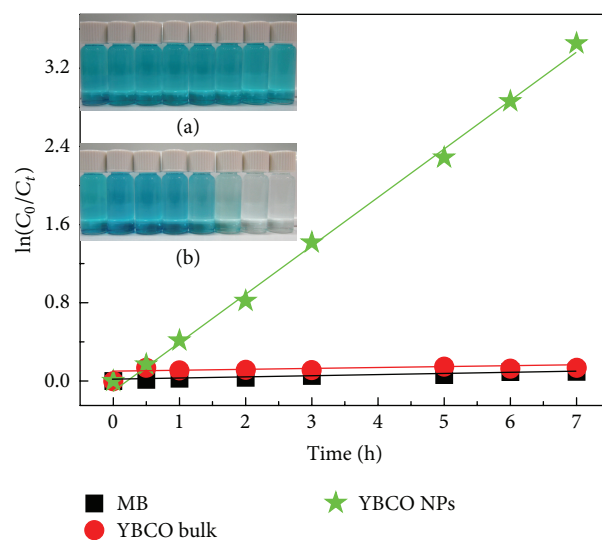


FIGURE 3: Photodegradation of MB solution with different photocatalysts: no catalysts (black line), YBCO ceramics (red line), and YBCO NPs (green line). Inset (a) MB solution using YBCO ceramics powders as photocatalyst after different hours of irradiation. Inset (b) MB solution using YBCO NPs as photocatalyst after different hours of irradiation.

be concluded that YBCO NPs and corresponding ceramics behaved significantly different in photocatalysis.

Previous studies suggested that an appropriate band-gap in semiconductor catalysts is the origin of its photocatalytic activities. In photocatalysis, when the energy irradiation is higher or equal to the band-gap of the semiconductor catalyst, excited state valence-band holes and conduction-band electrons would form [6–8]. Then the holes and electrons could be got trapped in metastable surface states to recombine or react with electron acceptors and electron donors adsorbed on the semiconductor surface or within the surrounding electrical double layer of the charged particles. If a suitable scavenger or surface defect state is available to trap the electrons or holes, the recombination could be prevented. Subsequently, the holes and electrons generated by exciting photons could have redox reaction with dyes in the solutions. It means that suitable band-gap energy is a key reason in photocatalysis. Therefore, photocatalysis cannot take place in conductors and/or superconductors. From the resistance versus temperature curve (Figure 2), it is evident that YBCO ceramics fabricated from NPs show superconductivity. So YBCO ceramics could not lead to photodegradation of MB.

However, for the YBCO NPs, they show significant photodegradation. As discussed above, surface defects were also another important reason in photocatalysis for the excited state valence-band holes and conduction-band electrons were trapped in metastable surface states in the reaction. Generally speaking, it is easy to attribute this abnormal photocatalysis to very small particle size (and/or large number of defects). But their TEM images in Figure 1(b) reveal the nanoparticle size is about 100 nm, which is relatively large and the surface atoms are not enough to dominate this novel property. So the main

reason for this phenomenon must come from modified band-gap energy in YBCO NPs.

As a famous high temperature superconductor, YBCO also has different conductivities depending on its oxygen content. Researches showed that $\text{YBa}_2\text{Cu}_3\text{O}_{7-x}$ had a semiconductor-like resistance characteristic when its oxygen content is in the range $0.5 < x < 0.7$ [36, 37]. Besides, for YBCO NPs in this work, it has single crystal phase as shown in Figure 1(c). Under the action of many mechanisms, YBCO single crystal can also perform novel properties [28–31], such as the formation of oxygen vacancies clusters [32]. Moreover, as compared to our former researches on the high temperature superconductor YBCO [5], the annealing period for YBCO NPs is relatively shorter in this work. So the oxygen content of YBCO NPs could be dominated by both the single crystal and the shorter annealing period. As a result, these might have led the YBCO NPs to be nonsuperconductive and have proper band-gap energy, which consequently make it possible to exhibit the vigorous photocatalytic activities. As a matter of fact, there are reports in the literature that, in some structure modified cases, the superconductivity of YBCO materials has vanished, which is likely to be consistent with our samples [20, 23]. This could be an effective method to investigate the potential properties and application in YBCO based composites. More characterization (such as PL spectra) and detailed study on the novel properties of YBCO NPs are highly desired [38].

4. Conclusions

YBCO NPs with narrow size distribution were obtained through a soft chemical route. The results showed that YBCO nanoparticles could produce excellent photocatalytic effects, while no degradation reactivities were observed for YBCO ceramics with normal superconductivity. The semiconductive nature induced by structure modification may be accounted for the photocatalytic effect of YBCO nanoparticles.

Conflict of Interests

The authors declare that they have no conflict of interests regarding the publication of this paper.

Authors' Contribution

Zhenjiang Shen and Yongming Hu contributed equally to this work.

Acknowledgments

This work was financially supported by the Hong Kong Polytechnic University (Projects A-PK29 and A-PL53) and the "863" High-Tech Project of China (Project no. 2013AA031903). Support from National Natural Science Foundation of China (no. 11304069), Natural Science Foundation of Hainan Province (no. 114009), and the Chutian Chair Professorship of Hubei Province is also acknowledged.

References

- [1] G. Blatter, M. V. Feigelman, V. B. Geshkenbein, A. I. Larkin, and V. M. Vinokur, "Vortices in high-temperature superconductors," *Reviews of Modern Physics*, vol. 66, no. 4, pp. 1125–1388, 1994.
- [2] R. X. Liang, P. Dosanjh, D. A. Bonn, D. J. Baar, J. F. Carolan, and W. N. Hardy, "Growth and properties of superconducting YBCO single crystals," *Physica C*, vol. 195, no. 1-2, pp. 51–58, 1992.
- [3] M. A. Beno, L. Soderholm, D. W. Capone et al., "Structure of the single-phase high-temperature superconductor $\text{YBa}_2\text{Cu}_3\text{O}_{7-\delta}$," *Applied Physics Letters*, vol. 51, no. 1, pp. 57–59, 1987.
- [4] D. A. Wollman, D. J. van Harlingen, W. C. Lee, D. M. Ginsberg, and A. J. Leggett, "Experimental determination of the superconducting pairing state in YBCO from the phase coherence of YBCO-Pb dc SQUIDS," *Physical Review Letters*, vol. 71, no. 13, pp. 2134–2137, 1993.
- [5] Z. J. Shen, Y. Wang, W. P. Chen et al., "Electrospinning preparation and high-temperature superconductivity of $\text{YBa}_2\text{Cu}_3\text{O}_{7-x}$ nanotubes," *Journal of Materials Science*, vol. 48, no. 11, pp. 3985–3990, 2013.
- [6] M. R. Hoffmann, S. T. Martin, W. Choi, and D. W. Bahnemann, "Environmental applications of semiconductor photocatalysis," *Chemical Reviews*, vol. 95, no. 1, pp. 69–96, 1995.
- [7] G. Palmisano, V. Augugliaro, M. Pagliaro, and L. Palmisano, "Photocatalysis: a promising route for 21st century organic chemistry," *Chemical Communications*, no. 33, pp. 3425–3437, 2007.
- [8] A. Mills and S. Le Hunte, "An overview of semiconductor photocatalysis," *Journal of Photochemistry and Photobiology A: Chemistry*, vol. 108, no. 1, pp. 1–35, 1997.
- [9] S. Livraghi, A. Votta, M. C. Paganini, and E. Giamello, "The nature of paramagnetic species in nitrogen doped TiO_2 active in visible light photocatalysis," *Chemical Communications*, vol. 28, no. 4, pp. 498–500, 2005.
- [10] S. M. Fonseca, A. L. Barker, S. Ahmed, T. J. Kemp, and P. R. Unwin, "Direct observation of oxygen depletion and product formation during photocatalysis at a TiO_2 surface using scanning electrochemical microscopy," *Chemical Communications*, vol. 9, no. 8, pp. 1002–1003, 2003.
- [11] T. L. Thompson and J. T. Yates Jr., " TiO_2 -based photocatalysis: surface defects, oxygen and charge transfer," *Topics in Catalysis*, vol. 35, no. 3-4, pp. 197–210, 2005.
- [12] A. L. Linsebigler, G. Lu, and J. T. Yates Jr., "Photocatalysis on TiO_2 surfaces: principles, mechanisms, and selected results," *Chemical Reviews*, vol. 95, no. 3, pp. 735–758, 1995.
- [13] J. Zhang, L. S. Qian, W. Fu, J. H. Xi, and Z. G. Ji, "Alkaline-earth metal Ca and N codoped TiO_2 with exposed {001} facets for enhancing visible light photocatalytic activity," *Journal of the American Ceramic Society*, vol. 97, no. 8, pp. 2615–2622, 2014.
- [14] J. Zhang, W. K. Chen, J. H. Xi, and Z. G. Ji, "{001} Facets of anatase TiO_2 show high photocatalytic selectivity," *Materials Letters*, vol. 79, pp. 259–262, 2012.
- [15] J. Zhang, W. Fu, J. H. Xi et al., "N-doped rutile TiO_2 nano-rods show tunable photocatalytic selectivity," *Journal of Alloys and Compounds*, vol. 575, pp. 40–47, 2013.
- [16] R. Asahi, T. Morikawa, T. Ohwaki, K. Aoki, and Y. Taga, "Visible-light photocatalysis in nitrogen-doped titanium oxides," *Science*, vol. 293, no. 5528, pp. 269–271, 2001.
- [17] Y.-M. Hu, H.-S. Gu, D. Zhou, Z. Wang, H. L.-W. Chan, and Y. Wang, "Orientation-control synthesis of $\text{KTa}_{0.25}\text{Nb}_{0.75}\text{O}_3$

- nanorods,” *Journal of the American Ceramic Society*, vol. 93, no. 3, pp. 609–613, 2010.
- [18] O. Carp, C. L. Huisman, and A. Reller, “Photoinduced reactivity of titanium dioxide,” *Progress in Solid State Chemistry*, vol. 32, no. 1-2, pp. 33–177, 2004.
- [19] S. Ould-Chikh, O. Proux, P. Afanasiev et al., “Photocatalysis with chromium-doped TiO_2 : bulk and surface doping,” *ChemSusChem*, vol. 7, no. 5, pp. 1361–1371, 2014.
- [20] R. J. Cava, A. W. Hewat, E. A. Hewat et al., “Structural anomalies, oxygen ordering and superconductivity in oxygen deficient $\text{Ba}_2\text{YCu}_3\text{O}_x$,” *Physica C: Superconductivity and its applications*, vol. 165, no. 5-6, pp. 419–433, 1990.
- [21] P. X. Zhang and H.-U. Habermeier, “Atomic layer thermopile materials: physics and application,” *Journal of Nanomaterials*, vol. 2008, Article ID 329601, 12 pages, 2008.
- [22] H. I. Wang, W. T. Tang, L. W. Liao et al., “Femtosecond laser-induced formation of wurtzite phase ZnSe nanoparticles in air,” *Journal of Nanomaterials*, vol. 2012, Article ID 278364, 6 pages, 2012.
- [23] J. D. Jorgensen, B. W. Veal, A. P. Paulikas et al., “Structural properties of oxygen-deficient $\text{YBa}_2\text{Cu}_3\text{O}_{7-\delta}$,” *Physical Review B*, vol. 41, no. 4, pp. 1863–1877, 1990.
- [24] S. Linzen, J. Kräußlich, A. Köhler, P. Seidel, B. Freitag, and W. Mader, “Unusual crystal structure of non-superconducting $\text{Y}_1\text{Ba}_2\text{Cu}_3\text{O}_{7-x}$ films on buffered silicon substrates,” *Physica C: Superconductivity and Its Applications*, vol. 290, no. 3-4, pp. 323–333, 1997.
- [25] M. Longhin, A. J. Kreisler, and A. F. Dégardin, “Semiconducting YBCO thin films for uncooled terahertz imagers,” *Materials Science Forum*, vol. 587-588, pp. 273–277, 2008.
- [26] C. Lin, X. Zhu, J. Feng et al., “Hydrogen-incorporated TiS_2 ultrathin nanosheets with ultrahigh conductivity for stamp-transferable electrodes,” *Journal of the American Chemical Society*, vol. 135, no. 13, pp. 5144–5151, 2013.
- [27] Y. Q. Guo, K. Xu, C. Z. Wu, J. Y. Zhao, and Y. Xie, “Surface chemical-modification for engineering the intrinsic physical properties of inorganic two-dimensional nanomaterials,” *Chemical Society Reviews*, vol. 44, no. 3, pp. 637–646, 2015.
- [28] K. Xu, X. L. Li, P. Z. Chen et al., “Hydrogen dangling bonds induce ferromagnetism in two-dimensional metal-free graphitic- C_3N_4 nanosheets,” *Chemical Science*, vol. 6, no. 1, pp. 283–287, 2015.
- [29] R. Liang, D. A. Bonn, and W. N. Hardy, “Discontinuity of reversible magnetization in untwinned YBCO single crystals at the first order vortex melting transition,” *Physical Review Letters*, vol. 76, no. 5, pp. 835–838, 1996.
- [30] J. Y. T. Wei, N.-C. Yeh, D. F. Garrigus, and M. Strasik, “Directional tunneling and andreev reflection on $\text{YBa}_2\text{Cu}_3\text{O}_{7-\delta}$ single crystals: predominance of d-wave pairing symmetry verified with the generalized blonder, tinkham, and klapwijk theory,” *Physical Review Letters*, vol. 81, no. 12, pp. 2542–2545, 1998.
- [31] F. M. Sauerzopf, “Anisotropic flux pinning in $\text{YBa}_2\text{Cu}_3\text{O}_{7-\delta}$ single crystals: the influence of defect size and density as determined from neutron irradiation,” *Physical Review B—Condensed Matter and Materials Physics*, vol. 57, no. 17, pp. 10959–10971, 1998.
- [32] D. A. Lotnyk, A. V. Bondarenko, A. A. Zavgorodniy, M. A. Obolenskiy, and A. Feher, “Anisotropy of static and dynamic order-disorder transition in $\text{YBa}_2\text{Cu}_3\text{O}_{7-\delta}$ single crystal,” *Journal of Physics: Conference Series*, vol. 150, no. 5, Article ID 052142, 2009.
- [33] Z. Chen, Q. Gao, C. Wu, M. Ruan, and J. Shi, “Preparation and properties of an ordered, uniform 0.9 nm Ag array assembled in a nanoporous VSB-1 by a simple soft chemical method,” *Chemical Communications*, vol. 10, no. 17, pp. 1998–1999, 2004.
- [34] N. R. Jana, L. Gearheart, and C. J. Murphy, “Wet chemical synthesis of silver nanorods and nanowires of controllable aspect ratio,” *Chemical Communications*, no. 7, pp. 617–618, 2001.
- [35] W. Z. Wang and L. Ao, “A soft chemical synthesis of TiO_2 nanobelts,” *Materials Letters*, vol. 64, no. 8, pp. 912–914, 2010.
- [36] M. Longhin, A. J. Kreisler, and A. F. Dégardin, “Semiconducting YBCO thin films for uncooled terahertz imagers,” *Materials Science Forum*, vol. 587-588, pp. 273–277, 2008.
- [37] V. S. Jagtap, A. Scheuring, M. Longhin, A. J. Kreisler, and A. F. Dégardin, “From superconducting to semiconducting YBCO thin film bolometers: sensitivity and crosstalk investigations for future thz imagers,” *IEEE Transactions on Applied Superconductivity*, vol. 19, no. 3, pp. 287–292, 2009.
- [38] X. Peng, L. Manna, W. Yang et al., “Shape control of CdSe nanocrystals,” *Nature*, vol. 404, no. 6773, pp. 59–61, 2000.